STUDY OF PHYSICAL PROPERTIES OF LEAD-FREE METAL HALIDE PEROVSKITE COMPOUNDS $CsMI_3$ (M= Mg, Ga) FOR SOLAR CELLS APPLICATIONS BY AB-INITIO SIMULATIONS

By

Mautushi Biswas

MSc in Physics

Student ID: 20MSPHY003

A thesis submitted in partial fulfilment of the requirements for the degree of MASTER of SCIENCE in Physics

Department of Physics

CHITTAGONG UNIVERSITY OF ENGINEERING AND TECHNOLOGY

June, 2024

CERTIFICATION

The thesis titled "STUDY OF PHYSICAL PROPERTIES OF LEAD-FREE METAL HALIDE PEROVSKITE COMPOUNDS CsMI3 (M= Mg, Ga) FOR SOLAR CELLS APPLICATIONS BY AB-INITIO SIMULATIONS" submitted by **Mautushi Biswas,** Roll No. 20MSPHY003F, Session: 2020-2021 has been accepted as satisfactory in partial fulfilment of the requirement for the degree of Master of Science (Physics) on the 3rd June, 2024.

BOARD OF EXAMINERS

1. _____ Chairman
Dr. Md. Mohi Uddin Supervisor
Professor
Department of Physics
Chittagong University of Engineering & Technology
Chattogram-4349

2. _____ Member (Ex-Officio)
Head
Professor
Department of Physics
Chittagong University of Engineering & Technology
Chattogram-4349

3. _____ Member
Dr. Md. Ashraf Ali
Professor
Department of Physics
Chittagong University of Engineering & Technology
Chattogram-4349

4. _____ Member
Dr. Nusrat Jahan
Professor
Department of Physics
Chittagong University of Engineering & Technology
Chattogram-4349

5. _____ Member (External)
Dr. Md. Nuruzzaman
Professor
Rajshahi University of Engineering & Technology
Department of Physics
Rajshahi-6204

Declaration

I hereby declare that the work contained in this thesis has not been previously submitted to meet the requirements for an award at this or any other higher education institution. To the best of my knowledge and belief, the Thesis contains no material previously published or written by another person except where due reference is cited. Furthermore, the Thesis complies with the PLAGIARISM and ACADEMIC INTEGRITY regulations of CUET.

Mautushi Biswas
20MSPHY003F
Department of Physics
Chittagong University of Engineering & Technology (CUET)

Dedication

I dedicate this thesis to my family members, friends, well-wishers, and every individual who has contributed to my learning journey.

List of Publications

Journal Article

M. Biswas, S. Ghosh, J. Chowdhury, M.A. Ali, M.M. Hossain, S.H. Naqib, M.M. Uddin, "An inclusive study of lead-free perovskite CsMI3 materials for photovoltaic and optoelectronic appliance explored by a first principles study'' **Materials Today Communications** xxx (2024) 109422 (Elsevier, IF-3.8).
https://doi.org/10.1016/j.mtcomm.2024.109422

Conference

"An inclusive study of lead-free perovskite $CsMI_3$ materials for photovoltaic and optoelectronic appliance explored by a first principle study'': M. Biswas, M. A. Ali, M. M. Hossain, S. H. Naqib, S Ghosh, J. Chowdhury And M. M. Uddin. 5^{th} International conference on "Physics for Sustainable Development & Technology (ICPSDT-2023)" held on 7-8 September 2023; organized by Department of Physics, CUET.

Approval/Declaration by the Supervisor(s)

This is to certify that Mautushi Biswas bearing roll number 20MSPHY003F has carried out this research work under my/our supervision and that she has fulfilled the relevant Academic Ordinance of the Chittagong University of Engineering & Technology so that she is qualified to submit the following Thesis in the application for the degree of MASTER OF SCIENCE in PHYSICS. Furthermore, the Thesis complies with the PLAGIARISM and ACADEMIC INTEGRITY regulations of CUET.

Dr. Md Mohi Uddin
Professor
Department of Physics
Chittagong University of Engineering & Technology

Acknowledgement

I express my gratitude to Almighty God and extend my heartfelt thanks to my family members for their support in the successful completion of my dissertation work.

This work has been done under the supervision of Dr. Md. Mohi. Uddin, Professor, Department of Physics, Chittagong University of Engineering & Technology (CUET). My heartfelt thanks to Dr. Uddin for his excellent guidance. His intellectual mentoring, critical reviews, and constructive comments contributed significantly to the formulation of my thesis. His helpful direction and unwavering support throughout the procedure were truly encouraging, allowing me to submit this dissertation with confidence.

I thank Prof. Dr. H.M.A.R. Maruf, Head of Physics Department at Chittagong University of Engineering & Technology (CUET), for their valuable support and materials during the writing of my dissertation. I am also grateful to Prof. Swapan Kumar Roy, ex-head of the Department of Physics at CUET, who was cordial throughout the research journey. I would like to express my gratitude to Associate Prof. Dr. Md. Mukter Hossain and Prof. Dr. Ashraf Ali for their guidance. For their constant encouragement and support, I am grateful to Prof. Dr. Mohammad Belal Hossen, Prof. Dr. Swapan Kumar Roy, Prof. Dr. Animesh Kumar Chakraborty, Prof. Dr. Nusrat Jahan, Mr. Shaiful Kabir, Mr. Zahid Hasan, Sinthia Binte Kholil, and Mr. Md. Abdur Rahman.

UNESCO-TWAS and the Swedish International Development Cooperation Agency (SIDA) supported this work with a grant (grant number: 21-378 RG/PHYS/AS_G-FR3240319526). The views expressed herein do not necessarily represent those of UNESCO-TWAS, SIDA, or its Board of Governors.

May, 2024

The Author

(Mautushi Biswas)

Abstract

The primary objectives are to thoroughly examine the $CsMI_3$ (M = Mg, Ga) lead-free perovskite materials for photovoltaic and optoelectronic applications using first-principle calculations. This study observed the mechanical, electrionic, optical, thermal, and structural aspects while also verifying the stability of the cell. The calculated results are compared with experimentally synthesized similar perovskite compound $CsPbI_3$. The computed formation energies of the compounds as follows: $CsMgI_3$(-1.81 eV/atom) > $CsPbI_3$(-1.624 eV/atom) > $CsGaI_3$(-1.326 eV/atom) and negative results are represented the mechanically stability of the compounds. Since there was no negative frequency, the phonon research demonstrated the compound's dynamic stability. The computed ν values support the $CsMI_3$ (M= Pb, Ga) compounds possess pure ductility, whereas the $CsMgI_3$ compounds lie on the ductile-brittle transition line. The bandgap (E_g) is calculated and found to be in the range of 1.63 to 3.26 eV that makes them potential candidate to be used as absorbance materials in solar cell applications. The E_g is further tuned to achieve more appropriate range for the solar cell applications by doping into the $CsMg(I_{1-x}Br_x)_3$ where x = (0, 0.25, 0.50, 0.75, 1). The E_g is found to be 1.12 to 1.87 eV and α increase due to doping that makes them more apposite for the suggested range of absorbance materials in the solar cell. The best combination $CsMg(I_{0.75}Br_{0.25})_3$ shows E_g ~ 1.4 eV that is well agreement with the optimum band gap suggested the Shockley-Queisser limit in a single layer solar cell absorbance material to be shown highest efficiency.

বিমূর্ত

প্রাথমিক উদ্দেশ্য হল $CsMI_3$ (M = Mg, Ga) সীসা-মুক্ত পেরোভস্কাইট উপাদানগুলিকে প্রথম-নীতিগত গণনা ব্যবহার করে ফটোভোলটাইক এবং অপটোইলেক্ট্রনিক অ্যাপ্লিকেশনগুলির জন্য পুঙ্খানুপুঙ্খভাবে পরীক্ষা করা। এই গবেষণায় mechanical, electronic, optical, thermal, and structural এবং structural stability যাচাই করা হয়েছে। গণনা করা ফলাফলগুলি পরীক্ষামূলকভাবে সংশ্লেষিত অনুরূপ পেরোভস্কাইট যৌগ $CsPbI_3$ এর সাথে তুলনা করা হয়। নিম্নরূপ যৌগগুলির গণনাকৃত formation energy: $CsMgI_3$(-1.81 eV/atom) > $CsPbI_3$(-1.624 eV/atom) > $CsGaI_3$(-1.326 eV/atom) এবং negative ফলাফলগুলি যান্ত্রিকভাবে যৌগিক স্থিতিশীলতার প্রতিনিধিত্ব করে। যেহেতু কোন negative ফ্রিকোয়েন্সি ছিল না, ফোনন গবেষণা যৌগের dynamical stability প্রদর্শন করেছে। গণনা করা ν মানগুলি $CsMI_3$ (M= Pb, Ga) যৌগগুলিকে সমর্থন করে যা pure ductility ধারণ করে, যেখানে $CsMgI_3$ যৌগগুলি নমনীয়-ভঙ্গুর রূপান্তর লাইনের উপর থাকে। ব্যান্ডগ্যাপ (E_g) গণনা করা হয় এবং 1.63 থেকে 3.26 eV-এর মধ্যে পাওয়া যায় যা তাদের সৌর কোষ অ্যাপ্লিকেশনগুলিতে absorbance material হিসাবে ব্যবহার করার সম্ভাব্য প্রার্থী করে তোলে। $CsMg(I_{1-x}Br_x)_3$ যেখানে x = (0, 0.25, 0.50, 0.75, 1) ডোপিং করে সৌর কোষ অ্যাপ্লিকেশনের জন্য আরও উপযুক্ত পরিসর অর্জনের জন্য উদাহরণটিকে আরও টিউন করা হয়েছে। উদাহরণটি 1.12 থেকে 1.87 eV এবং α ডোপিংয়ের কারণে বৃদ্ধি পাওয়া যায় যা সৌর কোষে শোষণকারী পদার্থের প্রস্তাবিত পরিসরের জন্য তাদের আরও উপযুক্ত করে তোলে। সেরা সংমিশ্রণ $CsMg(I_{0.75}Br_{0.25})_3$ দেখায় যেমন $E_g \sim 1.4$ eV যা সর্বোত্তম ব্যান্ড গ্যাপের সাথে ভালভাবে একমত যা সর্বোচ্চ দক্ষতা দেখানোর জন্য একটি একক স্তরের সৌর কোষ absorbance material Shockley-Queisser limit পরামর্শ দেয়।

Table of Contents

List of Figures

List of Tables

NOMENCLATURE

AE	All-Electron
AO	Atomic Orbital
BF	Block Function
BO	Born –Oppenheimer
BZ	Brillouin Zone
BFGS	Broyden-Fletcher-Goldfrab-Shanno
BOP	Bond of Population
CO	Crystal Orbital
CASTEP	Cambridge Serial Total Energy Package
DF	Density Functional
DFPT	Density Functional perturbation Theory
DFT	Density Functional Theory
DOS	Density of States
ECP	Effective Core Potential
eV	Electron Volts
EVC	Effective Valence Charge
GGA	Generalized Gradient Approximation
GPa	Giga Pascals
GS	Ground State
GSES	Ground States Electronic Structure
HF	Hartree-Fock
IR	Infrared
KS	Kohn and Shan
LCAO	Linear Combination of Atomic Orbital
LDA	Local Density Approximation
LO	Longitudinal Optical
LDOS	Local Electron Density of State
MAP	Mulliken Atomic Population
PBE	Perdew, Burke, and Ernzerhof
PDOS	Projected Density of States/ Partial Density of States
PP	Pseudopotential
PWPP	Plane Wave Pseudopotential
PDC	Phonon Dispersion Curve
RPBE	Revised Perdew-Burke-Ernzerhof
SAW	Surface Acoustic Wave
SCF	Self-Consistent Field
TO	Transverse Optical
UV	Ultraviolet
VEC	Valence Electron Concentration
VRH	Voigt-Reuss-Hill
XC	Exchange Correlation
XRD	X-Ray Diffraction

Chapter 1: INTRODUCTION

Because of the rapid changes in the global economic and social landscape, the more energy is required than traditional fossil fuels can provide. Solar energy will undoubtedly offer a variety of benefits, like being renewable and pollution-free, given that it is destined to be the primary energy source in the 4IR. In nature, metal halide perovskites (MHP) are commonly accessible and reasonably priced. Consequently, solar cells based on these materials would be more economical and efficient than silicon-based photovoltaic (PV) technology [1,2]. Due to their remarkable opto-electronic properties which include a tunable bandgap, high optical absorption, broad absorption spectrum, small carrier effective mass, long charge diffusion length, and high charge carrier mobility [1,3–12], the MHPs have recently attracted a great deal of attention from the scientific community. In recent times, there has been a significant increase in the power conversion efficiency (PCE) of lead (Pb)-based metal halide perovskite solar cells (MHPSCs) from 3.8% to 25.5% [13–15]. Additionally, a significant number of MHPSCs have successfully passed a test of the 1,000-hour operational stability benchmark [16,17]. Lead halide perovskites have been used to create devices with the power conversion efficiency of about 22% [18], which is comparable to materials used in conventional solar cells such as cadmium telluride (CdTe), copper indium gallium selenide (CIGS), and single-crystal Si [13]. $CH_3NH_3PbI_3$, a typical hybrid organic-inorganic halide perovskite, features a bandgap that is close to the Shockley–Queisser optimum, [19,20] significant visible spectrum absorption, [21,22] long carrier lives, [23,24] high charge carrier mobilities, [25–27] and long carrier lifetimes. As a result, in a solar cell, $CH_3NH_3PbI_3$ can function as a charge-transporting layer that is both effective and light-absorbing. On the other hand, poisoning of lead is a significant environmental hazard. Because lead perovskites tend to break down in ambient circumstances and release toxic chemicals like PbI_2, using lead is especially hazardous [28]. These Pb-based high-efficiency PSCs [$MAPbI_3$, $FAPbI_3$, $Cs_{0.05}$ $FA_{0.85}$ $MA_{0.10}$ Pb ($I_{0.97}$ $Br_{0.03}$)$_3$] do, however, have certain inevitable drawbacks, namely, that lead is a poisonous element that is difficult for organisms and the environment to remove from the body. According to research, lead ion poisoning of soil and water sources is persistent and has a highly severe effect on plant, animal, and human survival [29–31]. Because lead may enter the body, attach to an enzyme, and then build up through blood circulation in soft tissues and bones such as the brain, liver, kidney, and spleen. The afflicted person's neurological,

digestive, and circulatory systems gradually develop functional problems as a result of lead poisoning. Most people usually start showing symptoms of lead poisoning when their daily lead consumption hits 0.5 mg [30,31]. Thus, various non- or low-toxic metal ions must be selected to substitute lead as PSC perovskite absorbers in order to guarantee that the natural environment for people is safe and pollution-free [32–35].

ABX_3, where X is a halogen anion, B is a metal cation, and A is an organic cation, is the general chemical formula for metal halide perovskites [36–39]. Here, the halogen anion is often made up of Cl, Br, I, or their mixture, while the organic cation is typically composed of methylammonium (MA), formamidinium (FA), Cs, or their mixture. Regarding B, prior research has demonstrated that less hazardous ions such as Sn^{2+}, Bi^{3+}, Ge^{2+}, Sb^{3+}, Mn^{2}+, and Cu^{2+} may be substituted for Pb^{2+} in perovskites to create a novel lead-free structure [12,40,41]. The addition of these metal cations improves PSCs' ecologically beneficial qualities while also broadening the variety of perovskite species. It is crucial to look for novel B metals and their solid solutions as well as opto-electronic properties in order to create highly efficient solar cells based on Pb-free MHPSCs. Furthermore, MHP solar cells would be more economical and efficient than photovoltaic (PV) technology based on silicon. Due to these remarkable properties, this family of semiconductors may be used in light-emitting diodes, photodetectors, and solar-to-fuel energy conversion devices, among other electronic devices, in addition to solar cells [1,4,11,12]. In order to forecast a particular device application and advancements, a more profound and basic comprehension of the semiconductor features is required. Furthermore, an examination of a material's optical functions can reveal information about how it responds to light. Therefore, for a material to be employed in real-world optoelectronic devices like solar cells, diodes, lasers, etc., a detailed understanding of the optical characteristics is required. When choosing a certain perovskite material to utilize as the absorbance/active layer in the solar cell construction, metrics such as the energy (wavelength) dependent absorption coefficient, shallow acceptor density (N_A), shallow donor density (N_D), etc., are crucial to know. To determine the efficiency, these factors must be entered into a simulation of the solar cell structure. However, only a few investigations have been done on the perovskite compounds' optical characteristics. The regular and frequent modelling of perovskite-based solar cells, which is crucial to the advancement of the cell like the well-known CdTe or CIGS based solar cell structure, was hampered by the lack of perovskite material properties. Based on the low

electron effective mass, which is caused by exceptionally dispersive conduction bands, and band gap tuning between 0.9 and 1.7 eV (1.7 eV for $CsMgI_3$, 1.5 eV for $CH_3NH_3MgI_3$, and 0.9 eV for $CH(NH_2)_2MgI_3$), ten compounds out of 248 candidates have been identified for potential solar cell applications with high-throughput screening [42]. In order to make these compounds suitable for optoelectronic and photovoltaic applications, certain proposed lead-free perovskites (M = Mg, Ga, Ca, Ba and Sr) with Mg, Ca, Ba, and Sr being alkaline-earth metals were tuned here to predict their optoelectronic characteristics [42,43].

In this context, Pb-free inorganic MHP compounds have been examined using first-principles density functional theory (DFT) to comprehend their overall properties. The main objective of this study is to explore new material(s) that may be considered as the alternative of lead-based solar cell materials in terms of properties and performance. To do this, the structural features, mechanical, thermodynamic, electronic, and optical properties of Pb-free MHPs, $CsMI_3$ (M = Mg, Ga, Ca, Ba, and Sr) have been investigated. It is found that $CsMgI_3$ could be a potential alternative to $CsPbI_3$ for photovoltaic applications.

1.1 Background

Perovskite materials

In recent years, the creation of inexpensive, highly efficient solar cells has taken center stage. A promising type of solar cells called perovskite solar cells (PSCs) have gotten a lot of attention in the last ten years. This is because they have a high absorption coefficient, good bipolar charge mobility, a long carrier diffusion length, low exciton binding energy, low trap state density, and a tunable bandgap. This image shows some organic and inorganic halide perovskite compounds. The general chemical formula for metal halide perovskites is typically ABX_3, where X is a halogen anion, B is a metal cation, and A is an organic cation. Cl, Br, I, or their mixture often form the halogen anion, while methylammonium (MA), formamidinium (FA), Cs, or their mixture typically compose the organic cation. The B cation has been the subject of numerous previous studies. Here the B elements, which can be found in the highlighted portions of the cubic phases perovskite materials and are shown in the

periodic table of Fig. (1.1). Fig (1.1) using different colours, are the building blocks of all B elements for cubic phases perovskites.

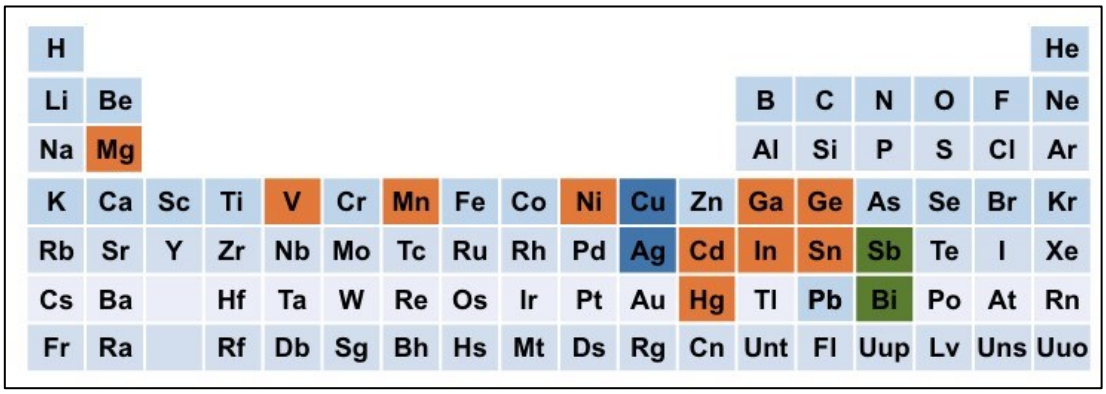

Figure 1.1: All currently known cubic phase perovskites are composed of B elements. Possible replacement elements for lead (Pb). The periodic chart [44] displays the orange coloring of the screened elements by Filip et al. that can substitute Pb. Researchers have also computed or demonstrated that the blue coloration of transition metal elements and the green shading of heterovalent elements in the VA group can serve as substitutes for lead.

1.2 Crystal structures of Perovskite compounds

Perovskites, which have the generic chemical formula ABX_3, have a cubic structure. The idealized cubic structure places "A" cations at the cube corner, "B" cations at the body center, and halogen atoms at the face center. The idealized shape is a seldom-found cubic structure (space group PM3m, no. 221). The type "A" atom is positioned at cube corner position (0, 0, 0) in the idealized cubic unit cell of this compound; the type "B" atom is positioned at body-center position (1/2, 1/2, 1/2); and the halogen atoms are positioned at face-centered locations (1/2, 1/2, 0), (1/2, 0, 1/2), and (0, 1/2, 1/2).

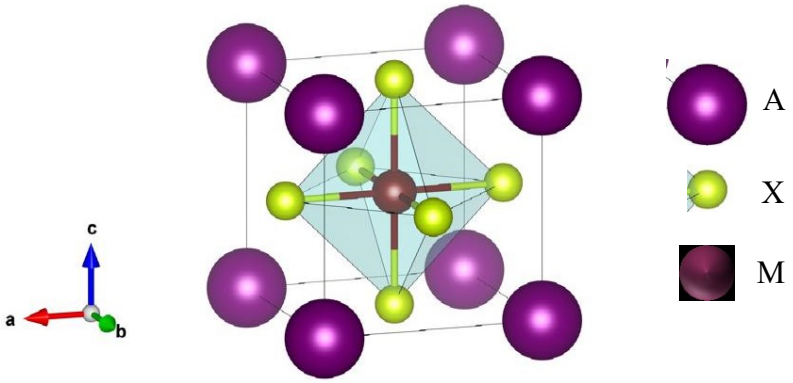

Figure 1.2: Unit cell of a perovskite structure (cubic).

1.3 Perovskite materials classification

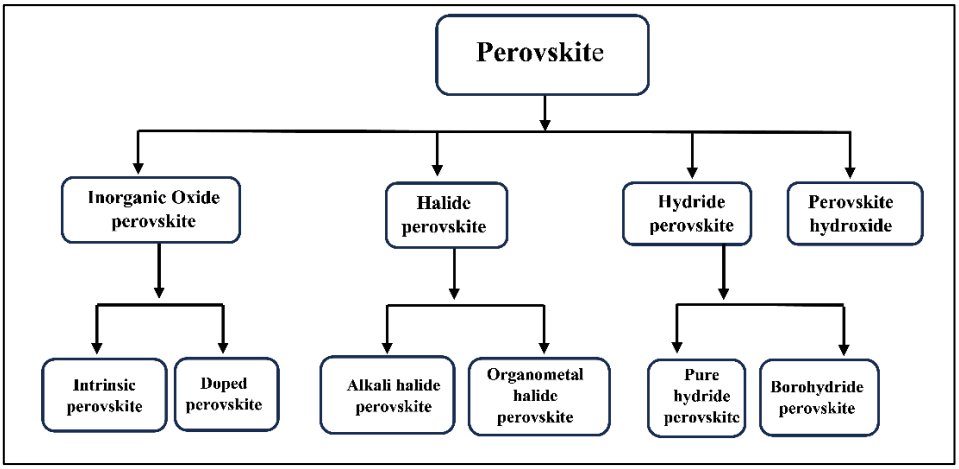

Figure 1.3: Classification of perovskites, according to anion X.

The perovskites can be classified as the following compound types (Fig. 1.3). Inorganic oxide perovskites, including intrinsic perovskites and doped perovskites in terms of chemical elements on their specific sites. The oxygen vacancies in perovskite oxides are easily manipulated by doping. Halide perovskite, including alkali halide perovskites and organometal halide perovskites. Halide perovskites structured with the general formula ABX_3 (where A=Cs, B= Pb, Sn, X=Cl, Br and I) gained remarkable attention because of the superior optical properties.

Some details of the applications are presenting in the following (Fig. 1.4).

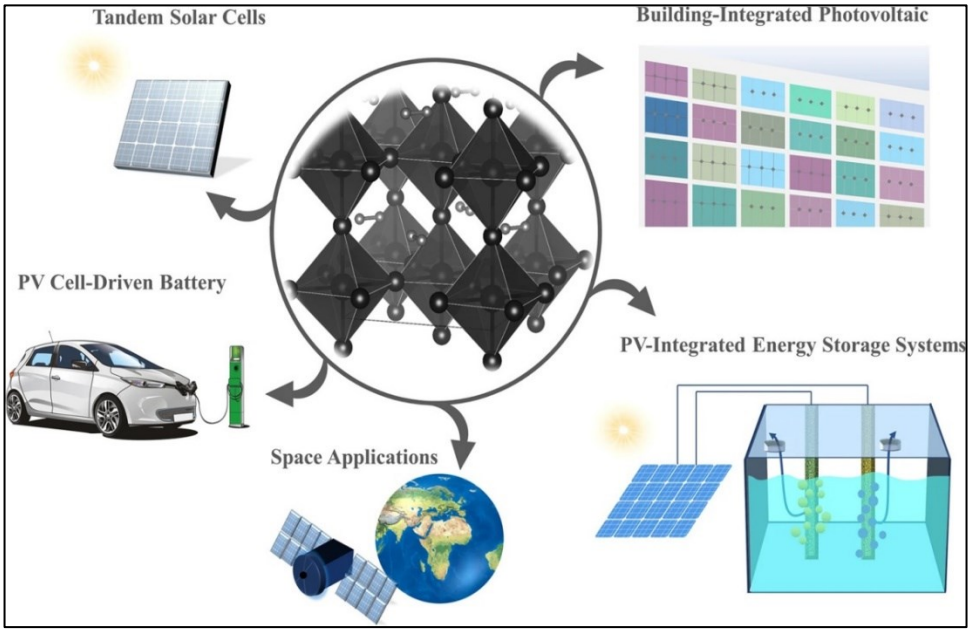

Figure 1.4: Possible Perovskite phase applications. [Communications Materials ISSN 2662-4443 (online)]

1.4 Context

To recommend a compound for technological applications, conceptually thorough research of the physical properties of materials is needed. Among these, a material's suitability for practical application can be determined by performing a dynamical stability and mechanical stability examination. Furthermore, it has been important to consider the materials as the foundation of many industrial applications that can be determined readily by the thermodynamic properties because of the compounds' resilience at high temperatures and pressures. For instance, the materials' considerable energy dependence on the refractive index and absorption coefficient as a result of these features is crucial for optoelectronic devices. Furthermore, the reflectivity is a crucial quality to mention when selecting coating materials to reduce solar heating [45]. Investigation of various $CsMI_3$ (M = Pb, Mg, Ga) Perovskite phase characteristics is therefore anticipated.

As a result, we plan to look at optoelectronic analysis, solid solution analysis and supercell analysis in addition to the material properties of considered compounds. We found that the majority of papers focused on the optoelectronic and elastic properties of the Perovskite phase. Vickers hardness, thermodynamic properties have not been taken into consideration.

Numerous studies of the Perovskite phases have been conducted, both theoretically and experimentally, but only a handful have been completed. There are many investigations on the compound $CsMgI_3$ and a few investigations on compound $CsGaI_3$ and $CsMg(I_{1-x}Br_xCl_x)_3$ combination with Cl and Br created by solid solution or super cell. Despite their technological importance. $CsGaI_3$ has not yet been synthesized or thoroughly researched, unlike the phases $CsPbI_3$ and $CsMgI_3$, which have both already been created.

The physical qualities of a compound must be thoroughly investigated theoretically in order to recommend it, particularly for technological applications. The study of a material's dynamical stability is crucial for practical application under high pressure and temperature circumstances. Additionally, the thermodynamic properties offer significant additional data about how materials behave under high pressures and temperatures, which is thought to be the foundation of many industrial applications [46]. The electronic characteristics of materials, which display the electronic reaction of the materials exposed to radiation, are intimately related to the optical properties. In order to develop very efficient solar cells and other optoelectronic devices, it is important to study carefully a set of physical characteristics such as optical and mechanical properties. Energy band morphology, which has several physical characteristics including the band structure and density of states are necessary for an effective development of photovoltaic as well as optoelectronic devices. Also, information on light-absorption capacity, reflectivity spectra and photoconductivity are required for efficient performance of device.

Secondly, it will be useful to investigate other properties including strength of failure mode (comprised of brittleness-ductility and elastic anisotropic behavior) thermal characteristics so that the full potential use in photovoltaic and optoelectronics applications is understood. Thus, we intend to perform a detailed study on the Lead-free metal halide perovskite $CsMI_3$ (X= Mg and Ga) compounds respects to the structural, electronic, optical, and mechanical

properties. We will also focus on their thermal properties to learn more about how they could be applied in coating technology.

Therefore, both from research and an application standpoint, it is desirable to explore these physical characteristics of $CsMI_3$ (M = Mg, Ga) Cubic phases to replace lead (Pb).

We feel compelled to thoroughly explore $CsMI_3$ (M = Mg, Ga) Cubic phases' dynamical stability, thermodynamics, and optical properties for the first time. In addition, the structural, elastic, and electronic properties are discussed along with charge density mapping and solid solution as well as supercell combination with Cl and Br of $CsMgI_3$ compound.

1.5 Aim and objectives

Aim:

The goal of this study is to provide a detailed analysis of the lead-free metal halide perovskite $CsMI_3$ (M= Mg, Ga) compounds where $CsPbI_3$ is a mother compound covering their structural characteristics as well as electronic properties, optical features, mechanical parameters, stability and thermal aspects. First of all, it is necessary to assess the feasibility of using these compounds in photovoltaic and optoelectronic applications as well as solar cell application. The primary goal is a detailed study of their properties to find out the appropriate applicants to substitute Lead (Pb).

Objectives:

- Employ DFT-based CASTEP for studying the crystal structure, and find out lattice parameters of $CsMI_3$ perovskite compounds.
- Analyze the phase stability, electronic band structure and density of states along with the band gap anomaly of $CsMI_3$ compounds to determine their utility in visible light absorbing semiconductor materials.
- Optical properties of the perovskite compounds, such as light absorption capability and reflection spectra should be analyzed to determine their suitability in optoelectronic applications.
- Assess the mechanical properties of $CsMI_3$ compounds, such as hardness, mode of failure (brittleness/ductility), and elastic anisotropic nature to determine structural integrity and reliability.

- Discuss the thermodynamic properties of $CsMI_3$ compounds such as thermal conductivity, coefficient of linear expansion and thermal stability to grasp their behavior under different temperature environments and application in coating technology.
- Discuss about the lead-free solid solution of $CsMg(I_{1-x}Cl_x)_3$ and $CsMg(I_{1-x}Br_x)_3$; where (x= 0, 0.1, 0.2, 0.3, 0.4, 0.5, 0.6, 0.7, 0.8, 0.9 1) along with mechanical and electronic properties.
- Carry out an analysis of the lead-free supercell $CsMg(I_{1-x}Br_x)_3$ where (x= 0, 0.25, 0.50, 0.75, 1) along with mechanical, electronic as well as optical properties.

- Go through an analysis of the collected data and make conclusions about $CsMI_3$ lead-free perovskite compounds for photovoltaic and optoelectronic applications.

1.6 Thesis Outline:

- Chapter 1: Introduction, challenges, and potential applicability of solar energy in addressing global energy demand with the structure, classification, history and application of perovskite materials.
- Literature Review will be discussed in chapter 2.
- Chapter- 3: Computational methods in details will be discussed in this chapter.
- Chapter-4: Results and discussion of the studied compounds will be discussed in this chapter.
- Conclusions: Summary of the findings of the research will be discussed concisely in this chapter.

Chapter 2: LITERATURE REVIEW

2.1 Literature review of the previous works

Solar power, which goes by the name of solar energy as well, makes up only 2% of the world's total energy supply and consumption. However, this paltry percentage informs us of something great – if we can address the most significant problems in that sector a massive opportunity is waiting to be unleashed.

Because of the rapid changes in the global economic and social landscape, now require more energy than traditional fossil fuels can provide. Solar energy will undoubtedly offer a variety of benefits, like being renewable and pollution-free, given that it is destined to be the primary energy source in the 4IR. In nature, metal halide perovskites (MHP) are commonly accessible and reasonably priced. Consequently, solar cells based on these materials would be more economical and efficient than silicon-based photovoltaic (PV) technology[1,47]. Due to their remarkable opto-electronic properties—which include a tunable bandgap, high optical absorption, broad absorption spectrum, small carrier effective mass, long charge diffusion length, and high charge carrier mobility [8,48] the MHPs have recently attracted a great deal of attention from the scientific community. ''The power conversion efficiency (PCE) of PSCs based on lead (Pb) perovskites has been dramatically improved from the initial 3.8% to recently certified value of 25.2% ''[14,49] ''Devices based on lead halide perovskites have reached power conversion efficiencies of >22%, [18] rivalling established solar cell materials including cadmium telluride (CdTe), copper indium gallium selenide (CIGS), and single-crystal Si''. ''The archetypal hybrid organic-inorganic halide perovskite, $CH_3NH_3PbI_3$, has a bandgap near the Shockley-Quessier optimum [18,50] strong absorption in the visible spectrum''[21,22] ''long carrier lifetimes'', [24] and ''high charge carrier mobilities ''. Consequently, $CH_3NH_3PbI_3$ can act both as a light absorber and as an efficient charge transporting layer in a solar cell. One of the major concerns, however, is the toxicity of lead. "The use of lead is particularly problematic because lead perovskites tend to decompose in ambient conditions, releasing harmful compounds such as PbI_2 [28]**".** However, there exist unavoidable shortcomings in these Pb-based high-efficiency PSCs (e.g., $MAPbI_3$, $FAPbI_3$, $Cs_{0.05}$ $FA_{0.85}$ $MA_{0.10}$ Pb $(I_{0.97}$ $Br_{0.03})_3$), that is, the element lead is toxic to the environment and organisms and difficult to discharge from the body. "Research indicates that the contamination of lead ions to soil and water sources is permanent and generates a very serious negative impact on human, animal, and plant survival [30,31,50] **(**Since lead can enter a person's body, bind with an enzyme, and then accumulate in soft tissues and bones

like the spleen, kidney, liver, and brain through blood circulation". "Lead poisoning eventually causes functional abnormalities in the nervous, digestive, and circulatory systems of the affected person. Typically, most persons begin to exhibit signs of lead toxicity when their daily lead intake reaches 0.5 mg [30,31]". Therefore, in order to ensure that the natural environment for humans is secure and free from pollution, certain non- or low-toxic metal ions must be developed to replace lead as PSC perovskite absorbers [32,51].

"The general chemical formula for metal halide perovskites is typically ABX_3, where X is a halogen anion, B is a metal cation, and A is an organic cation [38,52] [40,42,53,97]. Here, the organic cation usually includes methylammonium (MA), formamidinium (FA), Cs, or their mixture, and the halogen anion consists of Cl, Br, I or their mixture. For B, previous work has showed that less toxic ions like Sn^{2+}, Bi^{3+},Ge^{2+}, Sb^{3+}, Mn^{2+}, and Cu^{2+} could be used as an alternative ion to Pb^{2+} in perovskites to constitute a new lead-free perovskite structure [12]".

The addition of these metal cations improves PSCs' ecologically beneficial qualities while also broadening the variety of perovskite species. This study summarizes the theoretical basis of current work and focuses mostly on several lead-free perovskite materials and associated solar cell applications. We used first-principles Density Functional Theory (DFT) to look at Pb-free inorganic metal halide perovskite compounds and figure out what their general properties are. The main purpose of this study is to compare the mechanical, electronic, optical, thermodynamic, and structural features of $CsMI_3$ (M=Mg, Ga) metal halide perovskites that don't contain lead to those that do contain lead in $CsPbI_3$. We have selected the elements Mg and Ga to replace Pb due to their similar chemical composition and vacancy in the periodic chart.

Furthermore, these materials are inexpensive and abundant in the natural world. As a result, solar cells made of these materials would be more economical and effective than photovoltaic (PV) technology based on silicon. These remarkable properties enable the use of this semiconductor family not only in solar cells but also in light-emitting diodes, photodetectors, and solar-to-fuel energy conversion devices, among other electronic devices [1,5,11,12]. In order to forecast a specific device application and advancements, a more profound and basic understanding of the semiconductor features is required. It is therefore

crucial to research the mechanical, optical, and electronic aspects as well as comprehend the system's general features.

To gain a deeper comprehension of the electronic properties of materials, it is imperative to investigate the optical properties of solids. The way a material reacts to light can also be found out by studying its optical functions. Therefore, a thorough understanding of the optical parameters is necessary for a material to be used in practical optoelectronic devices like solar cells, diodes, lasers, etc. However, very few studies have been conducted on the optical properties of the considered perovskite compounds. In particular the optical properties of $CsMI_3$ where (M=Mg and Ga) materials are still unexplored in detail. Predicting the significance of these materials for industrial applications also requires an understanding of their mechanical characteristics, such as their ductility, rigidity, and mechanical stability. To the best of our knowledge, the elastic constants and moduli of the Pb-free $CsGaI_3$ compound is still not reported. In order to obtain appropriate Pb-free perovskites for solar cells and other optoelectronic devices, we have thus taken into consideration a few metal halide perovskite compounds and examined their structural, electronic, optical, thermodynamic, and mechanical properties using first-principles Density Functional Theory (DFT). "Ten compounds out of 248 candidates have been identified for possible solar cell applications with high-throughput screening [44]**.** They could be able to tune band gap between 0.9 and 1.7 eV (1.7 eV for $CsMgI_3$, 1.5 eV for $CH_3NH_3MgI_3$ and 0.9 eV for $CH(NH_2)_2MgI_3$) and low electron effective mass, which is caused by exceptionally dispersive conduction bands. Some suggested lead-free Perovskites (M=Mg and Ga) where Mg is alkaline- earth metal and Ga is p-block element were optimized here for the predictability of optoelectronic properties for making these compounds acceptable for optoelectronic and photovoltaic application[53]"**.**

In this study, we aimed to detail study of the structural, electronic, mechanical, optical and thermal properties of Pb-free inorganic metal halide cubic perovskites $CsMI_3$ (M= Mg and Ga) for optoelectronic and photovoltaic applications by First-principle calculation. This development signifies a significant step forward in solar energy technology, promising enhanced renewable energy conversion capabilities [54].

In 2009, Kojima et al. introduced yet another highly efficient solar cell, utilizing the perovskite semiconductor based on lead (Pb), which increased power conversion efficiency (PSCs) from 3.8% to 25.2%. This progress highlights the continuous advancement in

Table 2.1: Summary of some Perovskite compounds and their band gap.

Compounds	Experimental Band Gap	Band Gap (eV) (using DFT)
$CsPbI_3$	1.73 [42]	1.475 [This], 1.51 (PBE) [55]
$CsPbBr_3$	2.3 [56]	2.07 (PBE)[55]
$CsSnI_3$	1.31 [57]	0.59 (PBE)[55]
$CsSnBr_3$	1.75 [57]	0.64 (PBE) [55]
$CsGeI_3$	1.53 [58]	1.17 (PBE) [55]
CsGeBr3	2.32 [58]	1.48 (PBE) [55]

renewable energy technology, potentially making solar power more practical and impactful in our energy lands[59].

Table 2.1 presents the findings of previous investigations into perovskite compounds. It is evident that in the majority of cases, their band gaps fall within the visible range. This characteristic renders chalcopyrite highly suitable for photovoltaic application.

This specific attribute underscores their potential to serve as efficacious semiconductors for absorbing visible light. As a result, these materials emerge as compelling candidates with promising applications in the realm of optoelectronics.

Now the landmark progresses on efficiency evolution of perovskite solar cells are presenting below in Fig. 2.3 [60].

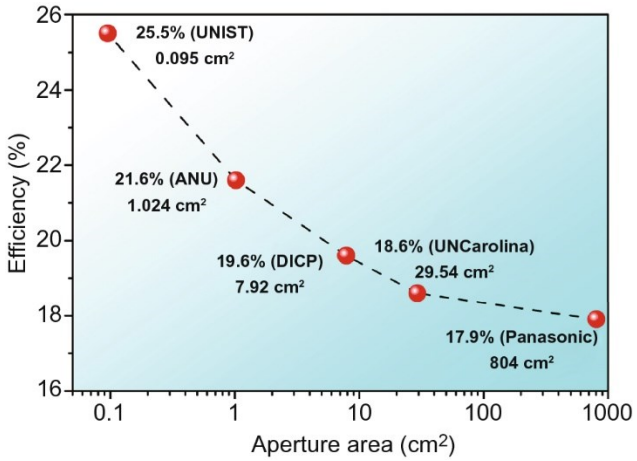

Figure 2.1: The landmark of PSC.

Table 2.2: Summary of the previous studies of $CsMI_3$ (M= Pb, Mg and Ga).

Compound	Structural	Mechanical	Stability	Optical	Thermal	Electronic	Ref.
$CsPbI_3$	Yes	Yes	No	Yes	No	Yes	[61]
$CsMgI_3$	Yes	Yes	No	Yes	No	Yes	[62]
$CsGaI_3$	No	No	No	No	No	No	[33]

Moreover, being characterized by lower thermal conductivity, perovskite serves the purpose of heat transfer restrain and offer better insulation properties. The unique combination of good optoelectronic properties and excellent thermal insulating ability makes perovskite promising candidates for a variety of applications as advanced materials beyond their basic capabilities in optical and electronic.

Therefore, this expedition of discovery and trial has revealed that we can do many things with light. Scientists are discovering better materials and patterns to capture sunlight and convert it into energy. It is like a gigantic puzzle and every new discovery brings us nearer to the use of solar power in incredible ways.

2.2 Motivation for the present work

Prior research by this work has focused on the goal to perfect solar energy conversion and identify novel perovskite compounds, particularly exploring cubic crystalline structures of $CsMI_3$ semiconductors. The goal is to improve solar cell performance by utilizing their peculiarities, particularly the appropriate band gap for light absorption at visible wavelengths. First, the structural, electronic and optical properties could be studied elaborately in order to check the suitability of these materials as an absorbing material. Furthermore, the mechanical, thermal and stability properties could also study to broaden the applicability of perovskite materials beyond energy harvesting. Their low thermal conductivity, which implies potential for use in TBC systems to improve insulation and thermal protection. This work seeks to achieve sustainable material applications by harnessing the merged optical and thermals qualities of perovskite materials.

Chapter 3: Computational methodology

3.1 Introduction

Compared to other methods, ab initio calculations can produce high-quality quantitative predictions for a variety of systems. In order to investigate structural and electronic properties, calculations were made using the ab initio plane wave pseudo potential (PW-PP) method within the framework of density functional theory (DFT) [63] implemented in CASTEP code [64]. The present chapter goes into great detail about these exacting mathematical processes used in ab initio approaches.

3.2 Ab initio method

The phrase "ab initio" means "from the beginning" and is derived from the Latin words "ab" (from) and "initio," an ablative of initium (beginning).

The most common categories of ab initio techniques are: Hartree-Fock (HF) method [65–67] and DFT [63,68]. We are concentrated only for DFT in this study.

3.2.1 Density functional theory (DFT)

The two theorems that Hohenberg and Kohn proved in 1964 [69] and the computational scheme that Kohn and Sham (KS) proposed the following year [70] form the foundation of density functional (DF) techniques. They demonstrated how the electron density affects the overall energy. This means that the essential concept in density functional theory. Electron density are must be understood instead of the challenging many electron wave function.

Theorem 1 (Uniqueness): The exact ground state electron density □o(***r***) is a unique functional of the ground state expectation value of any observable. This indicates that it is possible to compute all of the system's properties in the ground state if the electron density and functional are known. In particular, the ground state energy $E_o[\square_o(\boldsymbol{r})$ can be calculated.

Theorem 2: The principle of variation the total energy functional *E* [□]. is minimized by (r). Thus, with a specific external potential generated by a set of nuclear charges, the second theorem offers a variational condition for calculating □o(r) and Eo [□] jointly. e.g.

$$V(\boldsymbol{r}) = -\sum_{i,j=1}^{N_{el}N_{at}} \frac{Z_j}{|r_i - \boldsymbol{R}_j|}$$

E_0 is found by minimizing an expression of the form [20]:

$$E[\rho(\boldsymbol{r})] = \int \rho(\boldsymbol{r}) V(\boldsymbol{r}) d\boldsymbol{r} + \frac{1}{2}\int \frac{[\rho(\boldsymbol{r})\rho(\boldsymbol{r}')]}{|\boldsymbol{r} - \boldsymbol{r}'|} d\boldsymbol{r} d\boldsymbol{r},$$

$$+\int \rho(\boldsymbol{r})\, g(\mathbf{r};[\rho])\, d\mathbf{r} + \sum_{i,j=1}^{N_{at}N_{at}} \frac{Z_i Z_j}{|\boldsymbol{R}_i - \boldsymbol{R}_j|}$$

$$= E_{ext} + E_j + E_{kxc} + E_{Rep} N_{uc} \tag{3.1}$$

with regard to an arbitrary function, r, which stands for the density of n electrons. The self-consistent field (SCF) method is used in the Kohn and Sham (KS) method to determine the ground state energy as follows:

1. For the one-electron effective Hamiltonian, the n/2 lowest eigen values and related Eigen functions (orbitals) are discovered:
2. $$\hat{h_{eff}}\psi_i(\boldsymbol{r}) \equiv \left[-\frac{1}{2}\nabla^2 + Ve_{ff}(\boldsymbol{r})\right]\psi(\boldsymbol{r}) = \varepsilon_i \psi_i(\boldsymbol{r}) \tag{3.2}$$

1. The calculation of density, $\rho(\boldsymbol{r})$:

$$\rho(\boldsymbol{r}) = 2\sum_{i}|\Psi_i(\boldsymbol{r})^2|$$

2. The re-calculation, V_{eff} as a function of the density, $\rho(\boldsymbol{r})$:

$$V_{eff}(\boldsymbol{r}) \;\; V(\boldsymbol{r}) + \int \frac{\rho(\boldsymbol{r}'}{|\boldsymbol{r}-\boldsymbol{r}'|}d\boldsymbol{r}' + \mu_{xc}(\boldsymbol{r};[\rho]) \tag{3.3}$$

Where $\mu_{xc}(\boldsymbol{r};[\rho])$ is the exchange-correlation potential.

3. If self-consistency is not reached, go to step 1.

4. At self-consistency, $\rho(\boldsymbol{r})= \rho_0(\boldsymbol{r})$ (GS density) and the ground state energy can be calculated by the following equation,

$$E_0 = E_{kps} + \int \rho_0(\boldsymbol{r})V(\boldsymbol{r})d\boldsymbol{r} + \frac{1}{2}\int \frac{\rho_0(\boldsymbol{r})\rho_0(\boldsymbol{r}')}{|\boldsymbol{r}-\boldsymbol{r}'|}d\boldsymbol{r}\,d\boldsymbol{r}$$

$$+E_{xc} + E_{Rep}N_{uc} \tag{3.4}$$

where the pseudo-kinetic energy, E_{kps} is defined by,

$$E_{kps} \;=\; \sum_i \int \psi_i\,(\boldsymbol{r})^* \left(-\frac{1}{2}\nabla^2\right)\psi_i(\boldsymbol{r})d\boldsymbol{r} \tag{3.5}$$

and the exchange-correlation energy, E_{xc} is expressed as,

$$= E_{ext} + E_j + E_{kxc} + E_{Rep}N_{uc} \tag{3.6}$$

The Effective Core Potential (ECP) can be calculated by the following equation [71]:

$$E^{DFT} = \int \varepsilon^{DFT}(\boldsymbol{r})\mathrm{d}\boldsymbol{r} \tag{3.7}$$

is a precise integration that must be used to determine the electron-electron interaction's contribution to energy in the periodic density functional theory (DFT) within the linear combination of atomic orbitals (DFT-LCAO) approach [72].

3.2.2 Local density approximation (LDA)

Typically, an LDA for the exchange-correlation energy in a spin-unpolarized system is expressed as,

$$E_{xc}^{LDA}[\rho] = \int \rho(\boldsymbol{r})\epsilon_{xc}(\rho)d\boldsymbol{r} \tag{3.8}$$

Where ρ is the electronic density and ϵ_{xc}, the exchange-correlation energy density, is a function of the density alone. The exchange-correlation energy is decomposed in to exchange and correlation terms linearly,

$$E_{xc} = E_x + E_c \tag{3.9}$$

so that separate expressions for E_x and E_c are sought.

3.2.3 Generalized gradient approximation (GGA)

The Generalized Gradient Approximation (GGA) has been used in this study's DFT calculations. Local density approximation is less effective than the generalized gradient approximation (GGA). The GGA has shown to outperform LDA in systems where the charge density is slowly changing. It also applies to the inhomogeneous electron gas system. The exchange-correlation energy E_{xc} is a function of the spin density and their gradients [72] and can thus produce the more relevant results.

$$[\rho\alpha, \rho\beta] = \int[\rho\alpha(\boldsymbol{r}), \rho\beta(\boldsymbol{r}), \nabla\rho\alpha(\boldsymbol{r}), \nabla\rho\beta(\boldsymbol{r})]d\boldsymbol{r} \tag{3.10}$$

The introduction of GGA is intended to greatly raise the caliber of LDA results.

3.3 Pseudopotentials

What is the pseudopotential? It tries to replace the complicated effects of the motion of an atom's core (i.e., non-valence) electrons and its nucleus with an effective potential, or pseudopotential. This way, the Schrödinger equation will show the modified effective potential term instead of the Columbic potential term for core electrons that is normally there. Hans Hellmann developed the pseudopotential approximation in the 1930s.

There are two types of Pseudo potentials:

1. Norm-conserving pseudopotential
2. Ultrasoft pseudopotential

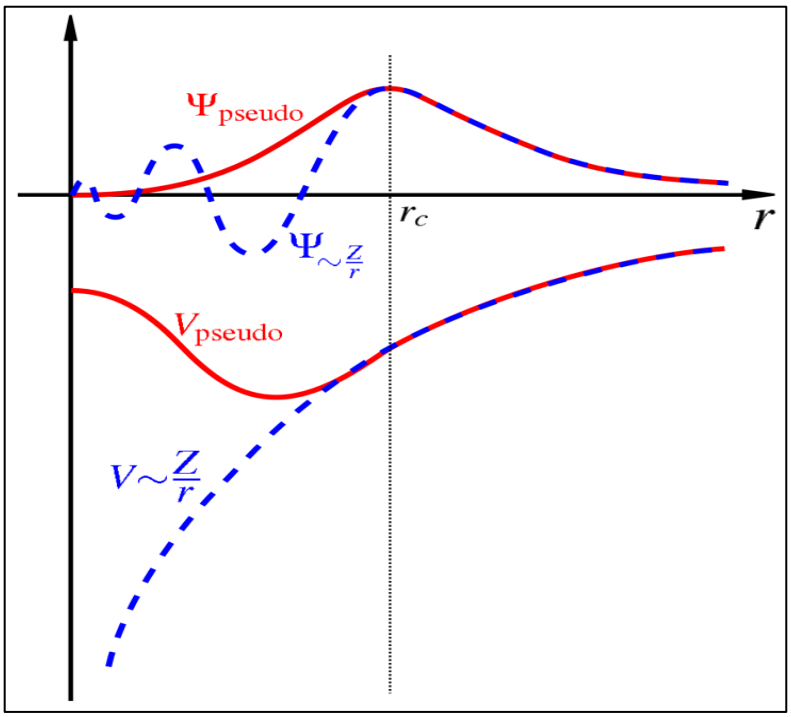

Figure 3.1: The pseudo-potentials and all-electron potentials, together with their corresponding radius, r_c—the separation between the two potentials—are depicted in the diagram.

3.4 CASTEP code

The current DFT [73] -based computations were performed using the CAmbridge Serial Total Energy Package (CASTEP) algorithm by the Materials Studio 8.0 module. This method has proven to be one of the most accurate methods for the calculation of electronic structures [74]. For all computations, the pseudopotential of Vanderbilt type [75] was utilized to handle the electron-ion interaction. Using the generalized gradient approximation (GGA) of Perdew-Berke-Ernzerhof (PBE) [76], the exchange-correlation energy was calculated. The Broyden–Fletcher–Goldfarb–Shanno (BFGS) [77] minimization approach was applied in order to maximize the crystal structure and determine the ground state energy. The finite

strain theory [78], which was implemented within the CASTEP module, was used to derive elastic constants. By varying the M cations, all of the characteristics of $CsMI_3$ (M = Pb, Mg, and Ga) were calculated. For all cubic $CsMI_3$ computations, the electronic wave function with a cutoff energy of 500 eV was utilized. The irreducible Brillouin zone was sampled using 11 × 11 × 11 *k*-point grids following the Monkhorst-Pack technique [79]. The current computations were conducted with the following convergence limits: 1×10^{-6} eV/atom for total energy, 0.03 eV/Å for maximum force on atoms, 0.001 Å for maximum atom displacements, and 0.05 GPa for maximum stress. The flow chart for the solving Kohn-Shams equation as follows:

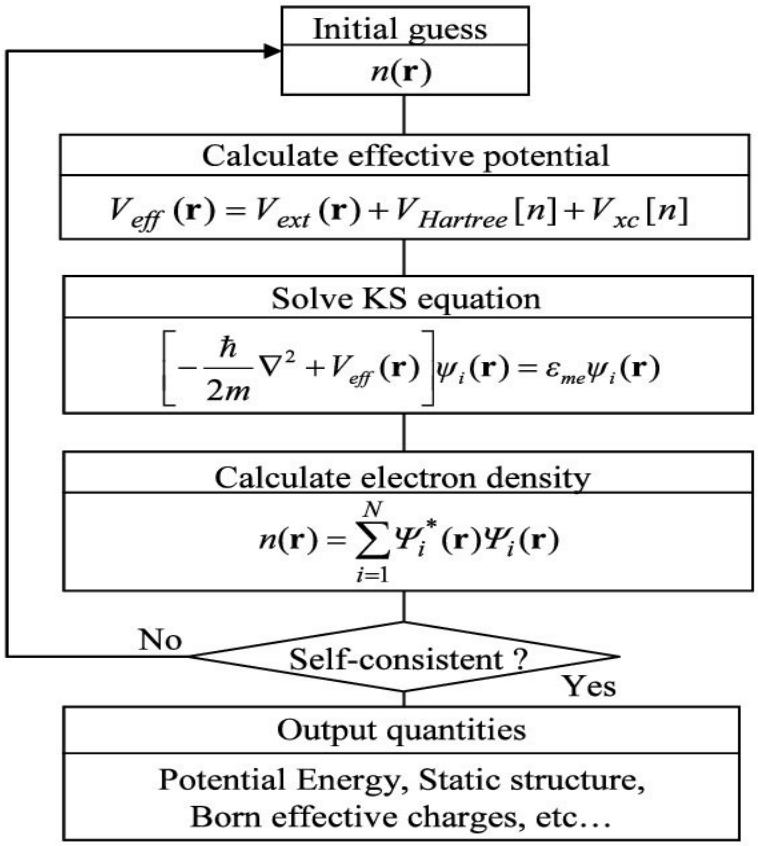

Figure 3.2: Self consistency in Khon-Sham Scheme.

We have examined the system's ground state electron density. With the aid of additional potentials, this density is utilized to compute the effective potential (V_{eff}), also known as the Kohn-Sham potential. In order to compute the Kohn-Shams equation for non-interacting particles, the V_{eff} is added to the Hamiltonian. Our program is finished if the newly computed electron density satisfies our requirement; if not, it will continue to calculate until convergence is reached. Whenever we achieve final energy where the system is converged, we would be able to calculate other properties of the system.

3.5 Supercell

In this study, we constructed 2 × 2 × 2 nonstoichiometric supercells of $CsMg(I_{1-x}Br_x)_3$ where X= (0, 0.25, 0.50, 0.75, 1) with 40 non-equivalent atoms as well as defect structures with Iodine and Bromine vacancy using Pm3m (no. 221) space group. After optimization there appears a triclinic distortion in the structure 2 × 2 × 2 $CsMg(I_{1-x}Br_x)_3$ supercell. For different combination of 2 × 2 × 2 supercell, results vary with different values in lattice parameter and in unit cell volume. Fig. 3.2 shows a supercell with 40 atoms. Once the vacancies are generated, the structure were fully relaxed to the equilibrium configuration.

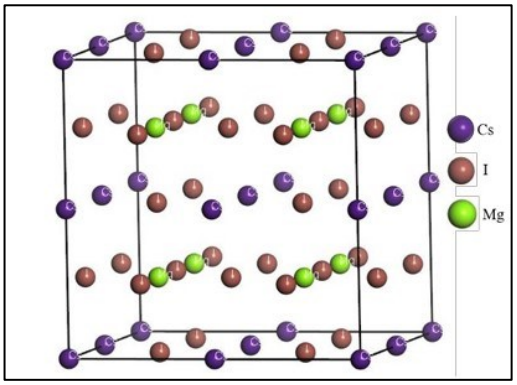

Figure 3.3: Slightly distorted triclinic structure of supercell $CsMg(I_{1-x}Br_x)_3$;(x=0, 0.25, 0.50, 0.75, 1).

Chapter 4: RESULTS AND DISCUSSION

4.1 Structural properties and phase stability

4.1.1 Structural properties

The $CsMI_3$ (M = Pb, Mg and Ga) compounds crystallize in the cubic system with space group Pm3m (no. 221). As seen in Fig. 4.1, the material's unit cell is made up of five atoms with a single formula unit. Within the structure, the Cs atom is positioned in the corner with a 1a Wyckoff site and (0, 0, 0) fractional coordinates; M is positioned in the body center with a 1b Wyckoff site and (1/2, 1/2, 1/2) fractional coordinates; and the I atom is positioned in the face center with a 3c Wyckoff site and (0, 1/2, 1/2) fractional coordinates. Ray [43] also reported the orthorhombic phase of stoichiometric $CsMI_3$ (M = Pb, Mg and Ga), but the cubic phase has been considered in this study using the available refinement data. The lattice parameters and internal coordinates were completely loosened in order to improve the geometry by switching the M site cation. PBE functional is used to compute the optimal lattice parameters and cell volume of $CsMI_3$ substances, as seen in Fig. 4.2. The hybrid DFT functionals, like HSE06, can correctly predict some experimentally measured band gaps in some materials but the structural properties, like lattice parameters are significantly deviated from the experimental values. It is well known that the calculation of the accurate lattice parameter is one of the key factors to predict the physical properties using DFT calculations accurately [80]. However, it is found that the properties of the HSE06 functional differed from those of other functionals, like PBE, PBEsol, GGA, and LDA. Because of this, PBE is used as a benchmark in the calculations to account for the correctness of the results.

It should be noted that $CsPbI_3$ is calculated for comparison of our studied samples as this is well known and detail studied system.

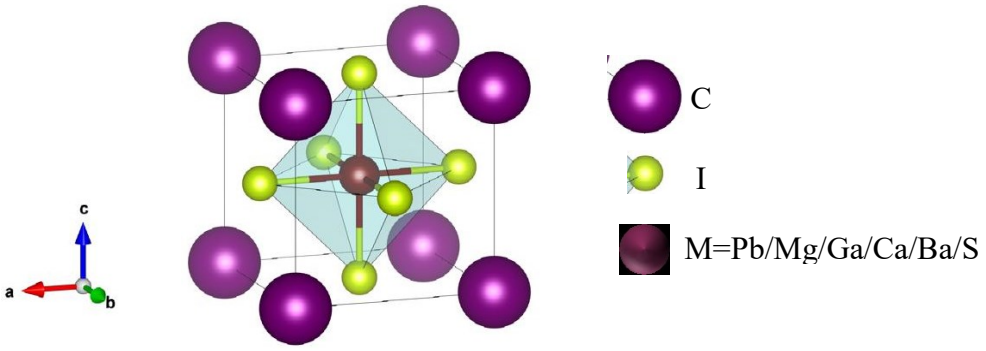

Figure 4.1: Cubic crystal structure of $CsMI_3$ metal halide perovskite compounds, (M= Pb, Mg and Ga).

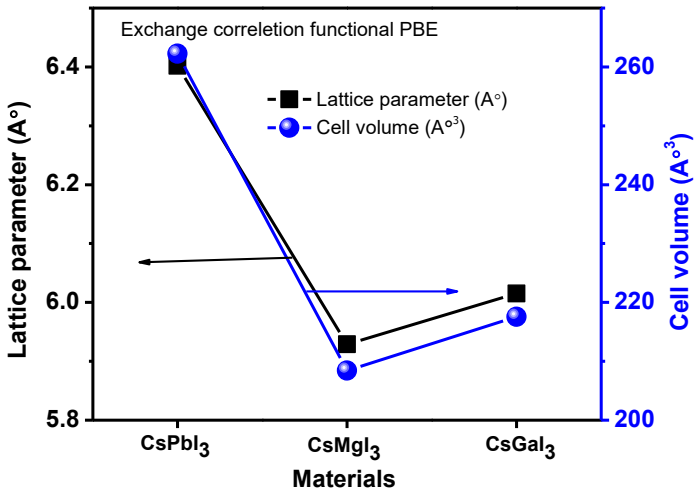

Figure 4.2: Lattice parameter (Å) and cell volume ($Å^3$) of the metal halide perovskites (MHP) crystal structure of $CsMI_3$ (M= Pb, Mg and Ga).

4.1.2 Dynamical stability

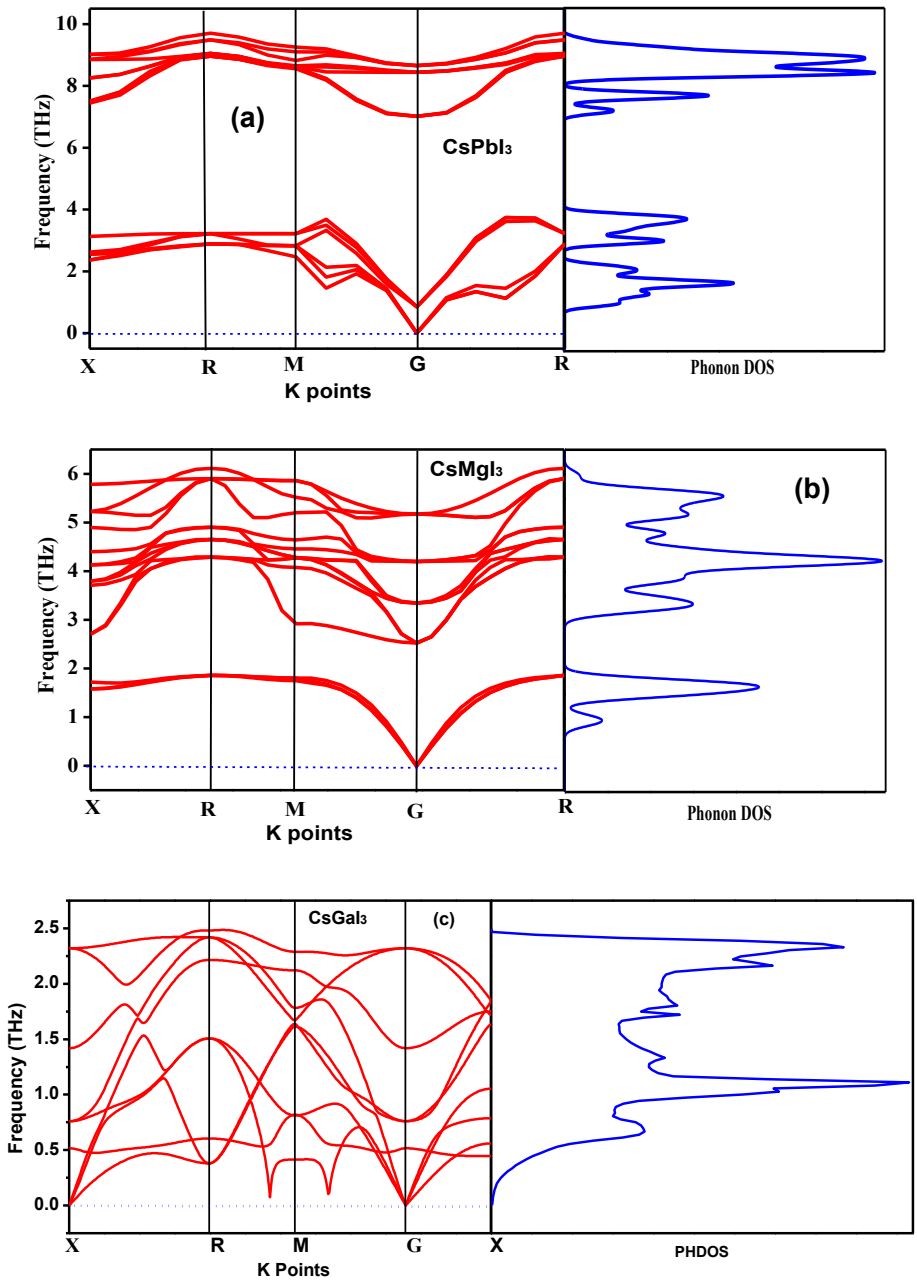

Figure 4.3: Phonon dispersion curves and phonon density of states (DOS) of (a) $CsPbI_3$ (b) $CsMgI_3$ and (c) $CsGaI_3$ compounds.

Comprehending the behavior of phonons is critical to describe mechanical, thermodynamic properties dynamic spectroscopic and acoustic characteristics in a crystal at finite temperatures. As shown in Fig. 4.3, we have presented phonon dispersion curves for some selected high symmetry directions that represent the vibrational nature of the compound. The present study is the first on this particular compound ($CsMgI_3$ and $CsGaI_3$) those have not been analyzed previously due to its vibrational properties. Hence, the predicted results provide an invaluable perspective about vibrational dynamics of these compound.

Dynamic stability of a material is an important criterion for assessing its appropriateness in real-world settings involving time-varying external stimuli. It is likely that materials that are formed at any temperature will not always be stable. For example, materials formed at high temperatures could not be stable when brought to a lower temperature. The phonon frequency is dependent on the temperature of the crystal lattice. To confirm the stability of the synthesized perovskite at low temperature, the phonon dispersion curve (PDC) is calculated in the ground state using the density functional perturbation theory (DFPT) finite-displacement approach. The phonon frequency that is used to evaluate stability over the whole Brillouin Zone (BZ) is displayed in Fig. 4.3 (a-c) for compounds $CsMI_3$ (M = Pb, Mg and Ga) PDC. Negative frequencies at any *k*-point indicate the instability of the compounds, whereas positive frequencies indicate their stability[81,82]. Fig. 4.3(a-c) shows that none of the compounds exhibit imaginary or negative frequencies, indicating that they are dynamically stable. This finding aligns with the section on structural attributes, which states that all phases under study have a negative formation energy. This suggests that the compounds might potentially be produced by experimentation. Five atoms make up the unit cells of the perovskite phases, leading to 15 phonon branches, 12 of which are optical modes and 3 of which are acoustic modes. Acoustic modes stay at the bottom of the phonon dispersion curves, whereas optical modes make up the top branch. Acoustic branches are created by in-phase vibrations of atoms in a lattice outside of their balance position. The calculated total phonon density of states (PHDOS) for $CsMI_3$ is shown in Fig. 4.3 (a - c). The sources of the PHDOS peaks include the bands' general flat appearance and the fact that the overall DOS peak is lower in lower bands because of their dispersive nature.

One interesting result of this work is that there are no soft modes in any one of the phonon branches covering the Brillouin zone. This observation implies that the compounds should be thermally and mechanically stable in a dynamic nature. The fact that there are no soft modes in the phonon spectra means that the compound does not change its structure, undergoes phase transition due to thermal fluctuations or weak external effects.

So, a combined analysis of phonon DOS and PDC allows us to obtain a complete picture of the lattice dynamical properties in our compounds under study.

4.1.3 Thermodynamic stability

The chemical stability of $CsMI_3$ can be confirmed by analyzing their formation energies. The subtraction of the total energies of pure constituent atoms from the total energy of the materials in their stable structures determines the formation energy (E_f). The following expression is used to estimate the formation energy of $CsMI_3$ [83]**:**

$$\Delta E_f(CsMI_3) = [E_{tot}(CsMI_3) - E_s(Cs) - E_s(M) - 3E_s(I)] \qquad (4.1)$$

Here, $E_{tot}\ (CsMI_3)_{fu}$ represents the total energy per formula unit and is given by $E_{tot}\ (CsMI_3)_{fu} = 1/N[E_{tot}(CsMI_3)_{cell}]$, where N denotes the number of formula units per unit cell. E_s(Cs), E_s(M), and E_s(I) are the total energies per atom of the pure elements Cs, M, I, respectively, in their ground-state solid phases. So, the $\Delta E_f(CsMI_3)$ per atom is given by $\Delta E_f(CsMI_3)_{fu}/N_t$, where N_t denotes the total number of atoms in one formula unit, gives the desired parameter. The calculated formation energies of perovskites $CsMI_3$ are found to be $CsMgI_3$(-1.81 eV/atom) > $CsPbI_3$(-1.624 eV/atom) > $CsGaI_3$(-1.326 eV/atom). The values are negative indicating the compounds are energetically stable to be synthesized. The particulars are presented Table- 4.1 that are used to calculate the formation energies of $CsMI_3$ (M = Pb, Mg and Ga) compounds.

Table 4.1: Some particulars to calculate formation energy E_f.

Phase	ID	Space Group	F.E(eV)	No. of atom	F.E(eV/atom)
Cs	mp-639727	$P6_3/mmc(194)$	-0.044	4	-0.011
Cs	mp-1183694	14/mmm(139)	-0.02	2	-0.01
Cs	mp-1	Im3m(229)	-0.02	2	-0.01
Cs	mp-1055940	Fm3m(225)	-0.164	4	-0.041
Cs	mp-573579	Cmce(64)	-0.864	16	-0.054
Pb	mp-20483	Fm3m(225)	0	4	0
Pb	mp-20745	$P6_3/mmc(194)$	-0.04	2	-0.02
Pb	mp-22692	Pm3m(221)	-0.04	2	-0.02
Mg	mp-153	$P6_3/mmc(194)$	0	2	0
Mg	mp-110	Pm3m(221)	-0.08	2	-0.04
Mg	mp-1056351	14/mmm(139)	-0.076	2	-0.038
Ga	mp-142	Cmce(64)	0	8	0
Ga	mp-569423	143d(220)	-1.2	12	-0.1
Ga	mp-140	14/mmm(139)	-0.256	2	-0.128
I	mp-639751	Immm	0	2	0
I	mp-601148	14/mmm(139)	-0.138	2	-0.069
I	mp-684663	Im3m(229)	-0.79	2	-0.395
$CsPbI_3$	-	Pm3m(221)	-8.12	5	-1.624
$CsMgI_3$	-	Pm3m(221)	-9.05	5	-1.81
$CsGaI_3$	-	Pm3m(221)	-6.63	5	-1.326

The negative values of the calculated formation energies (shown in Table 4.1) also confirm that $CsMI_3$ compounds are thermodynamically stable. Interestingly, only the calculations of formation energy with respect to the convex hull are exclusively used for defect systems. Considering the calculated values (shown in Table 4.1), we may state that $CsMI_3$ is thermodynamically stable.

Fig. 4.4 illustrates all formation energy values are below the critical line starts from 0, confirming the phase/chemical stability of our calculated compounds.

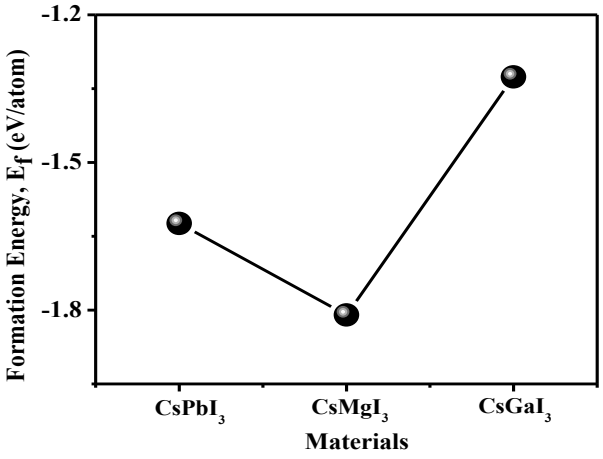

Figure 4.4: Formation energies E_f of $CsMI_3$ (M = Pb, Mg and Ga) compounds.

4.2 Mechanical Properties

For industrial applications of engineering materials, the research of various physical properties such as elastic anisotropy, brittle and ductile nature, and elastic moduli is essential. The linear finite stress-strain method in the CASTEP algorithm yields the elastic constants C_{ij} [78]. Table 4.2 shows the three independent elastic constants for cubic $CsMI_3$ that were calculated: C_{11}, C_{12}, and C_{44}. The Born stability criteria, which are frequently expressed in terms of C_{ij} and therefore based on free energy considerations, may be used to derive the elastic constants, which are crucial to forecasting the mechanical stability of a crystal [84]. The spinodal, shear, and Born conditions for mechanical stability of a cubic crystal are $C_{11} + 2C_{12} > 0$, $C_{11} - C_{12} > 0$, and $C_{44} > 0$, respectively. It is analogous to requiring a positive bulk modulus, B, to apply the spinodal criteria. Therefore, for a cubic crystal to be mechanically stable, its phases must have positive values for the elastic constants B, $C_{11} - C_{12}$, and C_{44}, as shown in Table 4.2. An elastic material's propensity to deform non-permanently in various directions when subjected to stress is determined by this feature. Information regarding the bonding behavior of solids is also provided by the elastic constants. The elasticity along the axial length is given by the elastic constant C_{11}. Therefore, the value of C_{11} may be used to represent the elastic stiffness of materials against the ⟨100⟩ uniaxial strain of the (100) plane. The elastic constants C_{12} and C_{44} stand for the pure shear stress in the (110) plane along the ⟨110⟩ direction and the shear stress in the (010) plane along the ⟨001⟩ direction, respectively.

Table 4.2 shows that, in comparison to the other compounds, $CsPbI_3$ has the highest value of C_{11}. The computed value of C_{11} for all perovskites is greater than C_{12}, which is noteworthy because it suggests that the bonding strength in $CsMI_3$ is stronger along the ⟨100⟩ direction than it is along the ⟨110⟩ direction. Table 4.2 provides an overview of the different elastic characteristics, which are computed from the single-crystal zero-pressure elastic constants using established relationships [85]. These values include the bulk modulus, B, shear modulus, G, Young's modulus, Y, and Poisson's ratio, v. Rakita et al. found the elastic moduli experimentally for $CsPbI_3$ [86]. The bulk modulus determines the average bond strength of the component atoms in a material [87]. Through observation of the bulk modulus of 101 GPa, Rahaman et al. recently found moderate bonding strength in $LiCuBiO_4$ [83]. However, the bulk moduli of 190 GPa and 171 GPa, respectively, indicated significant bonding strength in ScIrP and ScRhP, according to Nasir et al. [88]. As a result, the computed values of B in the 19.65 – 11.39 GPa range (Table 4.2) may indicate that the atoms in $CsMI_3$ have weak bonding strengths, and these are soft materials in nature. Table 4.2 also shows that changing the cations from Pb to Mg increases the bulk modulus, however it decreases for the Ga. The cationic size increases the bulk modulus of $CsMI_3$ by decreasing the compounds' compressibility and creating a dense solid. The necessary resistance to volume deformation under external pressure is also provided by the binding strength of atoms. On the other hand, the G measures how a solid change in form, and it shows a significant correlation with the hardness of the material. As the value of G increases, the material gets stiffer. The solid matter's resistance to heat shock is influenced by Young's modulus, Y. In relation to Y, the critical thermal shock coefficient changes inversely [61]. The better the thermal shock resistance, the higher the value of the thermal shock coefficient. Thermal shock resistance is a determining factor in the selection of a material for a thermal barrier coating (TBC). Because of its notably reduced Young's modulus, $CsMI_3$ may be a good choice for a TBC material. Higher values of G and Y denote stiffness, whereas the computed value of Y (28.24 – 12.20 GPa) suggests that $CsMI_3$ is moderately flexible [89–91]. In addition to being helpful in explaining the mechanical characteristics of solids, the moduli of elasticity, such as G, B, and Y, are also a reliable way to gauge the hardness. Of the measured elastic constants, C_{44} is the most accurate in predicting the hardness of materials. Furthermore, among the moduli of elasticity, the shear modulus (G) is thought to be the most accurate indicator of hardness. Table 1 makes it clear that $CsMgI_3$ is more durable than the other compounds examined in

this investigation. The hardness calculations using Chen's formula [92] support these claims. Table 1 presents the estimated values of macro and micro hardness, which are in line with previous predictions based on C_{44} and G values. Mazhnik and Oganov [93] show favorable agreement between the theoretical and experimental hardness values of various materials computed using Chen's formula. It is commonly known that superhard materials such as diamond (H_V = 96 GPa), BC_2N (H_V = 76 GPa), and BC_5 (H_V = 71 GPa) are utilized extensively [93]. Therefore, the fact that $CsMI_3$ has a substantially lower hardness than superhard materials verifies that the compounds under study are not hard materials. Vickers hardness, however, is primarily a measure of the material's resistance to plastic deformation. A knowledge of a solid's hardness can lead to the prediction of many significant applications for useful devices. Additionally, a thorough comprehension of the mechanical behavior may be attained by examining the connection between hardness and elastic polycrystalline modules. Table 1 shows the assessed Vickers hardness values for $CsMI_3$ (M = Pb, Mg, Ga, Ca, Ba, and Sr). This table makes it very evident that $CsMgI_3$ is less hard than $CsPbI_3$ and that $CsGaI_3$ is tougher than $CsPbI_3$. Even so, compared to the most stiff materials (Vickers hardness 70 to 150 GPa) [94], the hardnesses of the titled compounds are low. Because of this, all $CsMI_3$ compounds show signs of being soft and flexible, which qualify them for thin-film fabrication. The cutting capacity of a compound, the maximum financial level of machine operation, and plastic strain—which are essential for industrial applications—are represented by the machinability factor of the materials under investigation, which is calculated by the formula $U_M = B/C_{44}$ [95]. With the exception of $CsMgI_3$, which indicates better lubricating characteristics and lower frictions and has important applications in a variety of industries, all U_M values are more than 2. In addition, failure mode research—that is, determining whether a material is brittle or ductile—is crucial for technology. The Pugh's ratio (B/G) value indicates if a material is ductile (> 0.75) or brittle (< 0.75) [96]. Table 4.2 displays all titled compounds as ductile materials, with the exception of $CsMgI_3$, which is characterized as being near the ductile−brittle transition line. Frantsevich et al., however, also suggested a critical value of Poisson's ratio ($\nu \sim 0.26$) for distinguishing between the brittle and ductile nature of solids [97], as illustrated in Fig. 4.5.

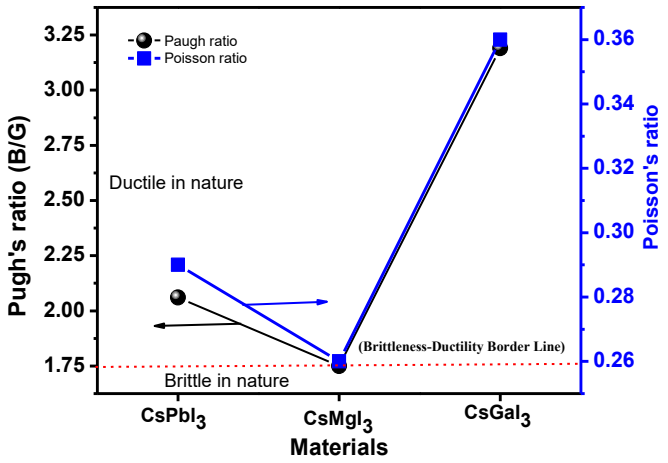

Figure 4.5: Pugh's and Poisson's ratio of the perovskites and the horizontal red dashed line distinguish the brittle and ductile materials.

The calculated values of ν **(**Fig. 4**)** again confirm that the $CsMI_3$ compounds are purely ductile except $CsMgI_3$ because of its position below the ductile-brittle transition line. However, the Cauchy pressure, defined as $C_{12} - C_{44}$, is another indicator of failure mode of materials [98]. If the Cauchy pressure is negative, then the material is expected to be brittle; otherwise (having a positive Cauchy pressure), it is a ductile one [98]. Hence, in this study, all $CsMI_3$ compounds are assumed to be ductile in accordance with the aforementioned three indicators. The Kleinman parameter (ξ) measures the ease of bond bending to bond stretching. In general, the value of ξ can be between 0 and 1 ($0 \leq \xi \leq 1$) and is estimated using the following expression [99]**:**

$$\xi = \frac{C_{11}+8C_{12}}{7C_{11}+2C_{12}} \qquad (4.2)$$

Kleinman reported that the upper limit corresponds to minimize the bond bending term, and the lower limit corresponds to a minimized bond stretching term [100]. The calculated values of ξ for $CsMI_3$ compounds are shown in Table 4.2. The estimated value of ξ of ~0.50 for $CsMI_3$ compounds is in good agreement with the previously reported value of ξ of ~0.55 for perovskite $LaAlO_3$ [101]. The calculated value of ξ suggests the strong bonding nature of $CsMI_3$, which is dominated by both bond bending and bond stretching contributions.

Table 4.2: The Elastic constants, Cij (GPa), Bulk Moduli, B (GPa), Shear Moduli, G (GPa), Young's Moduli, Y (GPa), Pugh's ratio, Poisson's ratio, Kleinman Parameter (ξ), Cauchy pressure, Machinability index U_M, and shear anisotropy (A).

Parameter	$CsPbI_3$	$CsMgI_3$	$CsGaI_3$	References
C_{11}	39.54 34.23	34.81	29.22	This work [35]
C_{12}	6.68 4.46	12.07	7.05	This work [35]
C_{44}	5.34 4.24	11.09	2.24	This work (64)
B	17.64 14.38 23 19.8 14.4	19.65	14.44	This work [35] [102] [103] [104]
G	8.55 6.30 7.9	11.2	4.53	This work [35] [104] Exp.
Y	22.07 14.49 20.1	28.24	12.31	This work [35] [104] Exp.
B/G	2.06	1.75	3.19	This work
ν	0.29 0.33	0.26	0.36	This work [104] Exp.
Kleinman Parameter (ξ).	0.32	0.49	0.39	This work
Cauchy Pressure (GPa)	1.34	0.98	4.81	This work
$U_M = B/C_{44}$	3.3	1.77	6.45	This work
A	0.67	0.20	0.60	This work

The values of C_{44} are related to shear anisotropy factor (Zener ratio) A, that is defined by the following formula [105]

$$A = \frac{G}{Y/[2(1+\nu)]} = \frac{2C_{44}}{C_{11} - C_{12}}$$

The value of A, as illustrated in Table 4.2, designates the anisotropic nature of the compounds with the possibility of deformation and the appearance of microcracks. The value of A is unity for completely isotropic material, and any deviation from unity (smaller or greater) denotes the degree of anisotropy. The computed values of A (Table 4.2) indicate the anisotropic nature of the compounds under study.

4.3 Electronic properties

4.3.1 Electronic Band Structures

The electronic band structure of the compounds provides insight into the electronic characteristics of solids. Fig. 4.6 (a-c) shows the electronic band structures of $CsMI_3$ compounds that have been computed using the GGA-PBE potential. Note that a hybrid potential such as HSE (Heyd-Scuseria-Ernzerhof) [80] might provide more accurate estimate. However, deviation has been discovered for some compounds, thus it is not ideal. As a result, determining a suitable potential to forecast the theoretical electronic band gap for this system of materials remains difficult. The electronic structures of $CsPbI_3$ and $CsGaI_3$, compounds show direct band gaps at the R, M, and Γ points of the Brillouin zone and remaining $CsMgI_3$ has illustrated indirect band gaps. The high symmetry paths of *k*-points in the Brillouin zone are selected as X-R-M-G-R. In the instance of GGA-PBE, it is till obtained an enhanced band gap of 1.48 eV, 1.12 eV and 1.74 eV for $CsPbI_3$, $CsMgI_3$ and $CsGaI_3$ respectively, with respect to the band gap range that is suitable for solar cells. The zero-energy level in Fig. 4.6 (a-c) is selected to be the Fermi energy, E_F. It is noted that thinner devices are possible

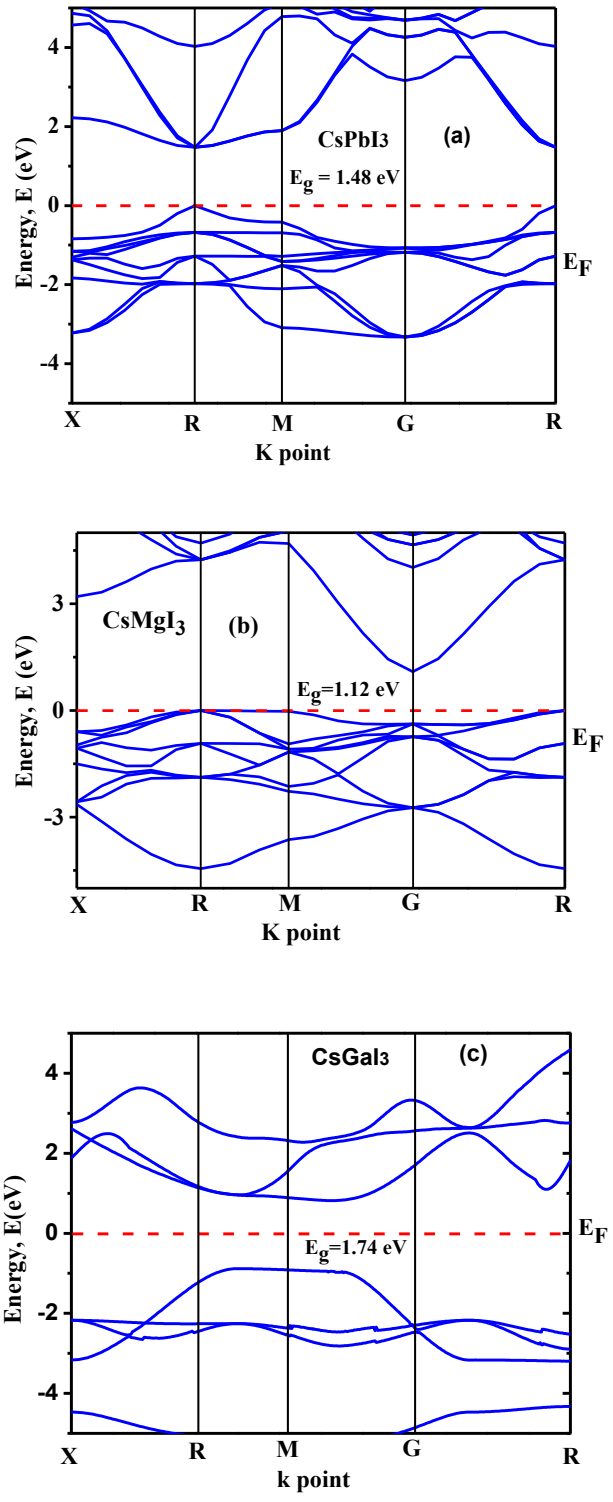

Figure 4.6: Band structures of (a) $CsPbI_3$ (b) $CsMgI_3$ and (c) $CsGaI_3$ compounds.

because photovoltaic materials with direct band gaps absorb light more easily than those with indirect gap. However, compared to indirect bandgap materials, direct bands also experience greater rates of radiative recombination. Therefore, optimizing the absorption properties along with the direct or indirect nature and suppression of radiative recombination of material is important for solar cell applications as absorbance or active materials [106].

4.4 The density of states (DOS)

In order to obtain a more detailed understanding of the type of compounding nature of the compounds we have showed the total and partial DOS in Fig. 4.7. In addition, combined DOS analysis demonstrates the specific atomic and orbital contributions to the electronic structure of $CsMI_3$ (M= Pb, Mg and Ga). This data is especially helpful for determining atomic interactions and bonding types in the compound, as well as predicting and explaining its physical properties.

The partial density of states (PDOS), total density of states (DOS), and atomic contributions to the band formation of $CsMI_3$ compounds have all been computed for a better understanding. The calculated DOS of the studied sample $CsMI_3$ (M= Pb, Mg, Ga) compounds are represented in Fig. 4.7 (a, b), where they are almost identical. The DOS makes it clear that every compound has n-type carriers with a distinct peak for the electron crossing at E_F. Because it is metallic, $CsGaI_3$ has a particularly negative class of carriers among them. Figure 4.7 (a, b) show that for the compounds from left to right, the total DOS below the E_F increases. Conversely, this value decreases for the compounds in ascending order. Furthermore, the *p* orbital of the halogen atom is the primary source of the total DOS below the E_F. Furthermore, Pb-6*p*, Mg-2*p*, and Ga-4*p*, were the major contributors from the *p* orbital of M atoms to the total DOS below the E_F. The E_F is thought to be at 0 eV in DFT, however due to calculation errors and a very little shift to the left side (valence band edge) rather than the right side (conduction band), it appears that there is a DOS at the E_F.

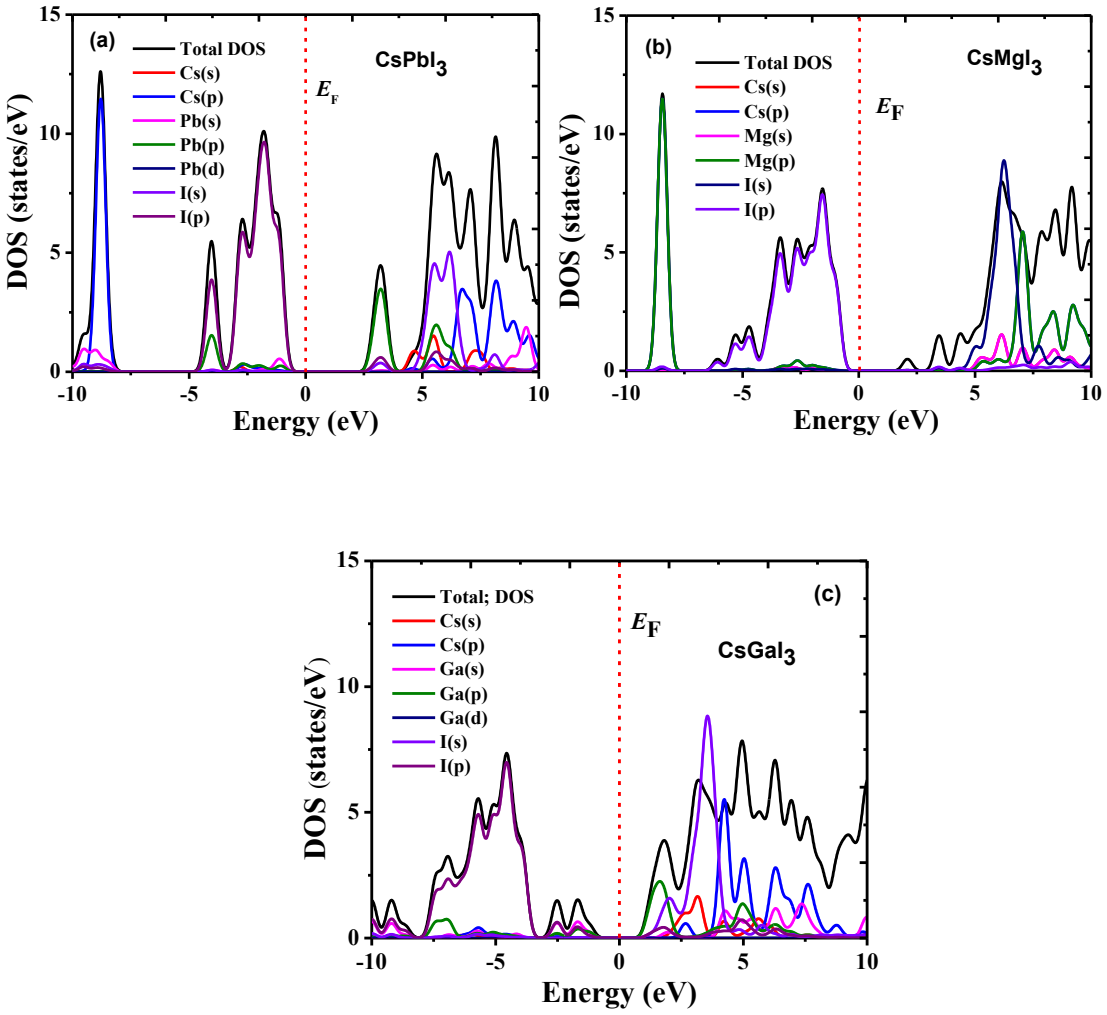

Figure 4.7: Total and partial densities of states of perovskites (a) $CsPbI_3$ and (b) $CsMgI_3$ and (c) $CsGaI_3$.

4.4.1 The Charge Density

To see how the overall electronic charge density is spread out in $CsMI_3$ compounds, look at Fig. 4.8, which displays the charge density maps of valence electrons. The scale to the right displays the electron density and intensity. The color blue indicates a low electron density, whereas the color red indicates a high electron density. Figure 4.8 makes it clear that the charge density distribution surrounding each and every atom in $CsMI_3$ compounds is almost

spherical. This result suggests that $CsMI_3$ molecules are ionic. The compounds' metallic properties also have an impact on their ionic properties.

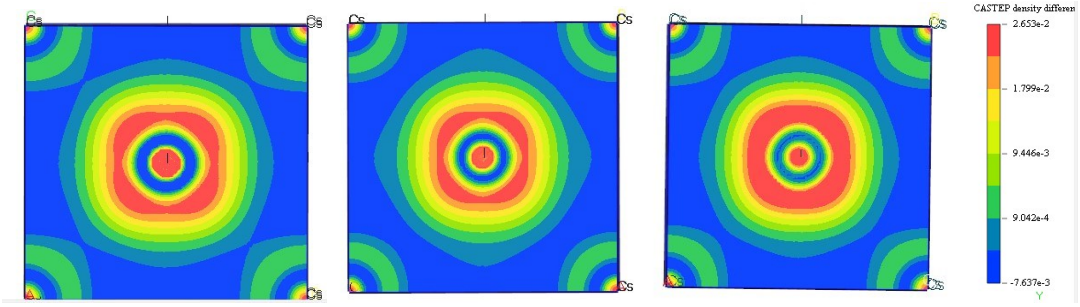

Figure 4.8: Charge Density Mapping of $CsMI_3$ perovskite compounds where (M= Pb, Mg and Ga).

4.5 Optical properties

An essential optical constant that sheds light on how a substance absorbs light over a specific distance is the absorption coefficient [107]. The absorption behavior is contingent upon several elements, including the molecular structure and band gap of the crystal. Specifically, optical absorption occurs when photon frequency entering the material is equal to the frequency of electronic transition in the material. Materials may selectively absorb photons at particular frequencies due to the variation in the absorption coefficient with frequency. Electronic transitions within the full states of the highest valence band and the empty states of the lowest conduction band are what cause the selective behavior. Efficiency in conversion is provided by the materials' absorption of photons. The absorption coefficient $\alpha(\omega)$ may be computed using the subsequent formula:

$$\alpha(\omega) = \left[\sqrt{\varepsilon_1^2(\omega) + \varepsilon_2^2(\omega)} - \varepsilon_1(\omega)\right]^{\frac{1}{2}} \quad (4.3)$$

Crystalline materials' optical characteristics can be characterized by the complex dielectric function, $\varepsilon(\omega) = \varepsilon_1(\omega) + i\varepsilon_2(\omega)$; where $\varepsilon_1(\omega)$ and $\varepsilon_2(\omega)$ which has real and imaginary components, respectively.

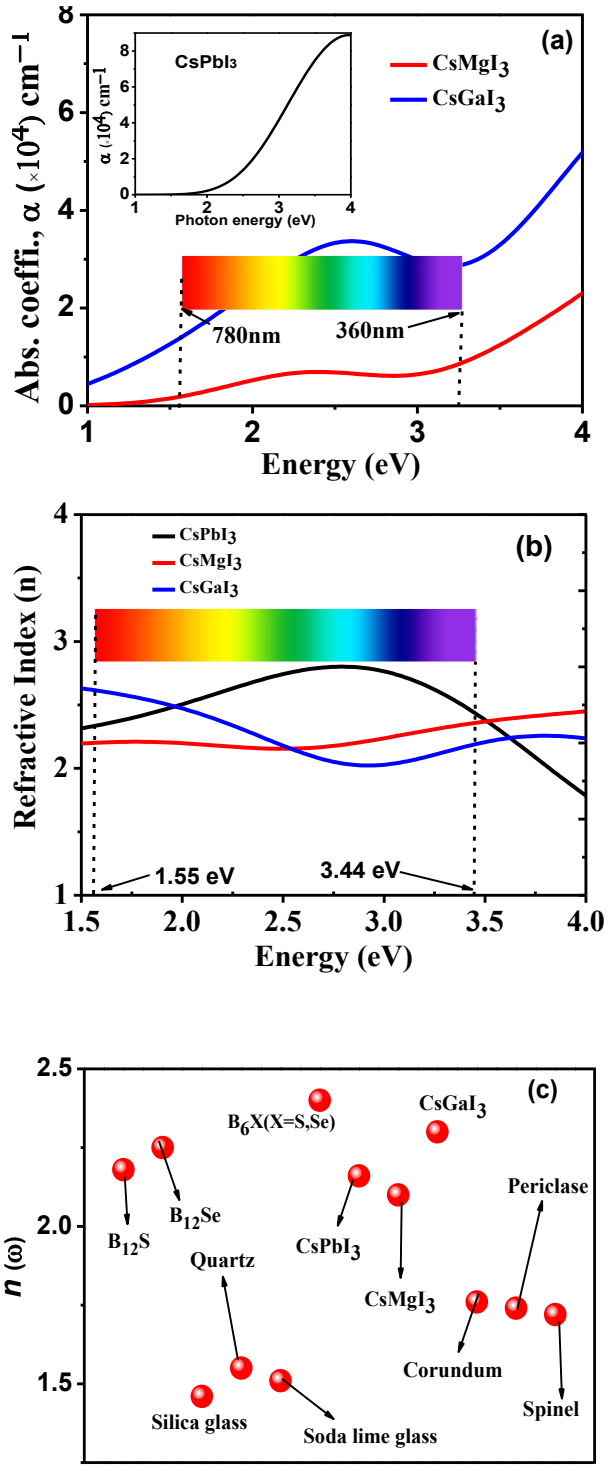

Figure 4.9: Photon energy dependent absorption (a) and refractive index (b) of the $CsMI_3$ (M= Pb, Mg and Ga) perovskite. (c) Comparison of the static refractive index, n at 1.55 eV of $CsMI_3$ with some other well-known ceramic and optical wave guide materials.

Fig. 4.9 (a) displays the absorption coefficient with photon energy. In addition to explaining how incident light is absorbed by a material, the α(ω) also clarifies how emergent

light decays through the medium, providing information on the attenuation of electromagnetic radiate [108,109]. It also provides information on the ideal solar energy conversion efficiency, which is crucial for the practical use of a material in solar cells. Additionally, for the compounds $CsPbI_3$ the value of α(ω) is zero at 0 eV, but it is non-zero for $CsGaI_3$ and $CsMgI_3$. Because all of the light will pass through zero absorbance substances (at 0 eV), they will be optically transparent in the areas where there is no light absorption. Of the three compounds that might be substituted for the Pb, $CsMgI_3$ exhibits absorbance in the visible range, with a value of 7.0×10^3 cm^{-1} at 2.36 eV.

The propagation of an electromagnetic beam or light through a compound may be explained from the behavior of $N(\omega) = n(\omega) + ik(\omega)$, where n(ω) represents the real refractive index and $k(\omega)$ is the extinction coefficient. For each compound, the n(ω) curve is shown in Fig. 4.9(b). It provides further details on how much incident light is bent or refracted as it travels through a material medium [109,110]. At 1.55 eV, the refractive indices for $CsPbI_3$, $CsMgI_3$, and $CsGaI_3$ are 2.3, 2.2 and 2.6, respectively. The $n(\omega)$ values begin to decrease after the peak positions, suggesting less interaction with the photons. Additionally, it is evident that the n(ω) curve and the $\varepsilon_1(0)$ spectra have similar natures due to their strong correlation, as shown by the formula $n(0) = \sqrt{\varepsilon_1(0)}$ [108].

The complex dielectric function, $\varepsilon(\omega) = \varepsilon_1(\omega) + i\varepsilon_2(\omega)$, which represents the real and imaginary parts of the dielectric function, respectively, may be used to explain the optical characteristics of crystalline solids. To compute further optical constants, one must know the imaginary portion of the dielectric function [111]. Using the selection rules [112], we can figure out the imaginary part of the dielectric function by looking at the momentum matrix elements for the occupied and unoccupied wave functions. It can be expressed as follows:

$$\varepsilon_2(\omega) = \frac{2\pi e^2}{\Omega \varepsilon_0} \sum_{k,v,c} |\langle \psi_k^c | u.r | \psi_k^v \rangle|^2 \delta(E_k^c - E_k^v - E) \qquad (4.4)$$

A given k is used to find the phonon frequency (ω), electronic charge (e), volume (Ω), unit vector ($\boldsymbol{u}$) along the polarization of the input electric field (Ω), and wave functions ψ_k^c and ψ_k^v. By applying the Kramers-Kronig relations, we can infer the real component of the dielectric function from the imaginary component. The remaining optical functions, as listed in the literature [113], can be obtained by using the real and imaginary parts of the dielectric

functions $\varepsilon_1(\omega)$ and $\varepsilon_2(\omega)$. These functions include the refractive index n (ω), extinction coefficient k (ω), absorption coefficient α (ω), energy-loss function L (ω), optical conductivity σ (ω), and reflectivity R (ω). If we look at Fig. 4.10(a,b), it can be seen the real $\varepsilon_1(\omega)$ and imaginary $\varepsilon_2(\omega)$ dielectric functions of three metal halide perovskites [M = Pb, Mg, and Ga].

The position of the real component of the dielectric function's peak is related to electron excitation in this study, and interband transitions are the main source of the peak. It is generally known that for metallic systems, intraband changes from the conduction electrons, particularly in the low-energy infrared region, dominate the real component of the dielectric function. However, due to the semiconductor character of $CsMI_3$ in the current work, interband transitions determine the dielectric function. The real component of dielectric function $\varepsilon_1(\omega)$ for $CsPbI_3$, $CsMgI_3$, and $CsGaI_3$ compounds exhibits two peaks and a shoulder in Fig. 4.10(a). For $CsGaI_3$, $CsPbI_3$, $CsMgI_3$ the static real dielectric constant values [at zero energy or $\varepsilon_1(0)$] are 6.8, 4.8, and 4.4 correspondingly. The $\varepsilon_1(\omega)$ value of $CsMgI_3$ is nearly constant in the visible range (1.58–3.26 eV), as can be seen in the figure. The values of $\varepsilon_1(\omega)$ are found to be 7.6, 6.2 and 7.1 at 2.7, 4.8 and 0.92 eV for $CsPbI_3$, $CsMgI_3$ and $CsGaI_3$. In the higher energy range, $\varepsilon_1(\omega)$ gradually decreases after reaching its apex. Additionally, it turns negative for all of the perovskites at around 9 eV, indicating that they resist strong plasmonic stimulation and behave like metals in this area. The imaginary dielectric function [Fig. 10(b)] provides insight into the state transitions that occur from occupied VB to empty CB [109,110]. Furthermore, the UV regime is where the highest values and a few additional lesser peaks are also reached. The peaks of $\varepsilon_2(\omega)$ seen at those specific energy levels can be attributed to the interband electronic transitions from the valence to conduction bands. In the high energy (more than 16 eV) region, the imaginary part of the dielectric function approaches zero. Conversely, as the dielectric function's real part approaches unity at high energies, it indicates that the materials become transparent and absorb relatively little high-energy input photons.

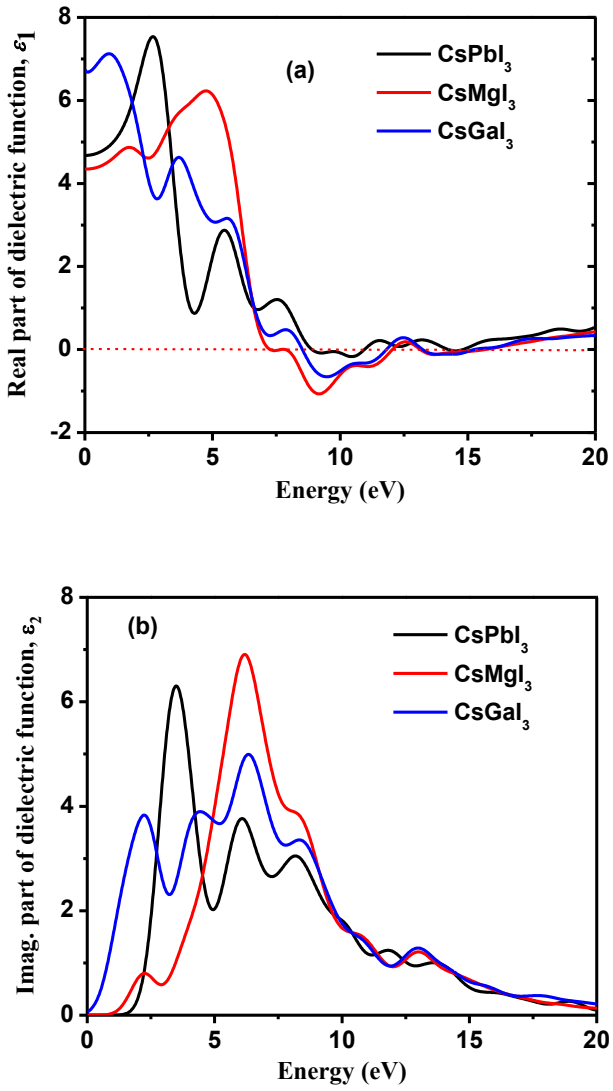

Figure 4.10: Calculated real part (a) and Imaginary part (b) of dielectric function of perovskites $CsMI_3$ (M= Pb, Mg and Ga) respectively.

The plot of the compounds' optical conductivity, σ(ω), is depicted in Fig. 4.11(a), and it closely matches the spectra of $\varepsilon_2(\omega)$ and α(ω). The conductance by the compounds produced during optical stimulation brought on by incident photons of electromagnetic radiation is shown by optical conductivity. For $CsPbI_3$, $CsMgI_3$, and $CsGaI_3$, respectively, the σ(ω) values are also zero until about 1.5 eV, 1.2 eV, and 0 eV, after which they rise to greater levels. It is noted that zero bandgap is obtained for the $CsGaI_3$ compound using PBE potential, whereas it is 1.74 eV using HSE06, all properties are calculated using PBE potential in this study. Therefore, $CsGaI_3$ shows conductivity at 0 eV in Fig. 4.11 (a). Since

zero σ (ω) denotes the lack of optical excitations, it may be explained that there is little interaction between the compound's electrons and photons from the incident EM beam within that photon energy range. In the UV range, it reaches its maximal values for $CsMgI_3$ at 9 eV and for $CsPbI_3$ at 4 eV. In addition to these highest peaks, there are other notable peaks that are limited to the ultraviolet region. The results indicate that the majority of the compounds under consideration exhibit strong conductivity and high absorption in the energy range of 4–16 eV, with a peak seen at around 4 eV. Additionally, it is found that, in comparison to Pb-based compounds, Mg-based compounds yield the highest levels of photoconductivity and photon absorption. It is also evident from the conductivity at zero photon energy that the compounds are semiconducting by nature.

Fig. 4.11 (b) shows the plot of electron energy loss spectra, or EELS [L(ω)]. It explains how an incoming electromagnetic beam might cause a compound's electrons to lose energy. In reality, electronic excitations cause energy loss; the L(ω) spectra provide information on these plasmonic excitations [114]. The UV region, which has the largest peaks for all perovskite compounds, is where the bulk of losses are found, according to the EELS plots.

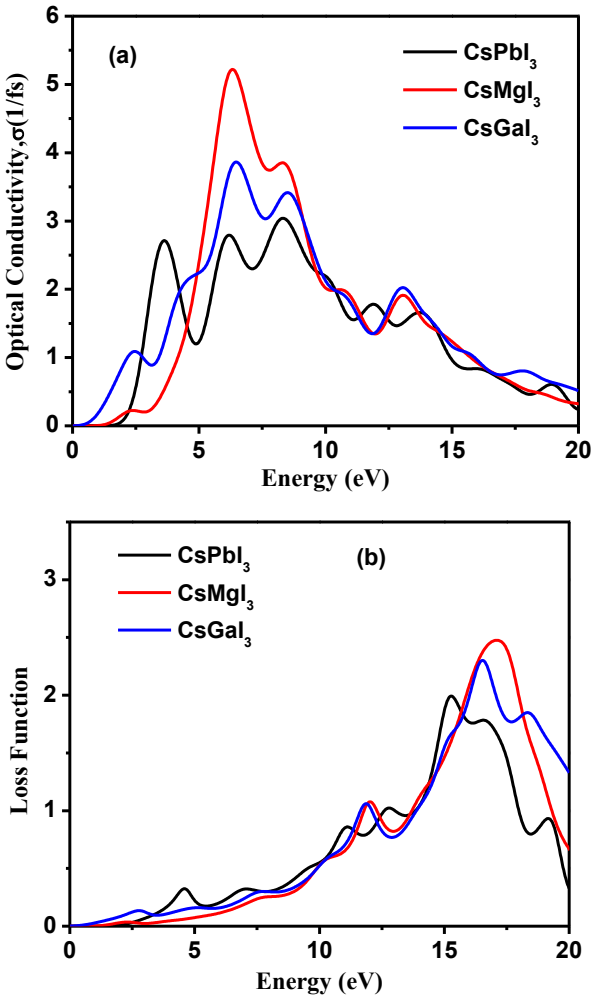

Figure 4.11: Calculated optical conductivity (a) and energy loss function (b) of perovskites $CsMI_3$ (M = Pb, Mg and Ga).

4.6 Thermodynamic Properties

Thermodynamic characteristics, including melting temperature (T_m), Debye temperature (θ_D), minimum thermal conductivity (K_{min}), lattice thermal conductivity (K_{ph}), and Grüneisen parameter (γ), have been examined in order to comprehend the behavior of $CsMI_3$ compounds at high temperatures and pressures. In order to explain several intriguing physical phenomena, including phonons, specific heat, melting temperature, thermal conductivity, etc., θ_D is a crucial characteristic of solids [115]. The following equation [115] may be used to approximate the value of θ_D based on average sound velocity:

$$\Theta_D = \frac{h}{k_B}\left[\frac{3m}{4\pi}\left(\frac{\rho N_A}{M}\right)\right]^{1/3} \nu_m \quad (4.5)$$

where k_B and h denote the Boltzmann and Planck constants, respectively. ρ is the density, and N_A is Avogadro's number. V, m, and M are the volume of a unit cell, the number of atoms within a unit cell, and molecular weight, respectively. v_m implies the average sound velocity in the crystal, which is calculated using the following equation:

$$V_m = \left[\frac{1}{3}\left(\frac{2}{v_t^3} + \frac{1}{v_l^3}\right)\right]^{-1/3} \quad (4.6)$$

Here, v_t and v_l denote the transverse and longitudinal sound velocities, respectively. The following expressions can be used to calculate v_l and v_t using the crystal density, ρ, shear modulus, G, and the bulk modulus, B:

$$\nu_l = \left(\frac{B+34G}{\rho}\right) \quad \text{and} \quad \nu_t = \left[\frac{G}{\rho}\right]^{1/2} \quad (4.7)$$

The melting temperature, T_m, of the $CsMI_3$ compounds has also been calculated via the following empirical formula using elastic constants, C_{ij} [116]**:**

$$T_m = \left[553K + \left(\frac{5.91K}{GPa}\right) C_{11}\right] \pm 300K \quad (4.8)$$

Additionally, thermal conductivity is computed, a crucial quantity that is used to examine a material's ability to transfer heat. It is commonly known that temperature directly affects the minimum thermal conductivity. A material's conductivity steadily increases with temperature and then gradually declines to a limiting value [117]. Although there are other comparable formulas available for predicting the lowest thermal conductivity, the Clarke expression [63] was used in this report's calculation of K_{min}, the minimum thermal conductivity, which has the following definition:

$$K_{min} = k_B \nu_m \left((M/n\rho N_A)^{-2/3}\right. \quad (4.9)$$

Where k_B is the Boltzmann constant, ν_m is the average sound velocity, M is the molecular mass, n is the number of atoms per molecule, and N_A is Avogadro's number.

The lattice thermal conductivity can be used to determine the amount of heat energy transferred by lattice vibrations owing to the temperature gradient in a material (K_{ph}). Slack [118] proposed the following empirical formula to calculate the K_{ph}:

$$K_{ph} = A(\gamma)\frac{M_{av}\Theta_D^3\delta}{\gamma^2 n^{2/3} T} \quad (4.10)$$

With

$$\gamma = \frac{3(1+\upsilon)}{2(2-3\upsilon)} \quad \text{and} \quad A(\gamma) = \frac{4.85628\times10^7}{2\left(1-\frac{0.514}{\gamma}+\frac{0.228}{\gamma^2}\right)} \quad (4.11)$$

The average atomic mass per atom in a compound is denoted by M_{av}, the absolute temperature is denoted by T, the number of atoms in a unit cell is represented by n, and the Grüneisen parameter is represented by γ. A function of γ is A(γ). Table 4.3 displays the values of k_{ph} that are computed at 300 K. A lower value of k_{ph} is obtained because of the smaller Θ_D [119,120]. For the 211 MAX phases, the value of k_{ph} fell between 2.5 (W/mK) and 36 (W/mK). Additionally, Table 4.3 displays the value of the Grüneisen parameter (γ), which indicates the phonons' anharmonicity. Materials with low γ values indicate that harmonic benefaction is present, and as a result, they have high phonon thermal conductivity [86,121]. The crucial parameter for the materials to employ in the high-temperature zone is the minimum thermal conductivity, K_{min}.

The Grüneisen parameter (γ) provides information regarding anharmonic effects, i.e., the temperature-dependent phonon damping as well as the thermal expansion effects. The Grüneisen parameter can be expressed as:

$$\gamma(\omega_n) = \frac{d\ ln(\omega_n)}{d\ (ln(\Phi)\ )} \quad (4.12)$$

where ω_n and Φ are the angular frequency and the packing fraction of crystals, respectively. The calculated values of Debye temperature, θ_D, along with different sound velocities (v_l, v_t, and v_m), melting temperature, T_m, the Grüneisen parameter, γ, and minimum thermal conductivity, K_{min}, lattice thermal conductivity K_{ph} of $CsMI_3$ under study are listed in Table 4.3. In general, a higher Debye temperature is associated with a higher phonon thermal conductivity and vice-versa. The relatively low values of, $K_{min,}$ and K_{ph} of $CsMI_3$ imply low thermal conductivity, and they might be suitable for use as thermoelectric devices.

Table 4.3: The calculated density, ($\boldsymbol{\rho}$), Debye temperature, (Θ_D), longitudinal, transverse, and average sound velocities (V_l, V_t, V_m), minimum thermal conductivity (K_{min}), lattice thermal conductivity (K_{ph}) at 300 K, and melting temperature (T_m) of $CsMI_3$ compound

Compound	**ρ(Kg/m^3)**	**V_l (km/s)**	**V_t (Km/s)**	**V_m (km/s)**	**Θ_D (k)**	**K_{min} (W/m K)**	**K^*_{ph} (W/m K)**	**γ**	**T_m (K)**
$CsPbI_3$	9130	1.78	0.97	1.48	109	0.231	0.844	1.71	787
$CsMgI_3$	8572	2.01	0.04	1.80	143	0.327	1.51	1.59	759
$CsGaI_3$	8905	1.52	0.02	1.06	83	0.181	0.162	2.22	726
$CsCaI_3$	7663	1.92	0.03	1.66	126	0.276	1.13	1.60	754
$CsBaI_3$	6980	1.59	0.81	1.17	81	0.163	0.266	1.90	719
$CsSrI_3$	7371	1.63	0.87	1.31	95	0.2	0.438	1.77	721

4.6.1 Heat Capacities and Thermal Expansion Coefficient

The thermodynamic properties, including heat capacity (C_p, C_V) and thermal expansion coefficient (*TEC*), have been calculated using the results from phonon dispersion and following the quasi-harmonic approximation. These temperature-dependence properties at zero pressure are calculated using the following equations [122]**:**

$$F = 3nN_AK_BT\int_0^{\omega_{max}} \quad ln\left\{2sinh\left(\frac{\hbar\omega}{2K_BT}\right)\right\}g(\omega)d\omega$$

$$E = 3nN_A\frac{\hbar}{2}\int_0^{\omega_{max}} \quad \omega coth\left(\frac{\hbar\omega}{2K_BT}\right)g(\omega)d\omega$$

$$S = 3nN_AK_B\int_0^{\omega_{max}} \quad \left[\frac{\hbar\omega}{2K_BT}coth\left(\frac{\hbar\omega}{2K_BT}\right) - ln\left\{2sinh\left(\frac{\hbar\omega}{2K_BT}\right)\right\}\right]g(\omega)d\omega$$

$$C_v = 9nN_AK_B\left(\frac{T}{\theta_D}\right)\int_0^{x_D} \quad \frac{x^4e^x}{(e^x-1)^2} \qquad (14)$$

Fig. 4.12 (a, b) displays the predicted values of C_p and C_v in the temperature range of 0–1000 K. Materials may be described using their specific heat under a variety of thermodynamic constraints. Heat capacity provides us with important details about the

materials, such as energy band structure, density of state, and lattice vibration. It also describes the material's capacity to retain heat. The concepts of heat capacity at constant pressure (C_p) and heat capacity at constant volume (C_v) are covered here. The phonon contribution dominates C_v and C_p as a function of temperature. The findings show that the specific heat C_v and C_p of $CsMI_3$ match the Debye model [123]. This model provides an accurate prediction of the temperature dependency of the heat capacity at constant volume at low temperatures. $CsMI_3$ exhibits a considerable increase in heat capacity (C_v and C_p) at temperatures as high as 200 K. Furthermore, it has been discovered that elevated temperatures allow for the reinstatement of the Dulong-Petit law. Scientists are interested in disseminating information about the application at high temperatures. By analyzing the thermal characteristics defining factors like Debye temperature (Θ_D), phonon thermal conductivity (k_{ph}), minimum thermal conductivity (K_{min}), Grüneisen parameter (γ), and melting temperature (T_m), one may comprehend the uses of these materials as thermoelectric power generator. The discrepancy between C_p and C_v is due to the thermal expansion of materials, which is brought on by the anharmonicity in the lattice dynamics.

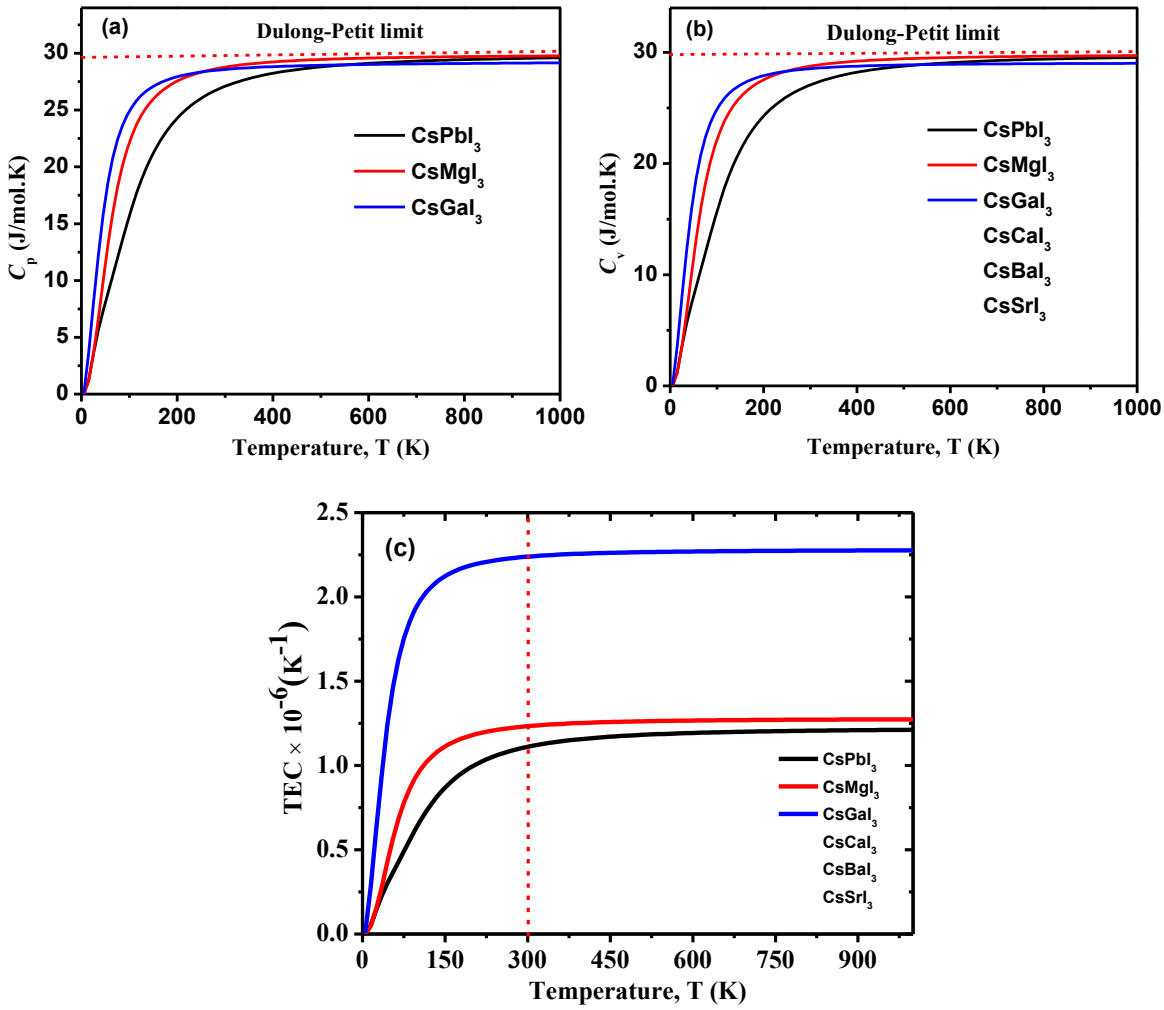

Figure 4.12: Calculated heat capacity at constant pressure, C_p (a) and heat capacity at constant volume, C_v (b), and estimated TEC values (c) of Perovskites $CsMI_3$ (M = Pb, Mg, and Ga) using PBE potential.

The thermal expansion coefficient (*TEC*) is calculated by the following equation [124]:

$$TEC = \frac{\gamma C_v}{3B_T v_m} \qquad (15)$$

Where γ = Grüneisen parameter, C_v = specific heat at constant volume, B_T = isothermal bulk modulus, and v_m = molar volume. The variation of TEC with temperature is presented in Fig. 4.12(c) for the compounds under study. The values are found to be 1.12×10^{-6}, 1.24×10^{-6}, and 2.24×10^{-6} (with unit K^{-1}) at temperature 300 K for the $CsMI_3$ (M = Pb, Mg, and Ga) compounds, respectively. These values are comparable with the reported values for the Ti_2SC

211 MAX phase system [125]. The values of C_p are calculated using $C_p = C_v[1 + \alpha\gamma T]$ and values are found to be26.97, 28.99, and 28.49 (with unit J/mol.K) for the $CsMI_3$ (M = Pb, Mg, and Ga) compounds at temperature 300 K, respectively [121].

4.7 Lead Free Perovskites (Supercell of $CsMg(I_{1-x}Br_x)_3$, x= 0 to 1 in step of 0.25)

It is seen from previous discussion that $CsMgI_3$ shows highest absorption among the candidates of Pb replacement due to environmental hazard and toxicity issues. Then we tried to tune the bandgap of $CsMgI_3$ for more efficient and suitability check in solar cell applications optimized bandgap and secure the Shockley-Queisser criteria. We have performed the solid solution of $CsMgI_3$ (data are represented in appendix Table -1 and Appendix Fig. 1 and Fig. 2), but optical properties could not get from solid solution, then we have formed supercell and calculated the optical properties, the following section we will present the supercell properties of $CsMgI_3$.

The key characteristics of the studied perovskite materials are illustrated in Table 4.4. It is seen that $CsMgI_3$ has higher absorption coefficient compared to others and it is suitable for optical device application.

Table 4.4: The key properties are summarized to predict perovskites.

Traits	**$CsPbI_3$**	**$CsMgI_3$**	**$CsGaI_3$**
Optical Absorption	Less	High	High
Photoconductivity	Less	High	Medium
Ductility	Highly Ductile	Brittle- Ductile Border line	Highly Ductile
Dynamically stable	Yes	Yes	Yes
Band Gap (eV) (using PBE-potential)	1.48	1.12	0
Reflectivity	High	High	Medium
Formation Energy	Negative	Negative	Negative

Table 4.4 summarizes the essential characteristics of the metal halide perovskites $CsMI_3$. As can be seen in Fig. 4.9 (a), the $CsGaI_3$ displays high absorbance; yet, using the PBE potential, it is proven that E_g= 0 eV. Since the $CsGaI_3$ exhibits metal properties, it might not be a good choice for solar applications. It should be mentioned that $CsGaI_3$ shows a non-zero bandgap when utilizing the HSE06 potential, but a 0 eV bandgap when using PBE. PBE potential was employed in this investigation to examine every compound's characteristic. Consequently, further insight into the $CsGaI_3$ characteristics may be gained. Then, the Mg-based compounds, in contrast to Pb-containing compounds, exhibit high optical absorbance and optical conductivity, indicating that Mg might be a more suitable substitute for lead. Furthermore, because $CsMgI_3$ has the maximum absorption and photoconductivity in the solar spectrum, It may be assumed that it would be a superior lead-free perovskite material for solar cell application. However, the issue with $CsMgI_3$ is that it remains at the boundary between brittleness and ductility. However, brittleness can be reduced by combining Br and Cl with $CsMgI_3$ in a solid solution [126]. This will increase the likelihood of obtaining a more lead-free, magnesium-based perovskite compound with a better band gap and better optoelectronic characteristics for use in solar cells. The mechanical characteristics and electronic band gap of solid solutions $CsMg(I_{1-x}Br_x)_3$ have been computed in order to identify a ductile lead-free perovskite. Fig. 4.13 shows the Pugh's ratio with Poisson's ratio for various combinations of I and Br. The results show that in $CsMg(I_{1-x}Br_x)_3$, the highest ductility is located at x = 0.25. The results indicate that $CsMg(I_{0.75}Br_{0.25})_3$ is more ductile than $CsMgI_3$. Additionally, the material is soft and mechanically stable (Appendix Table-2), and it can be readily fabricated as a thin film. A supercell of $CsMg(I_{1-x}Br_x)_3$ is produced where x = 0, 0.25, 0.50, 0.75, and 1 in order to better understand absorption and optical conductivity. The electronic band gap of $CsMg(I_{0.75}Br_{0.25})_3$ is determined to be 1.4 eV. For applications that need ductility, the optimum Pb-free perovskite would be $CsMg(I_{0.75}Br_{0.25})_3$. The electronic band gap value is graphically presented with the lattice parameter in appendix Fig. 1 (a,b), indicating that $CsMg(I_{1-x}Br_x)_3$ is a superior combination.

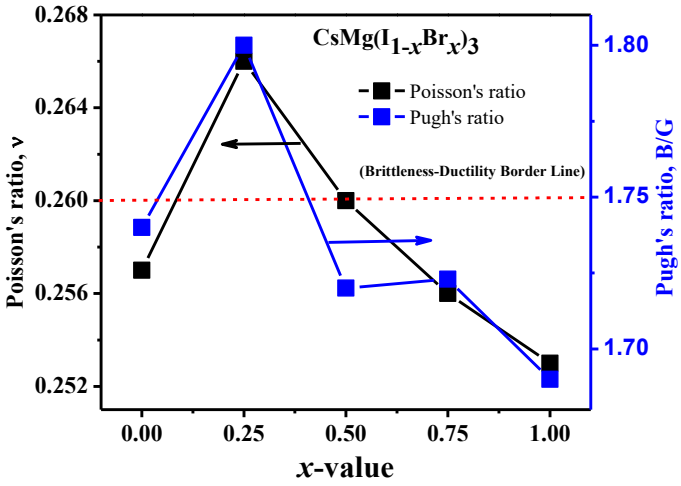

Figure 4.13: Variation of Pugh's ratio with Poisson's ratio of the perovskites with different compositions in supercell of $CsMg(I_{1-x}Br_x)_3$. The red dashed line separates the ductile materials from the brittle.

4.7.1 Opto-electronic of lead-free perovskites (supercell of $CsMg(I_{1-x}Br_x)_3$, x = 0, 0.25, 0.50, 0.75, 1):

Despite having acceptable mechanical stability and ductility qualities, the $CsMg(I_{0.6}Br_{0.4})_3$ solid solution does not exhibit the optical properties necessary to get a desired band gap value of 1-1.8 eV for use in solar cell applications. To get a deeper knowledge of the electronic band gap and more suitable optoelectronic characteristics, a supercell of 40 $CsMg(I_{1-x}Br_x)_3$ atoms, with x = 0, 0.25, 0.50, 0.75 has been constructed and 1; the structural property section has already covered x-values. 24 I atoms in the $CsMgI_3$ supercell have undergone successive changes to produce the desired mixture of 25%, 50%, 75%, and 100% Br in the molecule. Fig.4.14 displays the electronic band gap of the supercell $CsMg(I_{1-x}Br_x)_3$, with x = (0, 0.25, 0.50, 0.75, and 1).

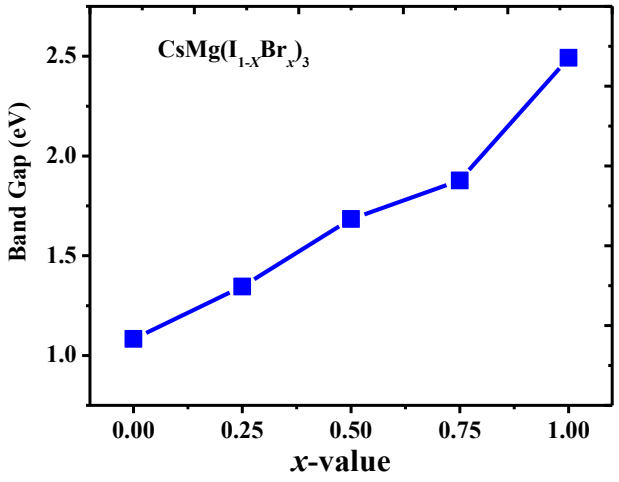

Figure 4.14: Variations of band gap of the perovskites with different composition [$CsMg(I_{1-x}Br_x)_3$ supercell].

According to the findings (Appendix Table-1), the $CsMg(I_{0.75}Br_{0.25})_3$ compound is more ductile than the $CsMgI_3$ material. It is also soft and mechanically stable, making it easy to form into thin films. Appendix Table 2 indicates that these composite compounds exhibit a modest phase change from cubic to triclinic, as well as 21 positive stiffness constants that all fulfill stability requirements. It is discovered that CsMg $(I_{0.75}Br_{0.25})_3$ has a band gap of 1.35 eV and favorable optical characteristics, indicating that it is a favorable candidate for lead-free perovskite. However, the $CsMg(I_{1-x}Br_x)_3$ compound exhibits an expected band gap of 1.87 eV for x = 0.50 and 0.75. However, the Shockley-Queisser limit indicates that a reasonable band gap for a single solar cell is 1.4.

For considered lead-free perovskite compounds $CsMg(I_{1-x}Br_x)_3$, where x = 0, 0.25, 0.75, 0.50, 1, the detailed optical properties, including the real and imaginary parts of dielectric functions, refractive index, extinction coefficient, absorption spectra, reflectivity, and photoconductivity, are investigated up to the photon energy of 20 eV to reveal the response of the materials in solar and high energy radiation [Appendix Fig. 2 (a-e)]. The amount of light at a given wavelength (energy) that enters a material before it is absorbed is measured by the substance's optical absorption coefficient [125]. Additionally, it provides details on the ideal solar energy conversion efficiency, which is crucial for a material's actual use in solar cells. Fig. 15 (a) shows the computed optical absorption spectra of the compounds

under consideration for the visible range. Its values are nearly identical to the bare $CsMgI_3$, and it varies greatly in the visible range.

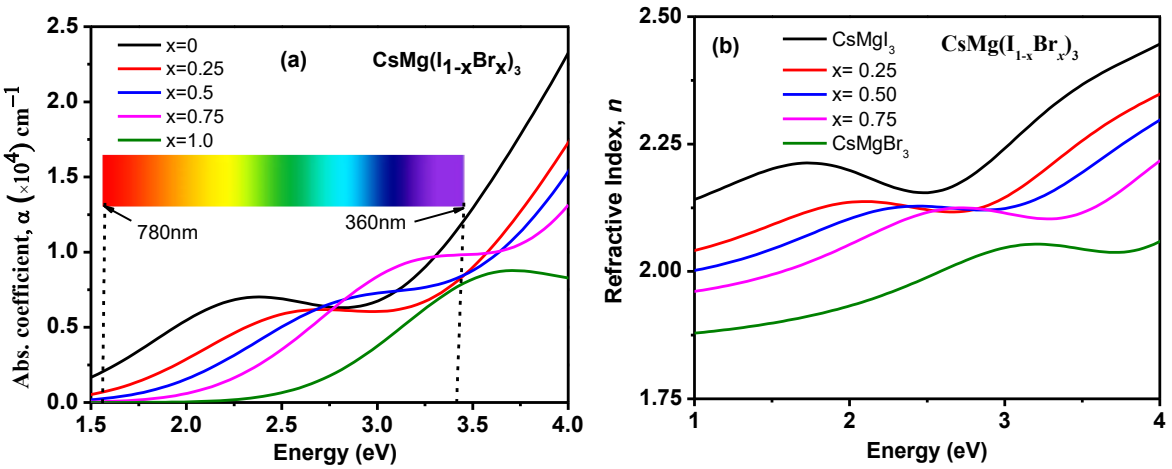

Figure 4.15: (a) Variations of absorption coefficient as a function of photon energy (b) refractive index for different compositions of $CsMg(I_{1-x}Br_x)3$ supercell.

The calculated refractive index, n, is shown in Fig. 4.15 (b), where n can be varied from 2.10 – 2.24 in the range of visible range for $x = 0.25$. It is consistent with its bare $CsMgI_3$ compound that is comparable with its commercially available counterpart (Fig. 4.9c). The remaining optical properties of the supercell, i.e., dialectic constant, conductivity, and loss function, have been represented in the supplementary section. All these findings reveal that $CsMg(I_{0.75}Br_{0.25})$ is a better replacement for lead-free perovskite for solar cell applications.

Chapter 5: CONCLUSIONS

5.1 General

This chapter summarizes the results and main conclusions obtained from a large-scale research study on perovskite $CsMI_3$ compounds' properties. The investigation probed structural, elastic, electronic and optical thermal elements to reveal the complexity uncovered in these materials as well as their promising uses.

5.2 Key Findings

First principles We have studied the structural, electronic, optical, mechanical, and thermodynamic characteristics of the Pb-free inorganic metal halide cubic perovskites $CsMI_3$ (M = Mg and Ga) using DFT simulations. We have contrasted these substances with lead-based compounds. The compounds demonstrated their chemical and structural stability through the negative formation energy, all positive frequencies in the phonon dispersion curve, and the fulfilment of stability criteria by elastic constants. From this study, it seems that switching the M= (Mg and Ga) atoms in the $CsMI_3$ compound for Pb atoms might change the electronic band gap value and other building blocks. These are the primary features of the materials intended for use in optoelectronic devices and solar cells. The examined perovskite compounds have a low bulk modulus, which makes them easily produced into thin films and mechanically stable. The Mg atom appears to be preferable to Pb for the inorganic perovskites under consideration, based on the investigation of both optical and electronic characteristics, as Mg-based compounds, such as $CsMgI_3$, exhibit better optical absorption and optical conductivity than Pb-based compounds. Replacing I with Br in $CsMgI_3$ significantly improves the photovoltaic characteristics, increasing the band gap from 1.12 to 1.87 eV and the absorption coefficient. The increase in E_g and γ caused by doping into CsMg ($I_{0.75}Br_{0.25}$) makes them suitable for use in solar cell materials. Based on the Shockley-Queisser limit, the optimal combination, $CsMg(I_{0.75}Br_{0.25})_3$, has an E_g of 1.4 eV, making it the ideal band gap for the maximum efficiency of a single solar cell.

5.3 Limitation of the Study

Although this work gives an insight into the physical properties of $CsMI_3$(M = Pb, Mg and Ga) compounds, it is very necessary to note its shortcomings. Although the study mainly deals with theoretical calculations, experiments should be done to ensure that those results obtained are real and applicable in nature.

5.4 Recommendation for Further Study

To continue the improvement in our knowledge and use of compounds $CsMI_3$, some really good options for further investigations are available. In the light of optoelectronic and thermal behaviors, experimental studies that could validate such theoretical findings will help to make a lot sense. Moreover, the research into the modification of these compounds through techniques such as alloying and also doping could lead to new materials with superior performance. The use of the two applications, photovoltaic and thermal barrier in practical tests will also help to determine their strengths for different industries.

In this research, we have summarized the intricate nature of perovskite $CsMI_3$ compounds to provide a way forward for their practical utilization in the various areas. The research findings hold great potential for benefiting the fields of material science, electronics, and sustainable energy. Our investigation strongly recommends conducting experimental synthesis to further enhance understanding and applications in these domains.

5.5 Impact of the present research

The current DFT-based investigation on $CsMI_3$ (M = Pb, Mg and Ga) perovskite semiconductors have a great importance in the numerous technological fields. The calculated band gaps for $CsPbI_3$, $CsMgI_3$ and $CsGaI_3$ are 1.48 eV, 1.12 eV, and 1.74 eV respectively. It is worth noting that the spectrally distributed band gaps lie within the visible and near-IR, providing the possibility of sunlight absorption over IR, visible, and even some UV wavelengths which is one of the most remarkable results. The value of absorption coefficient ($\sim 10^5$ cm^{-1}) of the studied compounds is almost comparable with that of the commercialized compound. This knowledge establishes an important starting point for the possible use of $CsMgI_3$ compounds in high-tech applications, mainly in optoelectronics, solar energy

conversion, and material engineering. The beneficial thermodynamics properties and low lattice thermal conductivity in $CsMgI_3$ makes it a potential form for the applications in thermal barrier coatings (TBC).

Appendices

Appendix Table-1: The calculated elastic constants C_{ij} (GPa), bulk modulus B (GPa), shear modulus G (GPa), Young's modulus Y (GPa), Pugh's ratio (B/G) and Poisson's ratio v of perovskites solid solutions $CsMg(I_{1-x}Br_x)_3$.

Phase	C_{11}	C_{12}	C_{44}	B	G	Y	B/G	v
$CsMgI_3$	34.81	12.08	11.09	19.65	11.20	28.24	1.754	0.261
$CsMg(I_{0.9}Br_{0.1})_3$	33.86	11.70	11.35	19.09	11.24	28.19	1.70	0.254
$CsMg(I_{0.8}Br_{0.2})_3$	32.91	12.35	11.75	19.20	11.14	28.00	1.724	0.260
$CsMg(I_{0.7}Br_{0.3})_3$	35.58	13.33	12.56	20.75	11.97	30.11	1.734	0.260
$CsMg(I_{0.6}Br_{0.4})_3$	46.93	16.55	15.13	26.67	15.15	38.22	1.76	0.261
$CsMg(I_{0.5}Br_{0.5})_3$	36.73	13.66	13.27	21.35	12.54	31.47	1.70	0.254
$CsMg(I_{0.4}Br_{0.6})_3$	38.15	13.70	13.87	21.85	13.19	32.94	1.66	0.250
$CsMg(I_{0.3}Br_{0.7})_3$	39.22	14.55	14.16	22.77	13.40	33.61	1.70	0.254
$CsMg(I_{0.2}Br_{0.8})_3$	39.73	14.20	14.43	22.71	13.74	34.30	1.65	0.250
$CsMg(I_{0.1}Br_{0.9})_3$	41.45	15.33	14.70	24.038	14.023	35.24	1.71	0.256
$CsMgBr_3$	42.59	15.55	15.20	24.56	14.50	36.95	1.69	0.253

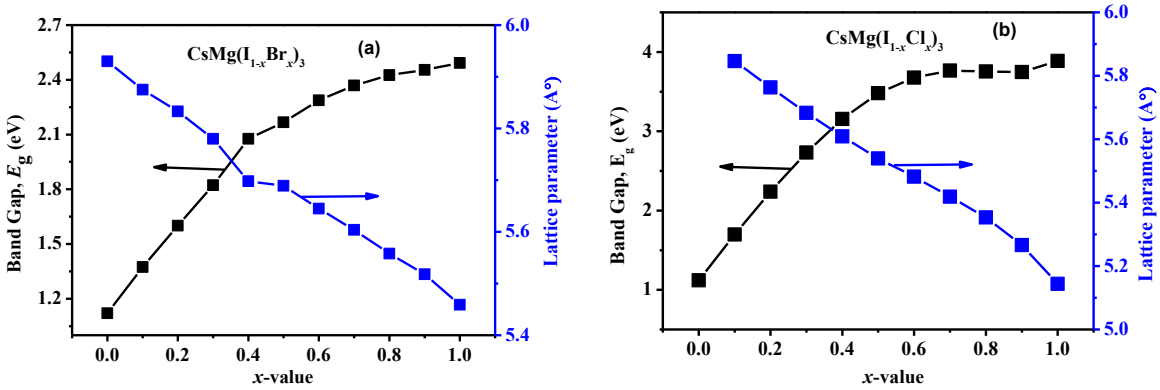

Appendix Fig. 1: Variations of band gap values with different lattice parameters for different compositions of perovskites [solid solutions of $CsMg(I_{1-x}Br_x)_3$ and $CsMg(I_{1-x}Cl_x)_3$].

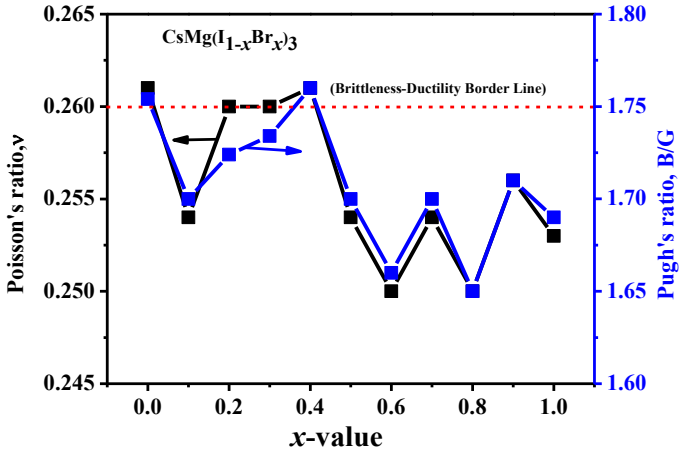

Appendix Fig.2: Variations of Pugh ratio and Poisson ratio of solid solution $CsMg(I_{1-x}Br_x)_3$.

Appendix Table 2: The calculated elastic constants C_{ij} (GPa), machinability indices (B/C_{44}) and Cauchy pressures [(C_{12} - C_{44})] (GPa) of supercell $CsMg(I_{1-x}Br_x)_3$ perovskite compounds.

Parameters	**$CsMg(I_{1-x}Br_x)_3$ x=0**	**$CsMg(I_{1-x}Br_x)_3$ x =0.25**	**$CsMg(I_{1-x}Br_x)_3$ x =0.50**	**$CsMg(I_{1-}Br_x)_3$ x =0.75**	**$CsMg(I_{1-x}Br_x)_3$ x =1.00**
C_{11}	31.990	34.595	37.386	40.239	43.921
C_{22}	32.148	35.689	37.464	41.235	43.670
C_{33}	32.163	35.651	37.393	20.844	43.920
C_{44}	10.350	11.759	13.444	13.183	15.731
C_{55}	10.351	13.925	13.441	13.028	15.743
C_{66}	10.352	9.730	13.426	12.818	15.765
C_{12}	11.071	13.767	14.110	15.760	16.083
C_{13}	11.074	13.412	14.124	18.088	16.170
C_{14}	0.027	0.223	0.025	0.255	0.078
C_{15}	0.037	0.196	0.023	0.588	0.050
C_{16}	0.055	0.621	0.015	0.052	0.389
C_{23}	11.150	12.396	14.123	10.450	16.084
C_{24}	0.032	0.080	0.023	0.198	0.080
C_{25}	0.039	0.116	0.028	0.231	0.050
C_{26}	0.057	0.635	0.005	0.075	0.452
C_{34}	0.032	0.085	0.027	0.117	0.077
C_{35}	0.033	0.065	0.025	0.414	0.049
C_{36}	0.057	0.394	0.018	2.844	0.464
C_{45}	0.001	0.003	0.001	0.278	0.003
C_{46}	0.000	0.036	0.000	0.107	0.059
C_{56}	0.002	0.219	0.002	0.048	0.005
B/C_{44}	1.75	1.74	1.63	1.22	1.61
(C_{12}-C_{44})	0.721	2.008	0.666	2.577	0.352

Optical properties of supercell of $CsMg(I_{1-x}Br_x)_3$:

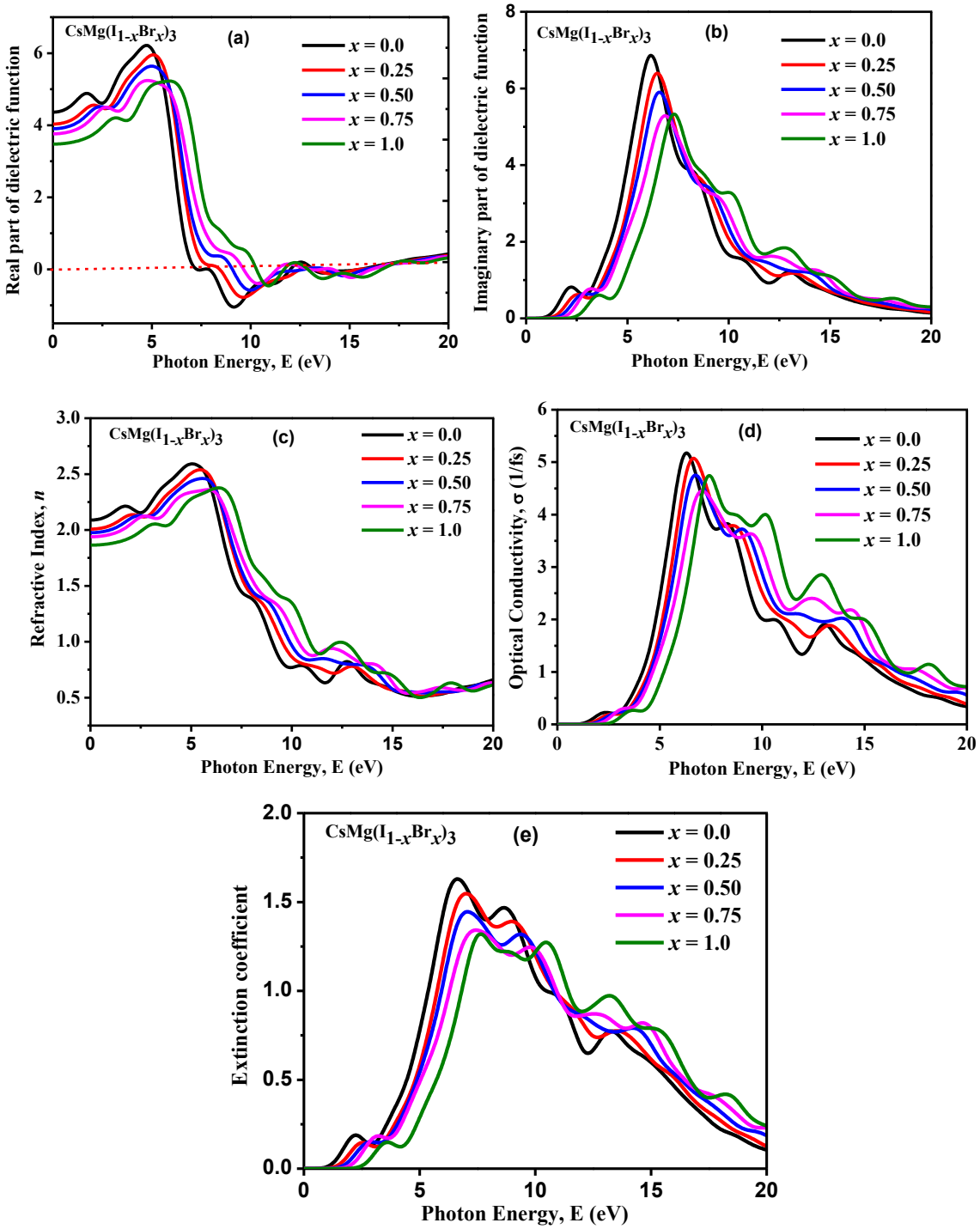

Appendix Fig. 3(a-e): Variation of real (a) and imaginary (b) part of dielectric function, refractive index (c), photoconductivity (d) and extinction coefficient (e) of the supercell $CsMg(I_{1-x}Br_x)_3$ perovskites.

References:

[1] Q.A. Akkerman, M. Gandini, F. Di Stasio, P. Rastogi, F. Palazon, G. Bertoni, J.M. Ball, M. Prato, A. Petrozza, L. Manna, Strongly emissive perovskite nanocrystal inks for high-voltage solar cells, Nature Energy. 2 (2016) 16194. https://doi.org/10.1038/nenergy.2016.194.

[2] Z. Ni, H. Jiao, C. Fei, H. Gu, S. Xu, Z. Yu, G. Yang, Y. Deng, Q. Jiang, Y. Liu, Y. Yan, J. Huang, Evolution of defects during the degradation of metal halide perovskite solar cells under reverse bias and illumination, Nature Energy. 7 (2022) 65–73. https://doi.org/10.1038/s41560-021-00949-9.

[3] W. Zhang, G.E. Eperon, H.J. Snaith, Metal halide perovskites for energy applications, Nature Energy. 1 (2016). https://doi.org/10.1038/nenergy.2016.48.

[4] P. Ramasamy, D.H. Lim, B. Kim, S.H. Lee, M.S. Lee, J.S. Lee, All-inorganic cesium lead halide perovskite nanocrystals for photodetector applications, Chemical Communications. 52 (2016) 2067–2070. https://doi.org/10.1039/c5cc08643d.

[5] A. Swarnkar, A.R. Marshall, E.M. Sanehira, B.D. Chernomordik, D.T. Moore, J.A. Christians, T. Chakrabarti, J.M. Luther, Quantum dot–induced phase stabilization of α-$CsPbI_3$ perovskite for high-efficiency photovoltaics, Science. 354 (2016) 92–95. https://doi.org/10.1126/science.aag2700.

[6] W.J. Yin, T. Shi, Y. Yan, Unique properties of halide perovskites as possible origins of the superior solar cell performance, Advanced Materials. 26 (2014) 4653–4658. https://doi.org/10.1002/adma.201306281.

[7] K.P. Marshall, M. Walker, R.I. Walton, R.A. Hatton, Enhanced stability and efficiency in hole-transport-layer-free $CsSnI_3$ perovskite photovoltaics, Nature Energy. 1 (2016) 16178. https://doi.org/10.1038/nenergy.2016.178.

[8] R.J. Sutton, G.E. Eperon, L. Miranda, E.S. Parrott, B.A. Kamino, J.B. Patel, M.T. Hörantner, M.B. Johnston, A.A. Haghighirad, D.T. Moore, H.J. Snaith, Bandgap-Tunable Cesium Lead Halide Perovskites with High Thermal Stability for Efficient Solar Cells, Advanced Energy Materials. 6 (2016) 1502458. https://doi.org/https://doi.org/10.1002/aenm.201502458.

[9] J.B. Hoffman, A.L. Schleper, P. V Kamat, Transformation of Sintered CsPbBr3 Nanocrystals to Cubic $CsPbI_3$ and Gradient $CsPbBr_xI_{3-x}$ through Halide Exchange., Journal of the American Chemical Society. 138 (2016) 8603–8611. https://doi.org/10.1021/jacs.6b04661.

[10] L. Huang, W.R.L. Lambrecht, Electronic band structure trends of perovskite halides: Beyond Pb and Sn to Ge and Si, Phys. Rev. B. 93 (2016) 195211. https://doi.org/10.1103/PhysRevB.93.195211.

[11] G.E. Eperon, G.M. Paternò, R.J. Sutton, A. Zampetti, A.A. Haghighirad, F. Cacialli, H.J. Snaith, Inorganic caesium lead iodide perovskite solar cells, J. Mater. Chem. A. 3 (2015) 19688–19695. https://doi.org/10.1039/C5TA06398A.

[12] T. Krishnamoorthy, H. Ding, C. Yan, W.L. Leong, T. Baikie, Z. Zhang, M. Sherburne, S. Li, M. Asta, N. Mathews, S.G. Mhaisalkar, Lead-free germanium iodide perovskite materials for photovoltaic applications, Journal of Materials Chemistry A. 3 (2015) 23829–23832. https://doi.org/10.1039/c5ta05741h.

[13] Best research-cell efciency chart. NREL, (n.d.). https://www.nrel.gov/pv/cellefciency.html (2021).

[14] M.M. Lee, J. Teuscher, T. Miyasaka, T.N. Murakami, H.J. Snaith, Efficient Hybrid Solar Cells Based on Meso-Superstructured Organometal Halide Perovskites, Science. 338 (2012) 643–647. https://doi.org/10.1126/science.1228604.

[15] D.P. McMeekin, G. Sadoughi, W. Rehman, G.E. Eperon, M. Saliba, M.T. Hörantner, A. Haghighirad, N. Sakai, L. Korte, B. Rech, M.B. Johnston, L.M. Herz, H.J. Snaith, A mixed-cation lead mixed-halide perovskite absorber for tandem solar cells, Science. 351 (2016) 151–155. https://doi.org/10.1126/science.aad5845.

[16] S. Yang, S. Chen, E. Mosconi, Y. Fang, X. Xiao, C. Wang, Y. Zhou, Z. Yu, J. Zhao, Y. Gao, F. De Angelis, J. Huang, Stabilizing halide perovskite surfaces for solar cell operation with wide-bandgap lead oxysalts, Science. 365 (2019) 473–478. https://doi.org/10.1126/science.aax3294.

[17] Y.-H. Lin, N. Sakai, P. Da, J. Wu, H.C. Sansom, A.J. Ramadan, S. Mahesh, J. Liu, R.D.J. Oliver, J. Lim, L. Aspitarte, K. Sharma, P.K. Madhu, A.B. Morales-Vilches,

P.K. Nayak, S. Bai, F. Gao, C.R.M. Grovenor, M.B. Johnston, J.G. Labram, J.R. Durrant, J.M. Ball, B. Wenger, B. Stannowski, H.J. Snaith, A piperidinium salt stabilizes efficient metal-halide perovskite solar cells, Science. 369 (2020) 96–102. https://doi.org/10.1126/science.aba1628.

[18] W.S. Yang, B.W. Park, E.H. Jung, N.J. Jeon, Y.C. Kim, D.U. Lee, S.S. Shin, J. Seo, E.K. Kim, J.H. Noh, S. Il Seok, Iodide management in formamidinium-lead-halide-based perovskite layers for efficient solar cells, Science. 356 (2017) 1376–1379. https://doi.org/10.1126/science.aan2301.

[19] T. Baikie, Y. Fang, J.M. Kadro, M. Schreyer, F. Wei, S.G. Mhaisalkar, M. Graetzel, T.J. White, Synthesis and crystal chemistry of the hybrid perovskite (CH_3NH_3)PbI3 for solid-state sensitised solar cell applications, Journal of Materials Chemistry A. 1 (2013) 5628–5641. https://doi.org/10.1039/c3ta10518k.

[20] M.R. Filip, F. Giustino, GW quasiparticle band gap of the hybrid organic-inorganic perovskite $CH_3NH_3PbI_3$: Effect of spin-orbit interaction, semicore electrons, and self-consistency, Physical Review B - Condensed Matter and Materials Physics. 90 (2014) 1–10. https://doi.org/10.1103/PhysRevB.90.245145.

[21] D. Shi, V. Adinolfi, R. Comin, M. Yuan, E. Alarousu, A. Buin, Y. Chen, S. Hoogland, A. Rothenberger, K. Katsiev, Y. Losovyj, X. Zhang, P.A. Dowben, O.F. Mohammed, E.H. Sargent, O.M. Bakr, Low trap-state density and long carrier diffusion in organolead trihalide perovskite single crystals, Science. 347 (2015) 519–522. https://doi.org/10.1126/science.aaa2725.

[22] K. Tvingstedt, O. Malinkiewicz, A. Baumann, C. Deibel, H.J. Snaith, V. Dyakonov, H.J. Bolink, Radiative efficiency of lead iodide based perovskite solar cells, Scientific Reports. 4 (2014) 1–7. https://doi.org/10.1038/srep06071.

[23] G. Xing, N. Mathews, S. Sun, S.S. Lim, Y.M. Lam, M. Grätzel, S. Mhaisalkar, T.C. Sum, Long-Range Balanced Electron- and Hole-Transport Lengths in Organic-Inorganic $CH_3NH_3PbI_3$, Science. 342 (2013) 344–347. https://doi.org/10.1126/science.1243167.

[24] S.D. Stranks, G.E. Eperon, G. Grancini, C. Menelaou, M.J.P. Alcocer, T. Leijtens,

L.M. Herz, A. Petrozza, H.J. Snaith, Electron-hole diffusion lengths exceeding 1 micrometer in an organometal trihalide perovskite absorber, Science. 342 (2013) 341–344. https://doi.org/10.1126/science.1243982.

[25] M. Grätzel, The light and shade of perovskite solar cells, Nature Materials. 13 (2014) 838–842. https://doi.org/10.1038/nmat4065.

[26] C. Wehrenfennig, G.E. Eperon, M.B. Johnston, H.J. Snaith, L.M. Herz, High Charge Carrier Mobilities and Lifetimes in Organolead Trihalide Perovskites, Advanced Materials. 26 (2014) 1584–1589. https://doi.org/10.1002/adma.201305172.

[27] C.C. Stoumpos, C.D. Malliakas, M.G. Kanatzidis, Semiconducting Tin and Lead Iodide Perovskites with Organic Cations: Phase Transitions, High Mobilities, and Near-Infrared Photoluminescent Properties, Inorganic Chemistry. 52 (2013) 9019–9038. https://doi.org/10.1021/ic401215x.

[28] A. Babayigit, D. Duy Thanh, A. Ethirajan, J. Manca, M. Muller, H.G. Boyen, B. Conings, Assessing the toxicity of Pb-and Sn-based perovskite solar cells in model organism Danio rerio, Scientific Reports. 6 (2016) 1–11. https://doi.org/10.1038/srep18721.

[29] F. Giustino, H.J. Snaith, Toward Lead-Free Perovskite Solar Cells, ACS Energy Letters. 1 (2016) 1233–1240. https://doi.org/10.1021/acsenergylett.6b00499.

[30] B. Hailegnaw, S. Kirmayer, E. Edri, G. Hodes, D. Cahen, Rain on methylammonium lead iodide based perovskites: Possible environmental effects of perovskite solar cells, Journal of Physical Chemistry Letters. 6 (2015) 1543–1547. https://doi.org/10.1021/acs.jpclett.5b00504.

[31] R. Wang, J. Wang, S. Tan, Y. Duan, Z.-K. Wang, Y. Yang, Opportunities and Challenges of Lead-Free Perovskite Optoelectronic Devices, Trends in Chemistry. 1 (2019) 368–379. https://doi.org/10.1016/j.trechm.2019.04.004.

[32] F. Hong, B. Saparov, W. Meng, Z. Xiao, D.B. Mitzi, Y. Yan, Viability of Lead-Free Perovskites with Mixed Chalcogen and Halogen Anions for Photovoltaic Applications, Journal of Physical Chemistry C. 120 (2016) 6435–6441. https://doi.org/10.1021/acs.jpcc.6b00920.

[33] M. Lyu, J.H. Yun, P. Chen, M. Hao, L. Wang, Addressing Toxicity of Lead: Progress and Applications of Low-Toxic Metal Halide Perovskites and Their Derivatives, Advanced Energy Materials. 7 (2017). https://doi.org/10.1002/aenm.201602512.

[34] Z. Shi, J. Guo, Y. Chen, Q. Li, Y. Pan, H. Zhang, Y. Xia, W. Huang, Lead-Free Organic–Inorganic Hybrid Perovskites for Photovoltaic Applications: Recent Advances and Perspectives, Advanced Materials. 29 (2017). https://doi.org/10.1002/adma.201605005.

[35] M. Roknuzzaman, K. Ostrikov, H. Wang, A. Du, T. Tesfamichael, Towards lead-free perovskite photovoltaics and optoelectronics by ab-initio simulations, Scientific Reports. 7 (2017) 14025. https://doi.org/10.1038/s41598-017-13172-y.

[36] G.E. Eperon, S.D. Stranks, C. Menelaou, M.B. Johnston, L.M. Herz, H.J. Snaith, Formamidinium lead trihalide: A broadly tunable perovskite for efficient planar heterojunction solar cells, Energy and Environmental Science. 7 (2014) 982–988. https://doi.org/10.1039/c3ee43822h.

[37] B. Ghosh, S. Chakraborty, H. Wei, C. Guet, S. Li, S. Mhaisalkar, N. Mathews, Poor Photovoltaic Performance of $Cs_3Bi_2I_9$: An Insight through First-Principles Calculations, Journal of Physical Chemistry C. 121 (2017) 17062–17067. https://doi.org/10.1021/acs.jpcc.7b03501.

[38] N.H. Tiep, Z. Ku, H.J. Fan, Recent Advances in Improving the Stability of Perovskite Solar Cells, Advanced Energy Materials. 6 (2016) 1–19. https://doi.org/10.1002/aenm.201501420.

[39] J. Zhao, H. Liu, Z. Yu, R. Quhe, S. Zhou, Y. Wang, C.C. Liu, H. Zhong, N. Han, J. Lu, Y. Yao, K. Wu, Rise of silicene: A competitive 2D material, Progress in Materials Science. 83 (2016). https://doi.org/10.1016/j.pmatsci.2016.04.001.

[40] B. Saparov, F. Hong, J.-P. Sun, H.-S. Duan, W. Meng, S. Cameron, I.G. Hill, Y. Yan, D.B. Mitzi, Thin-Film Preparation and Characterization of $Cs_3Sb_2I_9$: A Lead-Free Layered Perovskite Semiconductor, Chemistry of Materials. 27 (2015) 5622–5632. https://doi.org/10.1021/acs.chemmater.5b01989.

[41] M. Serhan, M. Sprowls, D. Jackemeyer, M. Long, I.D. Perez, W. Maret, N. Tao, E.

Forzani, Total iron measurement in human serum with a smartphone, AIChE Annual Meeting, Conference Proceedings. 2019-Novem (2019) 1–3. https://doi.org/10.1039/x0xx00000x.

[42] M.R. Filip, F. Giustino, Computational Screening of Homovalent Lead Substitution in Organic-Inorganic Halide Perovskites, Journal of Physical Chemistry C. 120 (2016) 166–173. https://doi.org/10.1021/acs.jpcc.5b11845.

[43] D. Ray, C. Clark, H.Q. Pham, J. Borycz, R.J. Holmes, E.S. Aydil, L. Gagliardi, Computational Study of Structural and Electronic Properties of Lead-Free $CsMI_3$ Perovskites (M = Ge, Sn, Pb, Mg, Ca, Sr, and Ba), Journal of Physical Chemistry C. 122 (2018) 7838–7848. https://doi.org/10.1021/acs.jpcc.8b00226.

[44] M.R. Filip, G.E. Eperon, H.J. Snaith, F. Giustino, Steric engineering of metal-halide perovskites with tunable optical band gaps, Nature Communications. 5 (2014) 5757. https://doi.org/10.1038/ncomms6757.

[45] J.A. Warner, S.K.R. Patil, S. V Khare, K.C. Masiulaniec, Ab initio calculations for properties of MAX phases Ti_2TlC, Zr_2TlC, and Hf_2TlC, Applied Physics Letters. 88 (2006) 101911.

[46] D. YL, S. ZM, H. Hashimoto, T. WB, First-principles study on thermodynamic properties of Ti_2AlC and Ti_2SC, Materials Transactions. 50 (2009) 2173–2176.

[47] Z. Ni, H. Jiao, C. Fei, H. Gu, S. Xu, Z. Yu, G. Yang, Y. Deng, Q. Jiang, Y. Liu, Y. Yan, J. Huang, Evolution of defects during the degradation of metal halide perovskite solar cells under reverse bias and illumination, Nature Energy. 7 (2021) 65–73. https://doi.org/10.1038/s41560-021-00949-9.

[48] A. Swarnkar, A.R. Marshall, E.M. Sanehira, B.D. Chernomordik, D.T. Moore, J.A. Christians, T. Chakrabarti, J.M. Luther, Quantum dot–induced phase stabilization of α-$CsPbI_3$ perovskite for high-efficiency photovoltaics, Science. 354 (2016) 92–95. https://doi.org/10.1126/science.aag2700.

[49] A. Kojima, K. Teshima, Y. Shirai, T. Miyasaka, Organometal Halide Perovskites as Visible-Light Sensitizers for Photovoltaic Cells, Journal of the American Chemical Society. 131 (2009) 6050–6051. https://doi.org/10.1021/ja809598r.

[50] M.R. Filip, F. Giustino, "Quasiparticle band gap of the hybrid organic-inorganic perovskite Effect of spin-orbit interaction, semicore electrons, and self-consistency", Physical Review B. 90 (2014) 245145. https://doi.org/10.1103/PhysRevB.90.245145.

[51] B. Peng, H. Zhang, H. Shao, Z. Ning, Y. Xu, G. Ni, H. Lu, D.W. Zhang, H. Zhu, Stability and strength of atomically thin borophene from first principles calculations, Materials Research Letters. 5 (2017). https://doi.org/10.1080/21663831.2017.1298539.

[52] Y. Zhao, K. Zhu, Organic-inorganic hybrid lead halide perovskites for optoelectronic and electronic applications, Chemical Society Reviews. 45 (2016) 655–689. https://doi.org/10.1039/c4cs00458b.

[53] G. Volonakis, M.R. Filip, A.A. Haghighirad, N. Sakai, B. Wenger, H.J. Snaith, F. Giustino, Lead-free halide double perovskites via heterovalent substitution of noble metals, The Journal of Physical Chemistry Letters. 7 (2016) 1254–1259.

[54] M.A. Green, K. Emery, Y. Hishikawa, W. Warta, E.D. Dunlop, Solar cell efficiency tables (version 46), Progress in Photovoltaics: Research and Applications. 23 (2015) 805–812. https://doi.org/10.1002/pip.2637.

[55] S. Körbel, M.A.L. Marques, S. Botti, Stability and electronic properties of new inorganic perovskites from high-throughput ab initio calculations, Journal of Materials Chemistry C. 4 (2016) 3157–3167. https://doi.org/10.1039/C5TC04172D.

[56] K. Heidrich, W. Schäfer, M. Schreiber, J. Söchtig, G. Trendel, J. Treusch, T. Grandke, H.J. Stolz, Electronic structure, photoemission spectra, and vacuum-ultraviolet optical spectra of $CsPbCl_3$ and $CsPbBr_3$, Phys. Rev. B. 24 (1981) 5642–5649. https://doi.org/10.1103/PhysRevB.24.5642.

[57] L. Peedikakkandy, P. Bhargava, Composition dependent optical{,} structural and photoluminescence characteristics of cesium tin halide perovskites, RSC Adv. 6 (2016) 19857–19860. https://doi.org/10.1039/C5RA22317B.

[58] L.-C. Tang, Y.-C. Chang, J.-Y. Huang, M.-H. Lee, C.-S. Chang, First Principles Calculations of Linear and Second-Order Optical Responses in Rhombohedrally Distorted Perovskite Ternary Halides, $CsGeX_3$ (X = Cl, Br, and I), Japanese Journal

of Applied Physics. 48 (2009) 112402. https://doi.org/10.1143/JJAP.48.112402.

[59] M. Jiang, J. Wu, F. Lan, Q. Tao, D. Gao, G. Li, Enhancing the performance of planar organo-lead halide perovskite solar cells by using a mixed halide source, Journal of Materials Chemistry A. 3 (2015) 963–967. https://doi.org/10.1039/C4TA05373G.

[60] T. Wu, Z. Qin, Y. Wang, Y. Wu, W. Chen, S. Zhang, M. Cai, S. Dai, J. Zhang, J. Liu, Z. Zhou, X. Liu, H. Segawa, H. Tan, Q. Tang, J. Fang, Y. Li, L. Ding, Z. Ning, Y. Qi, Y. Zhang, L. Han, The Main Progress of Perovskite Solar Cells in 2020–2021, Nano-Micro Letters. 13 (2021) 152. https://doi.org/10.1007/s40820-021-00672-w.

[61] X. Wang, H. Xiang, X. Sun, J. Liu, F. Hou, Y. Zhou, Mechanical Properties and Damage Tolerance of Bulk $Yb_3Al_5O_{12}$ Ceramic, Journal of Materials Science & Technology. 31 (2015) 369–374. https://doi.org/10.1016/j.jmst.2015.01.002.

[62] Z. Shi, J. Guo, Y. Chen, Q. Li, Y. Pan, H. Zhang, Y. Xia, W. Huang, Lead-Free Organic–Inorganic Hybrid Perovskites for Photovoltaic Applications: Recent Advances and Perspectives, Advanced Materials. 29 (2017). https://doi.org/10.1002/adma.201605005.

[63] M.D. Segall, P.J.D. Lindan, M.J. al Probert, C.J. Pickard, P.J. Hasnip, S.J. Clark, M.C. Payne, First-principles simulation: ideas, illustrations and the CASTEP code, Journal of Physics: Condensed Matter. 14 (2002) 2717.

[64] S. Baroni, S. De Gironcoli, A. Dal Corso, P. Giannozzi, Phonons and related crystal properties from density-functional perturbation theory, Reviews of Modern Physics. 73 (2001) 515.

[65] [Cramer; J., No Title, 2002. https://www.wiley.com/en-us/Essentials+of+Computational+Chemistry:+Theories+and+Models,+2nd+Edition-p-9780470091821.

[66] F. Jensen, No Title, (2007) 98–149. https://www.wiley.com/en-us/Introduction+to+Computational+Chemistry%2C+3rd+Edition-p-9781118825990.

[67] D.R. Hartree, No Title, (1928) 426. https://www.scirp.org/(S(lz5mqp453edsnp55rrgjct55))/reference/ReferencesPapers.a

spx?ReferenceID=2093600.

[68] M. Segall, O. Limited, M. Probert, P.J. Hasnip, First-Principles Simulation : Ideas , Illustrations and the CASTEP Code First-principles simulation : ideas , illustrations and the CASTEP code, (2002). https://doi.org/10.1088/0953-8984/14/11/301.

[69] V. Singh, D. Joung, L. Zhai, S. Das, S.I. Khondaker, S. Seal, Graphene based materials: Past, present and future, Progress in Materials Science. 56 (2011). https://doi.org/10.1016/j.pmatsci.2011.03.003.

[70] G.P. FW Kutzler, No Title, Phys Rev B Condens Matter . (1992). https://pubmed.ncbi.nlm.nih.gov/10001891/.

[71] P. Durand, J.C. Barthelat, New atomic pseudopotentials for electronic structure calculations of molecules and solids, Chemical Physics Letters. 27 (1974) 191–194. https://doi.org/https://doi.org/10.1016/0009-2614(74)90201-2.

[72] M. Causà, Numerical Integration in Density Functional Methods with Linear Combination of Atomic Orbitals, in: C. Pisani (Ed.), Quantum-Mechanical Ab-Initio Calculation of the Properties of Crystalline Materials, Springer Berlin Heidelberg, Berlin, Heidelberg, 1996: pp. 91–100. https://doi.org/10.1007/978-3-642-61478-1_5.

[73] M.C. Payne, M.P. Teter, D.C. Allan, T.A. Arias, ad J.D. Joannopoulos, Iterative minimization techniques for ab initio total-energy calculations: molecular dynamics and conjugate gradients, Reviews of Modern Physics. 64 (1992) 1045.

[74] M. Caid, D. Rached, S. Al-Qaisi, Y. Rached, H. Rached, DFT calculations on physical properties of the lead-free halide-based double perovskite compound Cs2CdZnCl6, Solid State Communications. 369 (2023) 115216. https://doi.org/https://doi.org/10.1016/j.ssc.2023.115216.

[75] S.J. Clark, M.D. Segall, C.J. Pickard, P.J. Hasnip, M.I.J. Probert, K. Refson, M.C. Payne, First principles methods using CASTEP, Zeitschrift Fur Kristallographie. 220 (2005) 567–570. https://doi.org/10.1524/zkri.220.5.567.65075.

[76] J.P. Perdew, K. Burke, M. Ernzerhof, Generalized gradient approximation made simple, Physical Review Letters. 77 (1996) 3865–3868.

https://doi.org/10.1103/PhysRevLett.77.3865.

[77] H.J. Monkhorst, J.D. Pack, Special points for Brillouin-zone integrations, Physical Review B. 13 (1976) 5188.

[78] C. Truesdell, Murnaghan's Finite Deformation of an Elastic Solid (1952), in: An Idiot's Fugitive Essays on Science, Springer New York, New York, NY, 1984: pp. 148–150. https://doi.org/10.1007/978-1-4613-8185-3_14.

[79] J.D. Pack, H.J. Monkhorst, "special points for Brillouin-zone integrations"-a reply, Physical Review B. 16 (1977) 1748–1749. https://doi.org/10.1103/PhysRevB.16.1748.

[80] J. Islam, S.K. Mitro, M.M. Hossain, M.M. Uddin, N. Jahan, A.K.M.A. Islam, S.H. Naqib, M.A. Ali, Exploration of the physical properties of the newly synthesized kagome superconductor $LaIr_3Ga_2$ using different exchange–correlation functionals, Phys. Chem. Chem. Phys. 24 (2022) 29640–29654. https://doi.org/10.1039/D2CP04054A.

[81] M.A. Ali, M.M. Hossain, M.M. Uddin, M.A. Hossain, A.K.M.A. Islam, S.H. Naqib, Physical properties of new MAX phase borides M_2SB (M = Zr, Hf and Nb) in comparison with conventional MAX phase carbides M_2SC (M = Zr, Hf and Nb): Comprehensive insights, Journal of Materials Research and Technology. 11 (2021) 1000–1018. https://doi.org/10.1016/j.jmrt.2021.01.068.

[82] A. Chowdhury, M.A. Ali, M.M. Hossain, M.M. Uddin, S.H. Naqib, A.K.M.A. Islam, Predicted MAX Phase Sc_2InC: Dynamical Stability, Vibrational and Optical Properties, Physica Status Solidi (B). 255 (2017) 1700235. https://doi.org/10.1002/pssb.201700235.

[83] M.H.K. Rubel, M. Mozahar Ali, M.S. Ali, R. Parvin, M.M. Rahaman, K.M. Hossain, M.I. Hossain, A.K.M.A. Islam, N. Kumada, First−principles study: Structural, mechanical, electronic and thermodynamic properties of simple−cubic−perovskite $(Ba_{0.62}K_{0.38})(Bi_{0.92}Mg_{0.08})O_3$, Solid State Communications. 288 (2019) 22–27. https://doi.org/10.1016/j.ssc.2018.11.008.

[84] M. Born, On the stability of crystal lattices. I, Mathematical Proceedings of the

Cambridge Philosophical Society. 36 (1940) 160–172. https://doi.org/DOI: 10.1017/S0305004100017138.

[85] A. Bouhemadou, R. Khenata, M. Kharoubi, Y. Medkour, First-principles study of structural and elastic properties of Sc_2AC (A= Al, Ga, In, Tl), Solid State Communications. 146 (2008) 175–180.

[86] Y. Rakita, S.R. Cohen, N.K. Kedem, G. Hodes, D. Cahen, Mechanical properties of $APbX_3$ (A = Cs or CH_3NH_3; X= I or Br) perovskite single crystals, MRS Communications. 5 (2015) 623–629. https://doi.org/10.1557/mrc.2015.69.

[87] M.M. Woolfson, Solid state physics 3. Theory of lattice dynamics in the harmonic approximation by A. A. Maradudin, E. W. Montroll, G. H. Weiss and I. P. Ipatova, Acta Crystallographica Section A. 29 (1973) 314. https://doi.org/10.1107/S0567739473000859.

[88] M.T. Nasir, M.A. Hadi, M.A. Rayhan, M.A. Ali, M.M. Hossain, M. Roknuzzaman, S.H. Naqib, A.K.M.A. Islam, M.M. Uddin, K. Ostrikov, First-Principles Study of Superconducting ScRhP and ScIrP pnictides, Physica Status Solidi (B). 254 (2017) 1700336. https://doi.org/https://doi.org/10.1002/pssb.201700336.

[89] M.M. Rahaman, M.H.K. Rubel, M.A. Rashid, M.A. Alam, K.M. Hossain, M.I. Hossain, A.A. Khatun, M.M. Hossain, A.K.M.A. Islam, S. Kojima, N. Kumada, Mechanical, electronic, optical, and thermodynamic properties of orthorhonmbic $LiCuBiO_4$ crystal: a first–priciples study, Journal of Materials Research and Technology. 8 (2019) 3783–3794. https://doi.org/10.1016/j.jmrt.2019.06.039.

[90] H. Rached, D. Rached, S. Benalia, A.H. Reshak, M. Rabah, R. Khenata, S. Bin Omran, First-principles study of structural stabilities, elastic and electronic properties of transition metal monocarbides (TMCs) and mononitrides (TMNs), Materials Chemistry and Physics. 143 (2013) 93–108. https://doi.org/https://doi.org/10.1016/j.matchemphys.2013.08.020.

[91] H. Rached, S. Bendaoudia, D. Rached, Investigation of Iron-based double perovskite oxides on the magnetic phase stability, mechanical, electronic and optical properties via first-principles calculation, Materials Chemistry and Physics. 193 (2017) 453–469.

https://doi.org/https://doi.org/10.1016/j.matchemphys.2017.03.006.

[92] X.-Q. Chen, H. Niu, D. Li, Y. Li, Modeling hardness of polycrystalline materials and bulk metallic glasses, Intermetallics. 19 (2011) 1275–1281. https://doi.org/https://doi.org/10.1016/j.intermet.2011.03.026.

[93] E. Mazhnik, A.R. Oganov, A model of hardness and fracture toughness of solids, Journal of Applied Physics. 126 (2019) 125109. https://doi.org/10.1063/1.5113622.

[94] F. Gao, Theoretical model of intrinsic hardness, Physical Review B. 73 (2006) 132104. https://doi.org/10.1103/PhysRevB.73.132104.

[95] M.F. Cover, O. Warschkow, M.M.M. Bilek, D.R. McKenzie, A comprehensive survey of M_2AX phase elastic properties, Journal of Physics: Condensed Matter. 21 (2009) 305403.

[96] S.F. Pugh, XCII. Relations between the elastic moduli and the plastic properties of polycrystalline pure metals, The London, Edinburgh, and Dublin Philosophical Magazine and Journal of Science. 45 (1954) 823–843. https://doi.org/10.1080/14786440808520496.

[97] I.N. Frantsevich, F.F. Voronov, I.N. Frantsevich, Elastic Constants and Elastic Moduli of Metals and Insulators Handbook, (1983) 60–180.

[98] D.G. Pettifor, Theoretical predictions of structure and related properties of intermetallics, Materials Science and Technology. 8 (1992) 345–349.

[99] M. Jamal, S. Jalali Asadabadi, I. Ahmad, H.A. Rahnamaye Aliabad, Elastic constants of cubic crystals, Computational Materials Science. 95 (2014) 592–599. https://doi.org/https://doi.org/10.1016/j.commatsci.2014.08.027.

[100] D. Vanderbilt, Rapid Communications Soft self-consistent pseudopotentials in a generalized eigenvalue formalism, n.d. file:///C:/Users/tahaitlink/AppData/Local/Mendeley Ltd./Mendeley Desktop/Downloaded/Vanderbilt - Unknown - Rapid Communications Soft self-consistent pseudopotentials in a generalized eigenvalue formalism.pdf.

[101] B.H. Elias, B.M. Ilyas, N.S. Saadi, A first principle study of the perovskite lanthanum

aluminate, Materials Research Express. 5 (2018) 86302. https://doi.org/10.1088/2053-1591/aad15f.

[102] Y.H. Chang, C.H. Park, K. Matsuishi, First-principles study of the structural and the electronic properties of the lead-halide-based inorganic-organic perovskites (CH_3NH_3)PbX_3 and $CsPbX_3$ (X = Cl, Br, I), Journal of the Korean Physical Society. 44 (2004) 889–893.

[103] G. Murtaza, I. Ahmad, First principle study of the structural and optoelectronic properties of cubic perovskites $CsPbM_3$ (M=Cl, Br, I), Physica B: Condensed Matter. 406 (2011) 3222–3229. https://doi.org/https://doi.org/10.1016/j.physb.2011.05.028.

[104] M. Afsari, A. Boochani, M. Hantezadeh, Electronic, optical and elastic properties of cubic perovskite $CsPbI_3$: Using first principles study, Optik. 127 (2016) 11433–11443. https://doi.org/https://doi.org/10.1016/j.ijleo.2016.09.013.

[105] I.R. Shein, A.L. Ivanovskii, Elastic properties of superconducting MAX phases from first-principles calculations, Physica Status Solidi (B). 248 (2011) 228–232.

[106] M. Tomasik, N. Mangan, J. Grossman, Photovoltaic efficiency of an indirect bandgap material, in: APS March Meeting Abstracts, 2015: p. L34.011.

[107] S. Azam, S. Goumri-Said, S.A. Khan, M.B. Kanoun, Electronic, optical and thermoelectric properties of new metal-rich homological selenides with palladium–indium: Density functional theory and Boltzmann transport model, Journal of Physics and Chemistry of Solids. 138 (2020) 109229. https://doi.org/https://doi.org/10.1016/j.jpcs.2019.109229.

[108] S.A. Dar, R. Sharma, V. Srivastava, U.K. Sakalle, Investigation on the electronic structure, optical, elastic, mechanical, thermodynamic and thermoelectric properties of wide band gap semiconductor double perovskite Ba_2InTaO_6, RSC Advances. 9 (2019) 9522–9532. https://doi.org/10.1039/C9RA00313D.

[109] V. Kumar, A. Dey, S. Thomas, M. Asle Zaeem, D.R. Roy, Hydrogen-induced tunable electronic and optical properties of a two-dimensional penta-Pt 2 N 4 monolayer, Physical Chemistry Chemical Physics. 23 (2021) 10409–10417. https://doi.org/10.1039/D1CP00681A.

[110] H.M. Ghaithan, Z.A. Alahmed, S.M.H. Qaid, M. Hezam, A.S. Aldwayyan, Density Functional Study of Cubic, Tetragonal, and Orthorhombic $CsPbBr_3$ Perovskite, ACS Omega. 5 (2020). https://doi.org/10.1021/acsomega.0c00197.

[111] M. Roknuzzaman, M.A. Hadi, M.A. Ali, M.M. Hossain, N. Jahan, M.M. Uddin, J.A. Alarco, K. Ostrikov, First hafnium-based MAX phase in the 312 family, Hf_3AlC_2: A first-principles study, Journal of Alloys and Compounds. 727 (2017) 616–626.

[112] M.D.B. Daniel C. Harris (Author), Symmetry and Spectroscopy: An Introduction to Vibrational and Electronic Spectroscopy (Dover Books on Chemistry), Dover Publications; New edition, 1989.

[113] A. Chowdhury, M.A. Ali, M.M. Hossain, M.M. Uddin, S.H. Naqib, A. Islam, Predicted MAX phase Sc2InC: dynamical stability, vibrational and optical properties, Physica Status Solidi (B). 255 (2018) 1700235.

[114] K. Ephraim Babu, N. Murali, K. Vijaya Babu, P. Taddesse Shibeshi, V. Veeraiah, Structural, Elastic, Electronic, and Optical Properties of Cubic Perovskite $CsCaCl_3$ Compound: An ab initio Study, Acta Physica Polonica A. 125 (2014) 1179–1185. https://doi.org/10.12693/APhysPolA.125.1179.

[115] O.L. Anderson, A simplified method for calculating the debye temperature from elastic constants, Journal of Physics and Chemistry of Solids. 24 (1963) 909–917. https://doi.org/https://doi.org/10.1016/0022-3697(63)90067-2.

[116] N. Mendelson, M. Doherty, M. Toth, I. Aharonovich, T.T. Tran, Strain-Induced Modification of the Optical Characteristics of Quantum Emitters in Hexagonal Boron Nitride, Advanced Materials. 32 (2020). https://doi.org/10.1002/adma.201908316.

[117] Y. Shen, D.R. Clarke, P.A. Fuierer, Anisotropic thermal conductivity of the Aurivillus phase, bismuth titanate ($Bi_4Ti_3O_{12}$): A natural nanostructured superlattice, Applied Physics Letters. 93 (2008). https://doi.org/10.1063/1.2975163.

[118] K.S. Novoselov, A.K. Geim, S. V Morozov, D. Jiang, Y. Zhang, S. V Dubonos, I. V Grigorieva, A.A. Firsov, Electric Field Effect in Atomically Thin Carbon Films Supplementary, Science. 5 (2004) 1–12. https://doi.org/10.1126/science.aab1343.

[119] M. Mattesini, M. Magnuson, F. Tasnádi, C. Höglund, I.A. Abrikosov, L. Hultman, Elastic properties and electrostructural correlations in ternary scandium-based cubic inverse perovskites: A first-principles study, Physical Review B - Condensed Matter and Materials Physics. 79 (2009) 1–9. https://doi.org/10.1103/PhysRevB.79.125122.

[120] M. Naguib, V.N. Mochalin, M.W. Barsoum, Y. Gogotsi, 25th anniversary article: MXenes: A new family of two-dimensional materials, Advanced Materials. 26 (2014). https://doi.org/10.1002/adma.201304138.

[121] M.A. Ali, M.M. Hossain, M.M. Uddin, M.A. Hossain, A.K.M.A. Islam, S.H. Naqib, Physical properties of new MAX phase borides M_2SB (M = Zr, Hf and Nb) in comparison with conventional MAX phase carbides M_2SC (M = Zr, Hf and Nb): Comprehensive insights, Journal of Materials Research and Technology. 11 (2021) 1000–1018. https://doi.org/10.1016/j.jmrt.2021.01.068.

[122] M.A. Ali, M.S. Ali, M.M. Uddin, Structural, elastic, electronic and optical properties of metastable MAX phase Ti5SiC4 compound, Indian Journal of Pure and Applied Physics. 54 (2016) 386–390.

[123] P. Debye, Zur theorie der spezifischen wärmen, Annalen Der Physik. 344 (1912) 789–839.

[124] M.A. Blanco, E. Francisco, V. Luaña, GIBBS: Isothermal-isobaric thermodynamics of solids from energy curves using a quasi-harmonic Debye model, Computer Physics Communications. 158 (2004) 57–72. https://doi.org/10.1016/j.comphy.2003.12.001.

[125] S. Cui, W. Feng, H. Hu, Z. Feng, H. Liu, Hexagonal Ti_2SC with high hardness and brittleness: a first-principles study, Scripta Materialia. 61 (2009) 576–579. https://doi.org/10.1016/j.scriptamat.2009.05.026.

[126] M.A. Hadi, M. Roknuzzaman, A. Chroneos, S.H. Naqib, A.K.M.A. Islam, R. V. Vovk, K. Ostrikov, Elastic and thermodynamic properties of new $(Zr_{3-x}Ti_x)AlC_2$ MAX-phase solid solutions, Computational Materials Science. 137 (2017) 318–326. https://doi.org/10.1016/j.commatsci.2017.06.007.

Materials Today Communications xxx (xxxx) 109422

Contents lists available at ScienceDirect

Materials Today Communications

journal homepage: www.elsevier.com/locate/mtcomm

An inclusive study of lead-free perovskite $CsMI_3$ materials for photovoltaic and optoelectronic appliance explored by a first principles study

M. Biswas [a], S. Ghosh [b], J. Chowdhury [b], M.A. Ali [a], M.M. Hossain [a], S.H. Naqib [c], M.M. Uddin [a, *]

[a] Department of Physics, Chittagong University of Engineering & Technology, Pahartali, Chittagong 4349, Bangladesh
[b] Department of Physics, Jadavpur University, 188, Raja S.C. Mallick Road, Kolkata 700032, India
[c] Department of Physics, University of Rajshahi, Rajshahi 6205, Bangladesh

ARTICLE INFO

Keywords:
Perovskite
First-principles calculation
Electronic properties
Optical properties
Solid solutions

ABSTRACT

The prime objective of this study is to understand the lead-free $CsMI_3$ (M = Pb, Mg, Ga, Ca, Ba, Sr) perovskites for photovoltaic and optoelectronic applications using first-principle calculations. This study considered the structural aspects along with the mechanical, electrical, optical, and thermal properties. The formation energy, phonon dispersion curve, and elastic constants were calculated to check the structural stability of the compounds. The computed Poisson ratios (ν) support the $CsMI_3$ compounds' ductility; only the $CsMgI_3$ compounds lie on the ductile-brittle transition line. However, the compounds' ductility is confirmed by the Cauchy pressure, which also reflects the materials' mechanism of mechanical failure. The band structure calculations confirmed the energy band gap, E_g, in the range of 1.63–3.26 eV, which makes them suitable for absorbing materials in solar cell applications. The optical properties calculations revealed strong photoconductivity, low reflectivity, and high absorption coefficient, all of which show photovoltaic properties given the materials use in the solar cell application. Among the titled compounds, $CsMgI_3$ will be the best replacement of Pb-based perovskites for photovoltaic and optoelectronic appliances. The substitution of I by Br in the $CsMgI_3$ causes a significant improvement (band gap is increased from 1.12 to 1.87 eV; absorption coefficient is also increased) in the photovoltaic properties. The E_g and α further increase due to doping into the $CsMg(I_{1-x}Br_x)_3$ where $x = (0.25)$ makes them apposite for solar cell materials. The best combination, $CsMg(I_{0.75}Br_{0.25})_3$, shows $E_g \sim 1.4$ eV, which may be considered as the optimum band gap for the highest efficiency of a single solar cell according to the Shockley-Queisser limit.

1. Introduction

Because of the rapid changes in the global economic and social landscape, the more energy is required than traditional fossil fuels can provide. Solar energy will undoubtedly offer a variety of benefits, like being renewable and pollution-free, given that it is destined to be the primary energy source in the 4IR. In nature, metal halide perovskites (MHP) are commonly accessible and reasonably priced. Consequently, solar cells based on these materials would be more economical and efficient than silicon-based photovoltaic (PV) technology [1,2]. Due to their remarkable opto-electronic properties which include a tunable bandgap, high optical absorption, broad absorption spectrum, small carrier effective mass, long charge diffusion length, and high charge carrier mobility [1,3–12], the MHPs have recently attracted a great deal of attention from the scientific community. In recent times, there has been a significant increase in the power conversion efficiency (PCE) of lead (Pb)-based metal halide perovskite solar cells (MHPSCs) from 3.8 % to 25.5 % [13–15]. Additionally, a significant number of MHPSCs have successfully passed a test of the 1,000-hour operational stability benchmark [16,17]. Lead halide perovskites have been used to create devices with the power conversion efficiency of about 22 % [18], which is comparable to materials used in conventional solar cells such as cadmium telluride (CdTe), copper indium gallium selenide (CIGS), and single-crystal Si [13]. $CH_3NH_3PbI_3$, a typical hybrid organic-inorganic halide perovskite, features a bandgap that is close to the Shockley–Queisser optimum, [19,20] significant visible spectrum absorption, [21,22] long carrier lives, [23,24] high charge carrier mobilities, [25–27] and long carrier lifetimes. As a result, in a solar cell, $CH_3NH_3PbI_3$ can function as a charge-transporting layer that is both effective and light-absorbing. On the other hand, poisoning of lead is a significant environmental hazard. Because lead perovskites tend to break down in ambient circumstances and release toxic chemicals like PbI_2, using lead is especially hazardous [28]. These Pb-based high-efficiency PSCs [$MAPbI_3$, $FAPbI_3$, $Cs_{0.05}$ $FA_{0.85}$ $MA_{0.10}$ Pb $(I_{0.97}$ $Br_{0.03})_3$]

* Corresponding author.
E-mail address: mohi@cuet.ac.bd (M.M. Uddin).

https://doi.org/10.1016/j.mtcomm.2024.109422
Received 22 March 2024; Received in revised form 29 May 2024; Accepted 31 May 2024
2352-4928/

do, however, have certain inevitable drawbacks, namely, that lead is a poisonous element that is difficult for organisms and the environment to remove from the body. According to research, lead ion poisoning of soil and water sources is persistent and has a highly severe effect on plant, animal, and human survival [29–31]. Because lead may enter the body, attach to an enzyme, and then build up through blood circulation in soft tissues and bones such as the brain, liver, kidney, and spleen. The afflicted person's neurological, digestive, and circulatory systems gradually develop functional problems as a result of lead poisoning. Most people usually start showing symptoms of lead poisoning when their daily lead consumption hits 0.5 mg [30,31]. Thus, various non- or low-toxic metal ions must be selected to substitute lead as PSC perovskite absorbers in order to guarantee that the natural environment for people is safe and pollution-free [32–35].

ABX_3, where X is a halogen anion, B is a metal cation, and A is an organic cation, is the general chemical formula for metal halide perovskites [36–39]. Here, the halogen anion is often made up of Cl, Br, I, or their mixture, while the organic cation is typically composed of methylammonium (MA), formamidinium (FA), Cs, or their mixture. Regarding B, prior research has demonstrated that less hazardous ions such as Sn^{2+}, Bi^{3+}, Ge^{2+}, Sb^{3+}, $Mn^{2}+$, and Cu^{2+} may be substituted for Pb^{2+} in perovskites to create a novel lead-free structure [12,40,41]. The addition of these metal cations improves PSCs' ecologically beneficial qualities while also broadening the variety of perovskite species. It is crucial to look for novel B metals and their solid solutions as well as opto-electronic properties in order to create highly efficient solar cells based on Pb-free MHPSCs. Furthermore, MHP solar cells would be more economical and efficient than photovoltaic (PV) technology based on silicon. Due to these remarkable properties, this family of semiconductors may be used in light-emitting diodes, photodetectors, and solar-to-fuel energy conversion devices, among other electronic devices, in addition to solar cells [1,4,11,12]. In order to forecast a particular device application and advancements, a more profound and basic comprehension of the semiconductor features is required. Furthermore, an examination of a material's optical functions can reveal information about how it responds to light. Therefore, for a material to be employed in real-world optoelectronic devices like solar cells, diodes, lasers, etc., a detailed understanding of the optical characteristics is required. When choosing a certain perovskite material to utilize as the absorbance/active layer in the solar cell construction, metrics such as the energy (wavelength) dependent absorption coefficient, shallow acceptor density (N_A), shallow donor density (N_D), etc., are crucial to know. To determine the efficiency, these factors must be entered into a simulation of the solar cell structure. However, only a few investigations have been done on the perovskite compounds' optical characteristics. The regular and frequent modelling of perovskite-based solar cells, which is crucial to the advancement of the cell like the well-known CdTe or CIGS based solar cell structure, was hampered by the lack of perovskite material properties. Based on the low electron effective mass, which is caused by exceptionally dispersive conduction bands, and band gap tuning between 0.9 and 1.7 eV (1.7 eV for $CsMgI_3$, 1.5 eV for $CH_3NH_3MgI_3$, and 0.9 eV for $CH(NH_2)_2MgI_3$), ten compounds out of 248 candidates have been identified for potential solar cell applications with high-throughput screening [42]. In order to make these compounds suitable for optoelectronic and photovoltaic applications, certain proposed lead-free perovskites (M = Mg, Ga, Ca, Ba and Sr) with Mg, Ca, Ba, and Sr being alkaline-earth metals were tuned here to predict their optoelectronic characteristics [42,43].

In this context, Pb-free inorganic MHP compounds have been examined using first-principles density functional theory (DFT) to comprehend their overall properties. The main objective of this study is to explore new material(s) that may be considered as the alternative of lead-based solar cell materials in terms of properties and performance. To do this, the structural features, mechanical, thermodynamic, electronic, and optical properties of Pb-free MHPs, $CsMI_3$ (M = Mg, Ga, Ca, Ba, and Sr) have been investigated. It is found that $CsMgI_3$ could be a potential alternative to $CsPbI_3$ for photovoltaic applications.

2. Computational methodology

The current DFT [44] -based computations were performed using the CAmbridge Serial Total Energy Package (CASTEP) algorithm by the Materials Studio 8.0 module. This method has proven to be one of the most accurate methods for the calculation of electronic structures [45]. For all computations, the pseudopotential of Vanderbilt type [46] was utilized to handle the electron-ion interaction. Using the generalized gradient approximation (GGA) of Perdew-Berke-Ernzerhof (PBE) [47], the exchange-correlation energy was calculated. The Broyden–Fletcher–Goldfarb–Shanno (BFGS) [48] minimization approach was applied in order to maximize the crystal structure and determine the ground state energy. The finite strain theory [49], which was implemented within the CASTEP module, was used to derive elastic constants. By varying the M cations, all of the characteristics of $CsMI_3$ (M = Pb, Mg, Ga, Ca, Ba, and Sr) were calculated. For all cubic $CsMI_3$ computations, the electronic wave function with a cutoff energy of 500 eV was utilized. The irreducible Brillouin zone was sampled using 11 × 11 × 11 *k*-point grids following the Monkhorst-Pack technique [50]. The current computations were conducted with the following convergence limits: 1×10^{-6} eV/atom for total energy, 0.03 eV/Å for maximum force on atoms, 0.001 Å for maximum atom displacements, and 0.05 GPa for maximum stress. The electronic band gaps of the studied compounds have been further estimated with the help of Quantum ESPRESSO suite of software [51].

3. Results and discussion

3.1. Structural properties

The $CsMI_3$ (M = Pb, Mg, Ga, Ca, Ba, and Sr) compounds crystallize in the cubic system with space group Pm3m (no. 221). As seen in Fig. 1, the material's unit cell is made up of five atoms with a single formula unit. Within the structure, the Cs atom is positioned in the corner with a

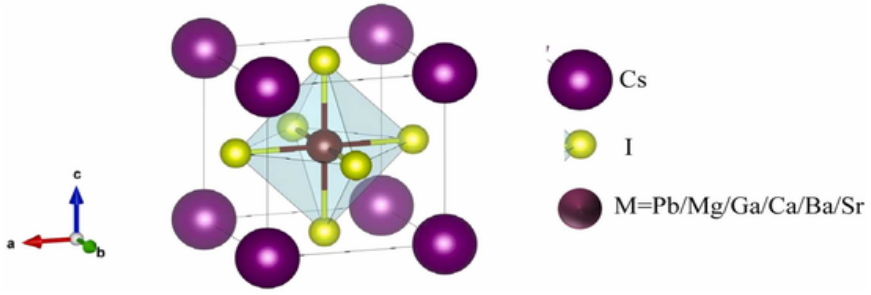

Fig. 1. Cubic crystal structure of $CsMI_3$ metal halide perovskite compounds (M = Pb, Mg, Ga, Ca, Ba, Sr).

1a Wyckoff site and (0, 0, 0) fractional coordinates; M is positioned in the body center with a 1b Wyckoff site and (1/2, 1/2, 1/2) fractional coordinates; and the I atom is positioned in the face center with a 3c Wyckoff site and (0, 1/2, 1/2) fractional coordinates. Ray [43] also reported the orthorhombic phase of stoichiometric $CsMI_3$ (M = Pb, Mg, Ga, Ca, Ba, and Sr), but the cubic phase has been considered in this study using the available refinement data. The lattice parameters and internal coordinates were completely loosened in order to improve the geometry by switching the M site cation. PBE functional is used to compute the optimal lattice parameters and cell volume of $CsMI_3$ substances, as seen in Fig. 2. The hybrid DFT functionals, like HSE06, can correctly predict some experimentally measured band gaps in some materials, but the structural properties, like lattice parameters, significantly deviate from the experimental values. It is well known that the calculation of the accurate lattice parameter is one of the key factors estimating in the physical properties using DFT calculations accurately [52]. However, it is found that the properties of the HSE06 functional differed from those of other functionals, like GGA-PBE. Because of this, PBE is used as a benchmark in the calculations to account for the correctness of the results.

3.2. Stability of the structures

3.2.1. Formation energy (E_f)

The chemical stability of $CsMI_3$ can be confirmed by analyzing their formation energies. The subtraction of the total energies of pure constituent atoms from the total energy of the materials in their stable structures determines the formation energy (E_f). The following expression is used to estimate the formation energy of $CsMI_3$ [53]:

$$\Delta E_f\left(CsMI_3\right) = \left[E_{tot}\left(CsMI_3\right) - E_s\left(Cs\right) - E_s\left(M\right) - 3E_s\left(I\right)\right] \quad (1)$$

Here, E_{tot} $(CsMI_3)_{fu}$ represents the total energy per formula unit and is given by E_{tot} $(CsMI_3)_{fu}$ = $1/N[E_{tot}(CsMI_3)_{cell}]$.where N denotes the number of formula units per unit cell. E_s(Cs), E_s(M), and E_s(I) are the total energies per atom of the pure elements Cs, M, and I, respectively, in their ground-state solid phases. So, the $\Delta E_f\left(CsMI_3\right)$ per atom is given by $\Delta E_f\left(CsMI_3\right)_{fu}/N_t$, where N_t denotes the total number of atoms in one formula unit, gives the desired parameter. The calculated formation energies of perovskites $CsMI_3$ are found to be $CsBaI_3$ (-2.254 eV/atom) > $CsCaI_3$ (-2.249 eV/atom) > $CsSrI_3$ (-2.239 eV/atom) > $CsMgI_3$(-1.81 eV/atom) > $CsPbI_3$(-1.624 eV/atom) > $CsGaI_3$(-1.326 eV/atom). The energy required (or released) to generate a configuration is understood to be its formation energy. Consequently, endothermic and exothermic processes can occur during the creation of a structure. According to [54], a sheet's structure is more stable when its creation energy is lower. That sort of denotes a sheet's energy (thermal) stability. The chemicals can be produced since the values are negative, suggesting that they are stable energetically. The particulars are presented in the supplementary Table-1 that are used to calculate the formation energies of $CsMI_3$ (M = Pb, Mg, Ga, Ca, Ba, Sr) compounds.

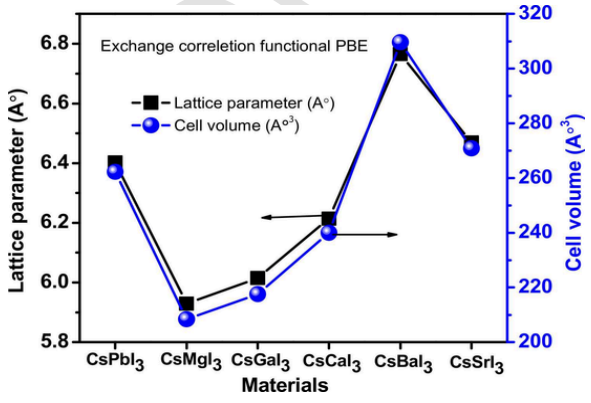

Fig. 2. Lattice parameter (Å) and cell volume ($Å^3$) of the metal halide perovskites (MHP) crystal structure of $CsMI_3$ (M= Pb, Mg, Ga, Ca, Ba, Sr).

3.2.2. The dynamical stability

The dynamic stability of a material is an important criterion for assessing its appropriateness in real-world settings involving time-varying external stimuli. It is likely that materials that are formed at any temperature will not always be stable. For example, materials formed at high temperatures could not be stable when brought to a lower temperature. The phonon frequency is dependent on the temperature of the crystal lattice. To confirm the stability of the synthesized perovskite at low temperatures, the phonon dispersion curve (PDC) is calculated in the ground state using the density functional perturbation theory (DFPT) finite-displacement approach. The phonon frequency that is used to evaluate stability over the whole Brillouin Zone (BZ) is displayed in Fig. 3(a,b), and supplementary Fig. 1(a-d) displays the remaining compounds $CsMI_3$ (M = Ga, Ca, Ba, Sr) PDC. Negative frequencies at any *k*-point indicate the instability of the compounds, whereas positive frequencies indicate their stability [55,56]. Fig. 3(a, b) shows that none of the compounds exhibit imaginary or negative frequencies, indicating that they are dynamically stable. This finding aligns with the section on structural attributes, which states that all phases under study have a negative formation energy. This suggests that the compounds might potentially be produced by experimentation. Five atoms make up the unit cells of the perovskite phases, leading to 15 phonon branches, 12 of which are optical modes and 3 of which are acoustic modes. Acoustic modes stay at the bottom of the phonon dispersion curves, whereas optical modes make up the top branch. Acoustic branches are created by in-phase vibrations of atoms in a lattice outside of their balance position. The calculated total phonon density of states (PHDOS) for $CsMI_3$ is shown in Fig. 3(a,b). The sources of the PHDOS peaks include the bands' general flat appearance and the fact that the overall DOS peak is in lower bands because of their dispersive nature.

3.3. Mechanical properties

For industrial applications of engineering materials, the research of various physical properties such as elastic anisotropy, brittle and ductile nature, and elastic moduli is essential. The linear finite stress-strain method in the CASTEP algorithm yields the elastic constants C_{ij} [49]. Table 1 shows the three independent elastic constants for cubic $CsMI_3$ that were calculated: C_{11}, C_{12}, and C_{44}. The Born stability criteria, which are frequently expressed in terms of C_{ij} and therefore based on free energy considerations, may be used to derive the elastic constants, which are crucial to forecasting the mechanical stability of a crystal [57]. The spinodal, shear, and Born conditions for mechanical stability of a cubic crystal are $C_{11} + 2\,C_{12} > 0$, $C_{11} - C_{12} > 0$, and $C_{44} > 0$, respectively. It is analogous to requiring a positive bulk modulus, B, to apply the spinodal criteria. Therefore, for a cubic crystal to be mechanically stable, its phases must have positive values for the elastic constants B, $C_{11} - C_{12}$, and C_{44}, as shown in Table 1. An elastic material's propensity to deform non-permanently in various directions when subjected to stress is determined by this feature. Information regarding the bonding behavior of solids is also provided by the elastic constants. The elasticity along the axial length is given by the elastic constant C_{11}. Therefore, the value of C_{11} may be used to represent the elastic stiffness of materials against the ⟨100⟩ uniaxial strain of the (100) plane. The elastic constants C_{12} and C_{44} stand for the pure shear stress in the (110) plane along the ⟨110⟩ direction and the shear stress in the (010) plane along the ⟨001⟩ direction, respectively. Table 1 shows that, in compari-

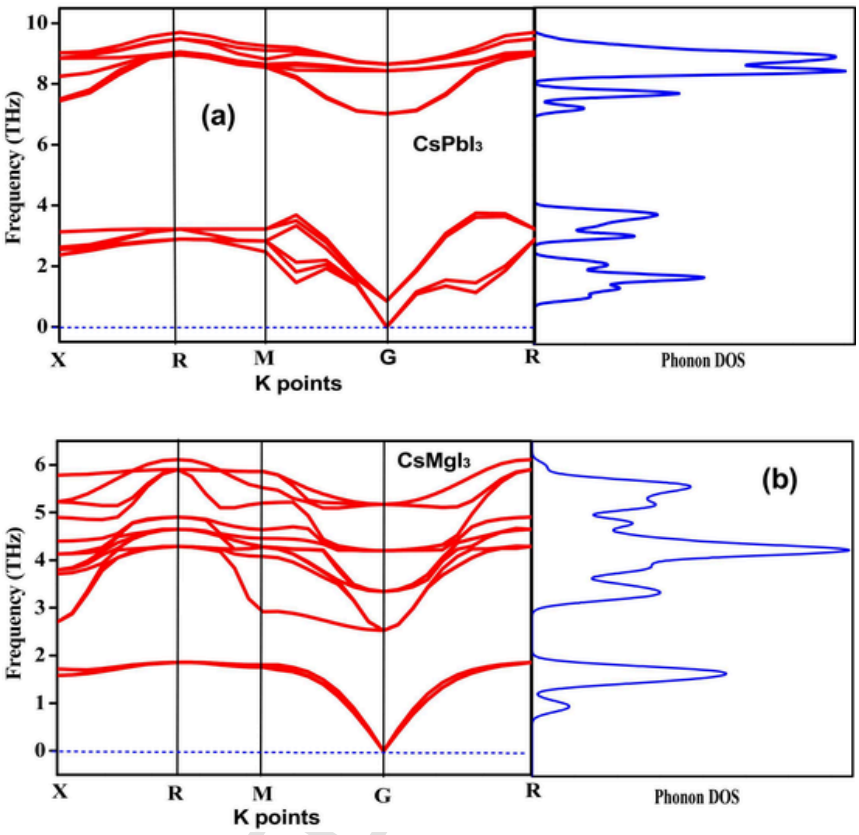

Fig. 3. (a,b): Phonon dispersion curves and PHDOS of $CsMI_3$ (M = Pb, Mg) compounds.

son to the other compounds, $CsPbI_3$ has the highest value of C_{11}. The computed value of C_{11} for all perovskites is greater than C_{12}, which is noteworthy because it suggests that the bonding strength in $CsMI_3$ is stronger along the ⟨100⟩ direction than it is along the ⟨110⟩ direction. Table 1 provides an overview of the different elastic characteristics, which are computed from the single-crystal zero-pressure elastic constants using established relationships [58]. These values include the bulk modulus, B, shear modulus, G, Young's modulus, Y, and Poisson's ratio, v. Rakita et al. found the elastic moduli experimentally for $CsPbI_3$ [59]. The bulk modulus determines the average bond strength of the component atoms in a material [60]. Through observation of the bulk modulus of 101 GPa, Rahaman et al. recently found moderate bonding strength in $LiCuBiO_4$ [61]. However, the bulk moduli of 190 GPa and 171 GPa, respectively, indicated significant bonding strength in ScIrP and ScRhP, according to Nasir et al. [62]. As a result, the computed values of B in the 19.65 – 11.39 GPa range (Table 1) may indicate that the atoms in $CsMI_3$ have weak bonding strengths, and these are soft materials in nature. Table 1 also shows that changing the cations from Ba to Mg increases the bulk modulus. The cationic size increases the bulk modulus of $CsMI_3$ by decreasing the compounds' compressibility and creating a dense solid. The necessary resistance to volume deformation under external pressure is also provided by the binding strength of atoms. On the other hand, the G measures how a solid change in form, and it shows a significant correlation with the hardness of the material. As the value of G increases, the material gets stiffer. The solid matter's resistance to heat shock is influenced by Young's modulus, Y. In relation to Y, the critical thermal shock coefficient changes inversely [63]. The better the thermal shock resistance, the higher the value of the thermal shock coefficient. Thermal shock resistance is a determining factor in the selection of a material for a thermal barrier coating (TBC). Because of its notably reduced Young's modulus, $CsMI_3$ may be a good choice for a TBC material. Higher values of G and Y denote stiffness, whereas the computed value of Y (28.24 – 12.20 GPa) suggests that $CsMI_3$ is moderately flexible [64–66]. In addition to being helpful in explaining the mechanical characteristics of solids, the moduli of elasticity, such as G, B, and Y, are also a reliable way to gauge the hardness. Of the measured elastic constants, C_{44} is the most accurate in predicting the hardness of materials. Furthermore, among the moduli of elasticity, the shear modulus (G) is thought to be the most accurate indicator of hardness. Table 1 makes it clear that $CsMgI_3$ is more durable than the other compounds examined in this investigation. The hardness calculations using Chen's formula [67] support these claims. Table 1 presents the estimated values of macro and micro hardness, which are in line with previous predictions based on C_{44} and G values. Mazhnik and Oganov [68] show favorable agreement between the theoretical and experimental hardness values of various materials computed using Chen's formula. It is commonly known that superhard materials such as diamond (H_V = 96 GPa), BC_2N (H_V = 76 GPa), and BC_5 (H_V = 71 GPa) are utilized extensively [68]. Therefore, the fact that $CsMI_3$ has a substantially lower hardness than superhard materials verifies that the compounds under study are not hard materials. Vickers hardness, however, is primarily a measure of the material's resistance to plastic deformation. A knowledge of a solid's hardness can lead to the prediction of many significant applications for useful devices. Additionally, a thorough comprehension of the mechanical behavior may be attained by examining the connection between hardness and elastic polycrystalline modules. Table 1 shows the assessed Vickers hardness values for $CsMI_3$ (M = Pb, Mg, Ga, Ca, Ba, and Sr). This table makes it very evident that $CsMgI_3$ is less hard than $CsPbI_3$ and that $CsGaI_3$ is tougher than $CsPbI_3$. Even so, compared to the most stiff materials (Vickers hardness 70–150 GPa) [69], the

Table 1
The Elastic constants, C_{ij} (GPa), Bulk Moduli, B (GPa), Shear Moduli, G (GPa), Young's Moduli, Y (GPa), Pugh's ratio, Poisson's ratio, Kleinman Parameter (ξ), Cauchy pressure, Machinability index U_M, Macro, Micro hardness and shear anisotropy (*A*).

Parameter	$CsPbI_3$	$CsMgI_3$	$CsGaI_3$	$CsCaI_3$	$CsBaI_3$	$CsSrI_3$	References
C_{11}	39.54	34.81	29.22	34.06	28.07	28.39	This work
	34.23						[35]
C_{12}	6.68	12.07	7.05	7.67	3.049	4.03	This work
	4.46						[35]
C_{44}	5.34	11.09	2.24	6.63	2.008	3.15	This work
	4.24						(64)
B	17.64	19.65	14.44	16.46	11.39	12.15	This work
	14.38						[35]
	23						[77]
	19.8						[78]
	14.4						[79]
G	8.55	11.2	4.53	8.76	4.62	5.62	This work
	6.30						[35]
	7.9						[79] Exp.
Y	22.07	28.24	12.31	22.33	12.2	14.61	This work
	14.49						[35]
	20.1						[79] Exp.
B/G	2.06	1.75	3.19	1.88	2.47	2.16	This work
ν	0.29	0.26	0.36	0.27	0.32	0.3	This work
	0.33						[79] Exp.
Kleinman Parameter (ξ).	0.32	0.49	0.39	0.38	0.26	0.29	This work
Cauchy Pressure (GPa)	1.34	0.98	4.81	1.04	1.041	0.88	This work
$U_M = B/C_{44}$	3.3	1.77	6.45	2.48	5.67	3.86	This work
H_{macro}	0.01	1.26	1.75	0.40	1.30	0.77	This work
H_{micro}	1.20	1.80	0.42	1.35	0.55	0.75	This work
A	0.67	0.20	0.60	0.50	0.16	0.26	This work

hardnesses of the titled compounds are low. Because of this, all $CsMI_3$ compounds show signs of being soft and flexible, which qualify them for thin-film fabrication. The cutting capacity of a compound, the maximum financial level of machine operation, and plastic strain—which are essential for industrial applications—are represented by the machinability factor of the materials under investigation, which is calculated by the formula $U_M = B/C_{44}$ [70]. With the exception of $CsMgI_3$, which indicates better lubricating characteristics and lower frictions and has important applications in a variety of industries, all U_M values are more than 2. In addition, failure mode research—that is, determining whether a material is brittle or ductile—is crucial for technology. The Pugh's ratio (B/G) value indicates if a material is ductile (> 0.75) or brittle (< 0.75) [71]. Table 1 displays all titled compounds as ductile materials, with the exception of $CsMgI_3$, which is characterized as being near the ductile–brittle transition line. Frantsevich et al., however, also suggested a critical value of Poisson's ratio (ν ~0.26) for distinguishing between the brittle and ductile nature of solids [72], as illustrated in Fig. 4.

The calculated values of ν (Fig. 4) again confirm that the $CsMI_3$ compounds are purely ductile except $CsMgI_3$ because of its position below the ductile-brittle transition line. However, the Cauchy pressure, defined as $C_{12} - C_{44}$, is another indicator of failure mode of materials [73]. If the Cauchy pressure is negative, then the material is expected to be brittle; otherwise (having a positive Cauchy pressure), it is a ductile one [73]. Hence, in this study, all $CsMI_3$ compounds are assumed to be ductile in accordance with the aforementioned three indicators. The Kleinman parameter (ξ) measures the ease of bond bending to bond stretching. In general, the value of ξ can be between 0 and 1 ($0 \le \xi \le 1$) and is estimated using the following expression [74]:

$$\xi = \frac{C_{11+8C_{12}}}{7C_{11} + 2C_{12}} \quad (2)$$

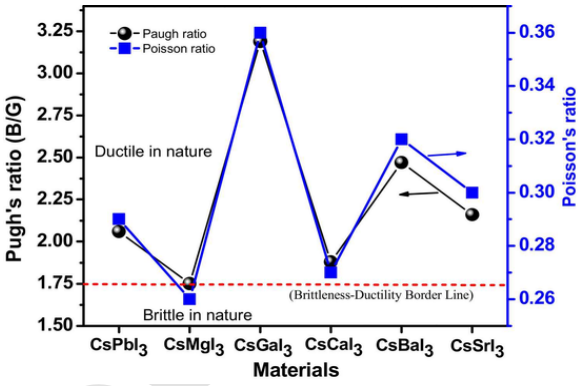

Fig. 4. : Pugh's and Poisson's ratio of the perovskites and the horizontal red dashed line distinguish the brittle and ductile materials.

Kleinman reported that the upper limit corresponds to minimize the bond bending term, and the lower limit corresponds to a minimized bond stretching term [75]. The calculated values of ξ for $CsMI_3$ compounds are shown in Table 1. The estimated value of ξ of ~0.50 for $CsMI_3$ compounds is in good agreement with the previously reported value of ξ of ~0.55 for perovskite $LaAlO_3$ [76]. The calculated value of ξ suggests the strong bonding nature of $CsMI_3$, which is dominated by both bond bending and bond stretching contributions.

The values of C_{44} are related to shear anisotropy factor (Zener ratio) A, that is defined by the following formula [80]

$$A = \frac{G}{Y/[2(1+\nu)]} = \frac{2C_{44}}{C_{11} - C_{12}}$$

The value of A, as illustrated in Table 1, designates the anisotropic nature of the compounds with the possibility of deformation and the appearance of microcracks. The value of A is unity for completely isotropic material, and any deviation from unity (smaller or greater) denotes the degree of anisotropy. The computed values of A (Table 1) indicate the anisotropic nature of the compounds under study.

3.4. Electronic properties

3.4.1. Electronic band structures

The electronic band structure of the compounds provides insight into the electrical characteristics of solids. The electronic band structure of the $CsPbI_3$ compound has been initially estimated under PBE, PBE + spin-orbit coupling (SOC), HSE06, HSE06 + SOC level of theories and the results are shown in Fig. 5. From Fig. 5, all the level of theories shows direct band gap at high-symmetry point R for the $CsPbI_3$ system. The band gap values of the compound, as attained from PBE, PBE + SOC, HSE06 and HSE06 + SOC level of theories, are estimated to be ~ 1.48, 0.24, 1.76 and 0.49 eV respectively. Interestingly, the band gap value of $CsPbI_3$, so obtained from the HSE06 functional without inclusion of SOC, very closely matches with the experimental band gap (~ 1.73 eV, [36]) and another theoretical result as reported elsewhere [36,81]. Although, the inclusion of SOC is found to underestimate the band gap of the studied compound, the band gaps, so estimated from PBE + SOC and HSE06 + SOC level of theory, closely match with the available theoretical results as reported elsewhere [81,82]. So for the present case, the HSE06 functional can be considered here as the most effective level of theory which can closely reproduce the band gap of $CsPbI_3$ compound in agreement with the experimental results. Nonetheless, when comparing the band structure computed using the PBE and HSE06 approaches (Fig. 5, 6), we see that they are quite similar. HSE06 determines the band gap close to the experimental value, in line with earlier research results; however, PBE underestimates the band gap. Ac-

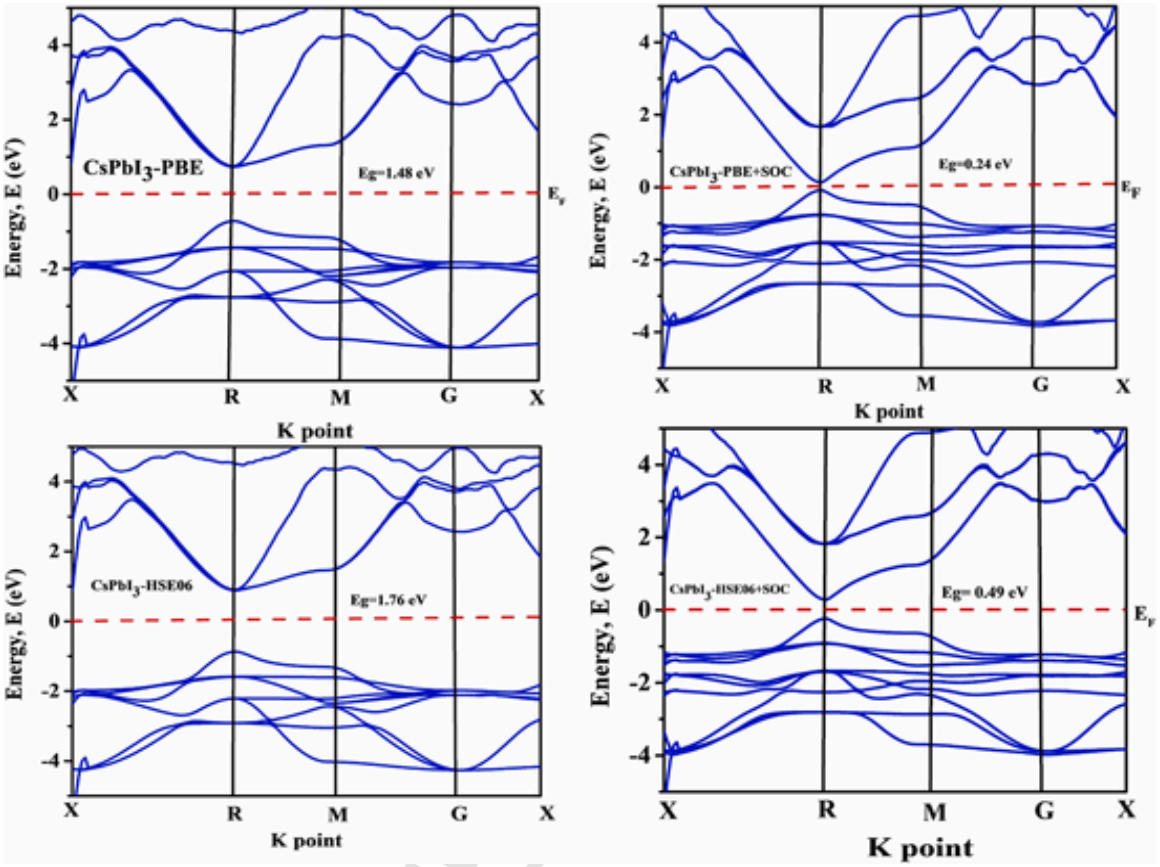

Fig. 5. : Electronic band structures of perovskites $CsPbI_3$ as obtained from PBE, PBE + SOC, HSE06 and HSE06 + SOC level of theories [The zero-energy level in Fig. 5 (a-f) is selected to be the Fermi energy, E_F].

cording to the literature, PBE calculates attributes that are more precise and require less time to complete [81,83,84]. As a result, the PBE computation serves as the foundation for all of the subsequent research in this study.

Thus, the electronic band structures of other perovskites $CsMI_3$ (M = Mg, Ga, Ca, Ba, Sr) have also been computed using the HSE06 functionals. The results are illustrated in Fig. 6(b-f) and Table 2. From Fig. 5, 6 and Table 2, it is observed that the HSE06 functional suggests $CsMI_3$ (M = Pb, Mg, Ga) systems as important materials for photovoltaic applications. The results provide a theoretical reference for future experiments. In addition, the band structures of $CsMI_3$ (M = Mg, Ga, Ca, Ba, Sr) computed using PBE functional are illustrated in supplementary Fig. 2.

Moreover, a tuneable lattice parameter is shown in supplementary Fig. 3, and an exception is noted when Pb is substituted by Mg, Ga, Ca, Ba, or Sr. The HSE06 electronic band structures [Fig. 6] of $CsPbI_3$ and $CsGaI_3$ compounds show direct band gaps at the R and M points of the Brillouin zone, and the remaining $CsMgI_3$, $CsBaI_3$, $CsCaI_3$, and $CsSrI_3$ have illustrated indirect band gaps. The high symmetry paths of *k*-points in the Brillouin zone are selected as X-R-M-G-R. It is noted that thinner devices are possible because photovoltaic materials with direct band gaps absorb light more easily than those with indirect gap. However, compared to indirect bandgap materials, direct bands also experience greater rates of radiative recombination. Therefore, optimizing the absorption properties along with the direct or indirect nature and suppression of radiative recombination of material is important for solar cell applications as absorbance or active materials [85]. Interestingly, Fig. 5 and 6 depict that some of the E_g is in the suitable range as well as visible spectrum range (1.63–3.26 eV) for the absorbance materials in solar cell applications.

3.4.2. *Density of states (DOS)*

The partial density of states (PDOS), total density of states (DOS), and atomic contributions to the band formation of $CsMI_3$ compounds have all been computed for a better understanding. The DOS of the remaining $CsMI_3$ compounds are in the supplemental materials; they are represented in Fig. 7(a,b), where they are almost identical. Fig. 7(a, b) and supplementary Fig. 4 shows that for the compounds from left to right, the total DOS below the E_F increases. Conversely, this value decreases for the compounds in ascending order. It implies that when Pb is replaced by Mg, Ga, Ca, Ba, and Sr, the opposite pattern is shown. Furthermore, the p-orbital of the halogen atom is the primary source of the total DOS below the E_F. Furthermore, Pb-*6p*, Mg-*2p*, Ga-*4p*, Ca-*3p*, Ba-*5p*, and Sr-*4p* electronic states were the major contributors from the p-orbital of M atoms to the total DOS below the E_F. Although the compounds under study are semiconductors by nature (Fig. 5), it appears that there is a value of DOS at the E_F [Fig. 7(a,b)]. The E_F is thought to be at 0 eV in DFT; however, due to calculation errors and a very little shift to the left side (valence band edge) rather than the right side (conduction band), it appears that there is a DOS at the E_F.

3.5. *Optical properties*

3.5.1. *Absorption coefficient*

An essential optical constant that sheds light on how a substance absorbs light over a specific distance is the absorption coefficient [87]. The absorption behavior is contingent upon several elements, including

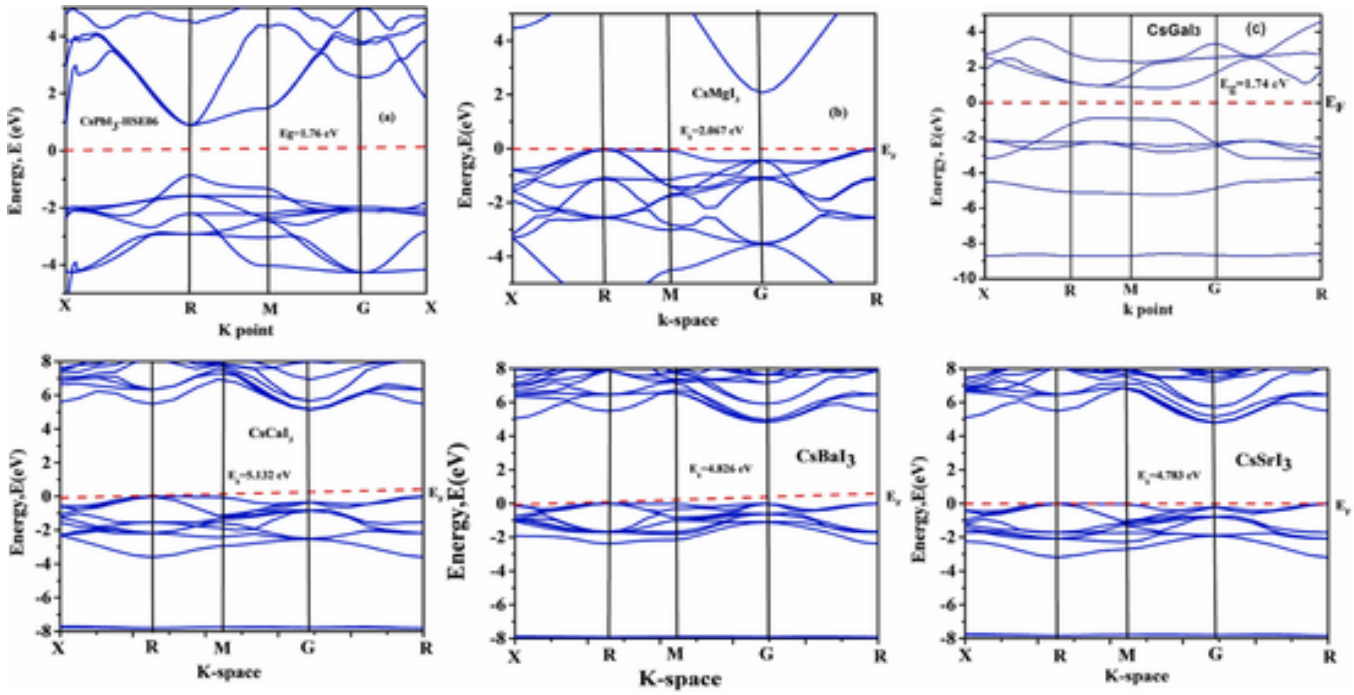

Fig. 6. (a-f): Electronic band structures of perovskites $CsMI_3$ (M = Pb, Mg, Ga, Ca, Ba, Sr) as obtained from HSE06 functional. [The zero-energy level is selected to be the Fermi energy, E_F].

Table 2
Band gaps of the $CsMI_3$ (M = Pb, Mg, Ga, Ca, Ba, Sr) compounds as estimated using HSE06 functional.

Compounds Name	Band Gap (eV) (GGA-PBE)	Band Gap (eV) (HSE06)	Experimental value Band Gap (eV)
$CsPbI_3$	1.48	1.760	1.73 [36]
$CsMgI_3$	1.12	2.067	1.70 [86]
$CsGaI_3$	0	1.740	-
$CsCaI_3$	2.30	5.132	-
$CsBaI_3$	3.514	4.826	-
$CsSrI_3$	3.62	4.783	-

the molecular structure and band gap of the crystal. Specifically, optical absorption occurs when photon frequency entering the material is equal to the frequency of electronic transition in the material. Materials may selectively absorb photons at particular frequencies due to the variation in the absorption coefficient with frequency. Electronic transitions within the full states of the highest valence band and the empty states of the lowest conduction band are what cause the selective behavior. Efficiency in conversion is provided by the materials' absorption of photons. The absorption coefficient α(ω) may be computed using the subsequent formula:

$$\alpha(\omega) = \left[\sqrt{\varepsilon_1{}^2(\omega) + \varepsilon_2{}^2(\omega)} - \varepsilon_1(\omega)\right]^{\frac{1}{2}}$$

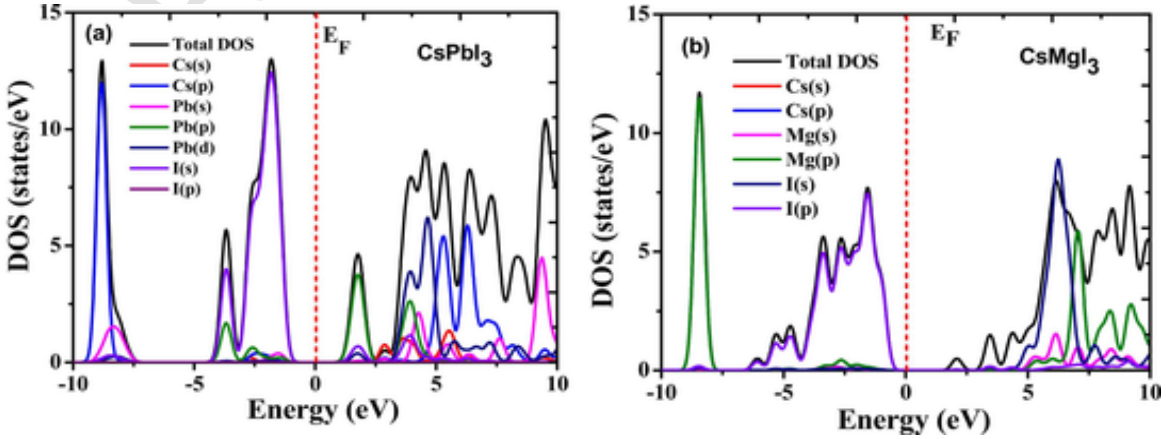

Fig. 7. : Total and partial densities of states of perovskites $CsPbI_3$ (a) and $CsMgI_3$ (b) as estimated from HSE06 functional. [Zero energy corresponds to Fermi energy level (E_F)].

Moreover, the optical properties of crystalline solids can be described by the complex dielectric function, $\varepsilon(\omega) = \varepsilon_1(\omega) + i\varepsilon_2(\omega)$; where $\varepsilon_1(\omega)$ and $\varepsilon_2(\omega)$ are the real and imaginary parts of the dielectric function, respectively (in section 6.3).

Fig. 8(a) displays the absorption coefficient with photon energy. In addition to explaining how incident light is absorbed by a material, the $\alpha(\omega)$ also clarifies how emergent light decays through the medium, providing information on the attenuation of electromagnetic radiation [88,89]. It also provides information on the ideal solar energy conversion efficiency, which is crucial for the practical use of a material in solar cells. Additionally, for the compounds $CsPbI_3$, $CsMgI_3$, $CsCaI_3$, $CsBaI_3$, and $CsSrI_3$, the value of $\alpha(\omega)$ is zero at 0 eV, but it is non-zero for $CsGaI_3$. Because all of the light will pass through zero absorbance substances (at 0 eV), they will be optically transparent in the areas where there is no light absorption. Of the five compounds that might be substituted for the Pb, $CsGaI_3$ and $CsMgI_3$ exhibit absorbance in the visible range, with a value of 3.4 $\times 10^4$ cm^{-1} and 7 $\times 10^3$ cm^{-1} at 2.6 and 2.36 eV, respectively.

3.5.2. Refractive index

The propagation of an electromagnetic beam or light through a compound may be explained from the behavior of $N(\omega) = n(\omega) + ik(\omega)$, where $n(\omega)$ represents the real refractive index and $k(\omega)$ is the extinction coefficient. For each compound, the $n(\omega)$ curve is shown in Fig. 8 (b). It provides further details on how much incident light is bent or refracted as it travels through a material medium [89,90]. At 1.55 eV, the refractive indices for $CsPbI_3$, $CsMgI_3$, $CsGaI_3$, $CsCaI_3$, $CsBaI_3$, and $CsSrI_3$ are 2.3, 2.2, 2.6, 1.3, 1.8, and 1.9, respectively. The $n(\omega)$ values begin to decrease after the peak positions, suggesting less interaction with the photons. Additionally, it is evident that the $n(\omega)$ curve and the $\varepsilon_1(0)$ spectra have similar natures due to their strong correlation, as shown by the formula $n(0) = \sqrt{\varepsilon_1(0)}$ [88].

3.5.3. Real and imaginary part of dielectric function

The optical properties of crystalline solids can be described by the complex dielectric function, $\varepsilon(\omega) = \varepsilon_1(\omega) + i\varepsilon_2(\omega)$; where $\varepsilon_1(\omega)$ and $\varepsilon_2(\omega)$ are the real and imaginary part of the dielectric function, respectively. The imaginary part of the dielectric function is essential to calculate other optical constants [91]. The imaginary part of the dielectric function can be calculated from the momentum matrix elements related to the occupied and unoccupied wave functions in accordance with the selection rules [92] and can be represented as:

$$\varepsilon 2(\omega) = \frac{2\pi e^2}{\Omega \varepsilon_0} \sum_{v,c,k} |\langle \psi_k^c | u.r | \psi_k^v \rangle|^2 \delta\left(E_k^c - E_k^v - E\right) \quad (4)$$

In the above formula, ω is the phonon frequency, e is the electronic charge, Ω is the volume of a unit cell, $\boldsymbol{u}$ is the unit vector along the polarization of the incident electric field and ψ_k^c and ψ_k^v are respective wave functions for conduction and valence band electrons at a particular k. The imaginary part of the dielectric function may be used to de-

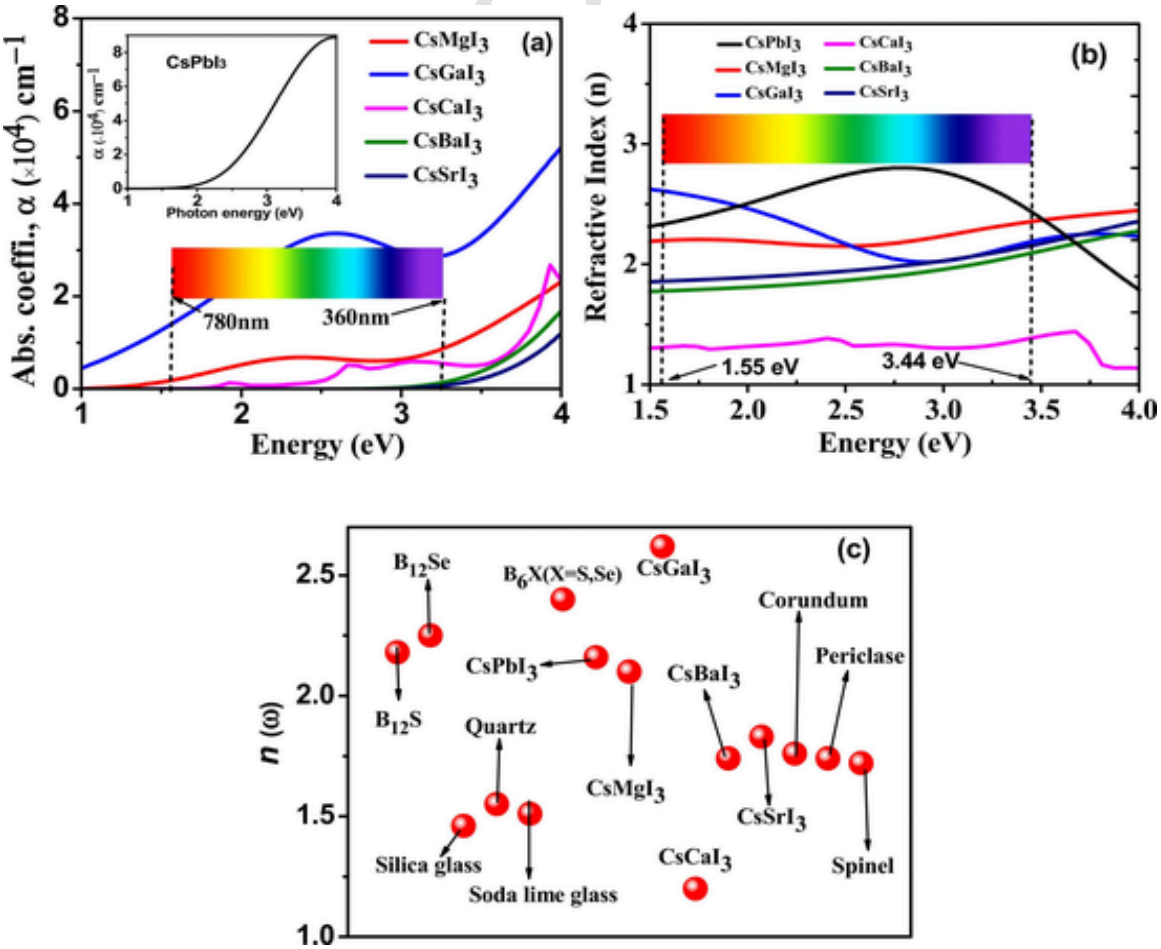

Fig. 8. : Photon energy dependent absorption (a) and refractive index (b) of the $CsMI_3$ perovskite. (c) Comparison of the static refractive index, n at 1.55 eV of $CsMI_3$, with some other well-known ceramic and optical waveguide materials [The photon energy scale in Fig. (a) is set to 1–4 eV to closely observe the absorption coefficient and refractive index in the visible region ranging from 1.55 to 3.44 eV].

duce the real part using the Kramers-Kronig relations. These real and imaginary parts of the dielectric functions $\varepsilon_1(\omega)$ and $\varepsilon_2(\omega)$ can be used to obtain the other remaining optical functions, which include the refractive index n(ω), extinction coefficient *k*(ω), absorption coefficient α (ω), energy-loss function L(ω), optical conductivity σ(ω), and reflectivity R(ω), as described in the literature [56]. Fig. 9(a,b) displays the computed real $\varepsilon_1(\omega)$ and imaginary components $\varepsilon_2(\omega)$ of the dielectric functions of six metal halide perovskites [M = Pb, Mg, Ga, Ca, Ba, and Sr]. The position of the real component of the dielectric function's peak is related to electron excitation in this study, and interband transitions are the main source of the peak. It is generally known that for metallic systems, intraband changes from the conduction electrons, particularly in the low-energy infrared region, dominate the real component of the dielectric function. However, due to the semiconductor character of $CsMI_3$ in the current work, interband transitions determine the dielectric function. The real component of dielectric function $\varepsilon_1(\omega)$ for $CsPbI_3$, $CsMgI_3$, and $CsGaI_3$ compounds exhibits two peaks and a shoulder in Fig. 9(a), while compounds for $CsCaI_3$, $CsBaI_3$, and $CsSrI_3$ compounds show one peak and a shoulder. For $CsGaI_3$, $CsPbI_3$, $CsMgI_3$, $CsCaI_3$, $CsSrI_3$, and $CsBaI_3$, the static real dielectric constant values [at zero energy or $\varepsilon_1(0)$] are 6.8, 4.8, 4.4, 3.7, 3.4, and 3 correspondingly. The ε_1 (ω) values for $CsMgI_3$, $CsCaI_3$, $CsSrI_3$, and $CsBaI_3$ are nearly constant in the visible range (1.58–3.26 eV), as can be seen in the figure. The largest $\varepsilon_1(\omega)$ value for $CsMgI_3$ is 6.25 and happens at 5 eV, whereas the maximum value for $CsPbI_3$ is 7.6 and happens at 2.5 eV. In the higher energy range, $\varepsilon_1(\omega)$ gradually decreases after reaching its apex. Additionally, it turns negative for all of the perovskites at around 9 eV, indicating that they resist strong plasmonic stimulation and behave like metals in this area. The imaginary dielectric function [Fig. 9(b)] provides insight into the state transitions that occur from occupied VB to empty CB [89,90]. Furthermore, the UV regime is where the highest values and a few additional lesser peaks are also reached. The peaks of $\varepsilon_2(\omega)$ seen at those specific energy levels can be attributed to the interband electronic transitions from the valence to conduction bands. In the high energy (more than 16 eV) region, the imaginary part of the dielectric function approaches zero. Conversely, as the dielectric function's real part approaches unity at high energies, it indicates that the materials become transparent and absorb relatively little high-energy input photons.

3.5.4. *Optical conductivity and loss function*

The plot of the compounds' optical conductivity, σ(ω), is depicted in Fig. 10(a), and it closely matches the spectra of $\varepsilon_2(\omega)$ and α(ω). The conductance by the compounds produced during optical stimulation brought on by incident photons of electromagnetic radiation is shown by optical conductivity. For $CsPbI_3$, $CsMgI_3$, $CsGaI_3$, and $CsCaI_3$, $CsBaI_3$, and $CsSrI_3$, respectively, the σ(ω) values are also zero until about 1.5 eV, 1.2 eV, 0 eV, and more than 3 eV, after which they rise to

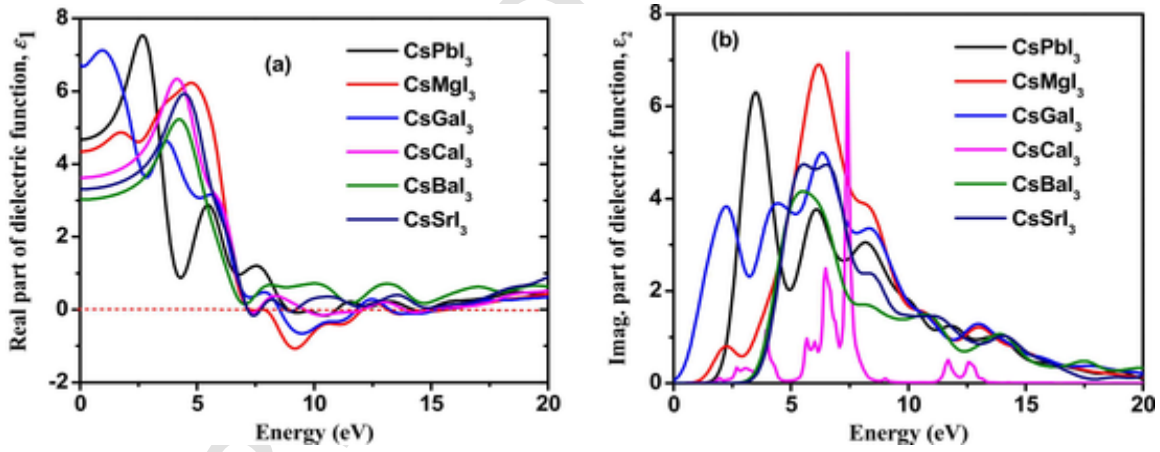

Fig. 9. : Calculated real part (a) and imaginary part (b) of the dielectric function of perovskites $CsMI_3$ (M = Pb, Mg, Ga, Ca, Ba, Sr).

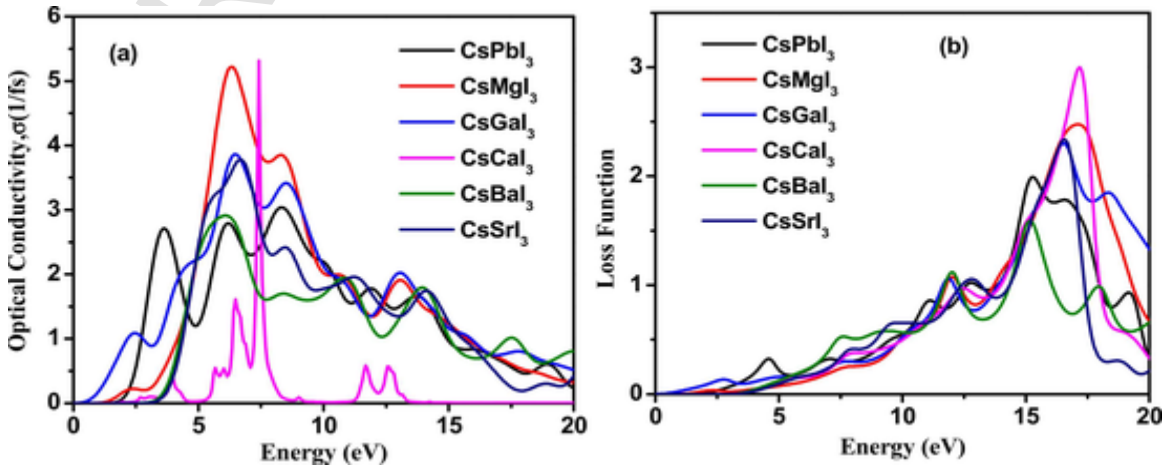

Fig. 10. : Calculated optical conductivity (a) and energy loss function (b) of perovskites $CsMI_3$ (M = Pb, Mg, Ga, Ca, Ba, Sr).

greater levels. Since zero σ (ω) denotes the lack of optical excitations, it may be explained that there is little interaction between the compound's electrons and photons from the incident EM beam within that photon energy range. In the UV range, it reaches its maximal values for $CsMgI_3$ at 9 eV and for $CsPbI_3$ at 4 eV. In addition to these highest peaks, there are other notable peaks that are limited to the ultraviolet region. The results indicate that the majority of the compounds under consideration exhibit strong conductivity and high absorption in the energy range of 4–16 eV, with a peak seen at around 4 eV. Additionally, it is found that, in comparison to Pb-based compounds, Mg-based compounds yield the highest levels of photoconductivity and photon absorption. It is also evident from the conductivity at zero photon energy that the compounds are semiconducting by nature.

Fig. 10(b) shows the plot of electron energy loss spectra, or EELS [L(ω)]. It explains how an incoming electromagnetic beam might cause a compound's electrons to lose energy. In reality, electronic excitations cause energy loss; the L(ω) spectra provide information on these plasmonic excitations [93]. The UV region, which has the largest peaks for all perovskite compounds, is where the bulk of losses are found, according to the EELS plots.

3.6. Thermodynamic properties

Thermodynamic characteristics, including melting temperature (T_m), Debye temperature (θ_D), minimum thermal conductivity (K_{min}), lattice thermal conductivity (K_{ph}), and Grüneisen parameter (γ), have been examined in order to comprehend the behavior of $CsMI_3$ compounds at high temperatures and pressures. In order to explain several intriguing physical phenomena, including phonons, specific heat, melting temperature, thermal conductivity, etc., θ_D is a crucial characteristic of solids [94]. The following equation [94] may be used to approximate the value of θ_D based on average sound velocity:

$$\Theta_D = \frac{h}{k_B}\left[\frac{3m}{4\pi}\left(\frac{\rho N_A}{M}\right)\right]^{1/3} \nu_m \tag{5}$$

where k_B and h denote the Boltzmann and Planck constants, respectively. ρ is the density, and N_A is Avogadro's number. V, m, and M are the volume of a unit cell, the number of atoms within a unit cell, and molecular weight, respectively. v_m implies the average sound velocity in the crystal, which is calculated using the following equation:

$$V_m = \left[\frac{1}{3}\left(\frac{2}{v_t^3}+\frac{1}{v_l^3}\right)\right]^{-1/3} \tag{6}$$

Here, v_t and v_l denote the transverse and longitudinal sound velocities, respectively. The following expressions can be used to calculate v_l and v_t using the crystal density, ρ, shear modulus, G, and the bulk modulus, B:

$$\nu l = \left(\frac{B+34G}{\rho}\right) \text{and} \nu t = \left[\frac{G}{\rho}\right]^{1/2} \tag{7}$$

The melting temperature, T_m, of the $CsMI_3$ compounds has also been calculated via the following empirical formula using elastic constants, C_{ij} [95]:

$$T_m = \left[553K + \left(\frac{5.91K}{GPa}\right)C_{11}\right] \pm 300K \tag{8}$$

Additionally, thermal conductivity is computed, a crucial quantity that is used to examine a material's ability to transfer heat. It is commonly known that temperature directly affects the minimum thermal conductivity. A material's conductivity steadily increases with temperature and then gradually declines to a limiting value [96]. Although there are other comparable formulas available for predicting the lowest thermal conductivity, the Clarke expression [97] was used in this report's calculation of K_{min}, the minimum thermal conductivity, which has the following definition:

$$K_{min} = k_B \nu_m \left(\left(M/n\rho N_A\right)^{-2/3}\right) \tag{9}$$

Where k_B is the Boltzmann constant, ν_m is the average sound velocity, M is the molecular mass, n is the number of atoms per molecule, and N_A is Avogadro's number.

The lattice thermal conductivity can be used to determine the amount of heat energy transferred by lattice vibrations owing to the temperature gradient in a material (K_{ph}). Slack [98] proposed the following empirical formula to calculate the K_{ph}:

$$Kph = A(\gamma)\frac{M_{av}\Theta_D^3\delta}{\gamma^2 n^{2/3}T} \tag{10}$$

With

$$\gamma = \frac{3(1+\upsilon)}{2(2-3\upsilon)} \text{and} A(\gamma) = \frac{4.85628\times10^7}{2\left(1-\frac{0.514}{\gamma}+\frac{0.228}{\gamma^2}\right)} \tag{11}$$

The average atomic mass per atom in a compound is denoted by M_{av}, the absolute temperature is denoted by T, the number of atoms in a unit cell is represented by n, and the Grüneisen parameter is represented by γ. A function of γ is A(γ). Table 3 displays the values of k_{ph} that are computed at 300 K. A lower value of k_{ph} is obtained because of the smaller Θ_D [99,100]. For the 211 MAX phases, the value of k_{ph} fell between 2.5 (W/mK) and 36 (W/mK). Additionally, Table 3 displays the value of the Grüneisen parameter (γ), which indicates the phonons' anharmonicity. Materials with low γ values indicate that harmonic benefaction is present, and as a result, they have high phonon thermal conductivity [55,59]. The crucial parameter for the materials to employ in the high-temperature zone is the minimum thermal conductivity, K_{min}.

The Grüneisen parameter (γ) provides information regarding anharmonic effects, i.e., the temperature-dependent phonon damping as well as the thermal expansion effects. The Grüneisen parameter can be expressed as:

Table 3
The calculated density, (p), Debye temperature, (Θ_D), longitudinal, transverse, and average sound velocities (V_l, V_t, V_m), minimum thermal conductivity (K_{min}), lattice thermal conductivity (K_{ph}) at 300 K, and melting temperature (T_m) of $CsMI_3$ compounds.

Compound	ρ(Kg/m^3)	V_l (km/s)	V_t (Km/s)	V_m (km/s)	Θ_D (k)	K_{min} (W/m K)	K^*_{ph} (W/m K)	Y	T_m (K)
$CsPbI_3$	9130	1.78	0.97	1.48	109	0.231	0.844	1.71	787
$CsMgI_3$	8572	2.01	0.04	1.80	143	0.327	1.51	1.59	759
$CsGaI_3$	8905	1.52	0.02	1.06	83	0.181	0.162	2.22	726
$CsCaI_3$	7663	1.92	0.03	1.66	126	0.276	1.13	1.60	754
$CsBaI_3$	6980	1.59	0.81	1.17	81	0.163	0.266	1.90	719
$CsSrI_3$	7371	1.63	0.87	1.31	95	0.2	0.438	1.77	721

$$\gamma(\omega_n) = \frac{d\ln(\omega_n)}{d\quad(\ln(\Phi)\quad)} \tag{12}$$

where ω_n and Φ are the angular frequency and the packing fraction of crystals, respectively.

The calculated values of Debye temperature, θ_D, along with different sound velocities (v_l, v_t, and v_m), melting temperature, T_m, the Grüneisen parameter, γ, and minimum thermal conductivity, K_{min}, lattice thermal conductivity K_{ph} of $CsMI_3$ under study are listed in Table 3. In general, a higher Debye temperature is associated with a higher phonon thermal conductivity and vice-versa. The relatively low values of, $K_{min,}$ and K_{ph} of $CsMI_3$ imply low thermal conductivity, and they might be suitable for use as thermoelectric devices.

3.6.1. Heat capacities and thermal expansion coefficient

The thermodynamic properties, including heat capacity (Cp, C_V) and thermal expansion coefficient (TEC), have been calculated using the results from phonon dispersion and following the quasi-harmonic approximation. These temperature-dependence properties at zero pressure are calculated using the following equations [101]:

$$F = 3nN_AK_BT\int_0^{\omega_{max}} \ln\left\{2\sinh\left(\frac{\hbar\omega}{2K_BT}\right)\right\} g(\omega)d\omega$$

$$E = 3nN_A\frac{\hbar}{2}\int_0^{\omega_{max}} \omega\coth\left(\frac{\hbar\omega}{2K_BT}\right) g(\omega)d\omega$$

$$S = 3nN_AK_B\int_0^{\omega_{max}} \left[\frac{\hbar\omega}{2K_BT}\coth\left(\frac{\hbar\omega}{2K_BT}\right) - \ln\left\{2\sinh\left(\frac{\hbar\omega}{2K_BT}\right)\right\}\right] g(\omega)d\omega$$

$$C_v = 9nN_AK_B\left(\frac{T}{\theta_D}\right)\int_0^{x_D}\frac{x^4e^x}{(e^x-1)^2} \tag{14}$$

Fig. 11(a, b) displays the predicted values of C_p and C_v in the temperature range of 0–1000 K. Materials may be described using their specific heat under a variety of thermodynamic constraints. Heat capacity provides us with important details about the materials, such as energy band structure, density of state, and lattice vibration. It also describes the material's capacity to retain heat. The concepts of heat capacity at constant pressure (C_p) and heat capacity at constant volume (C_v) are covered here. The phonon contribution dominates C_v and C_p as a function of temperature. The findings show that the specific heat C_v and C_p of $CsMI_3$ match the Debye model [102]. This model provides an accurate prediction of the temperature dependency of the heat capacity at constant volume at low temperatures. $CsMI_3$

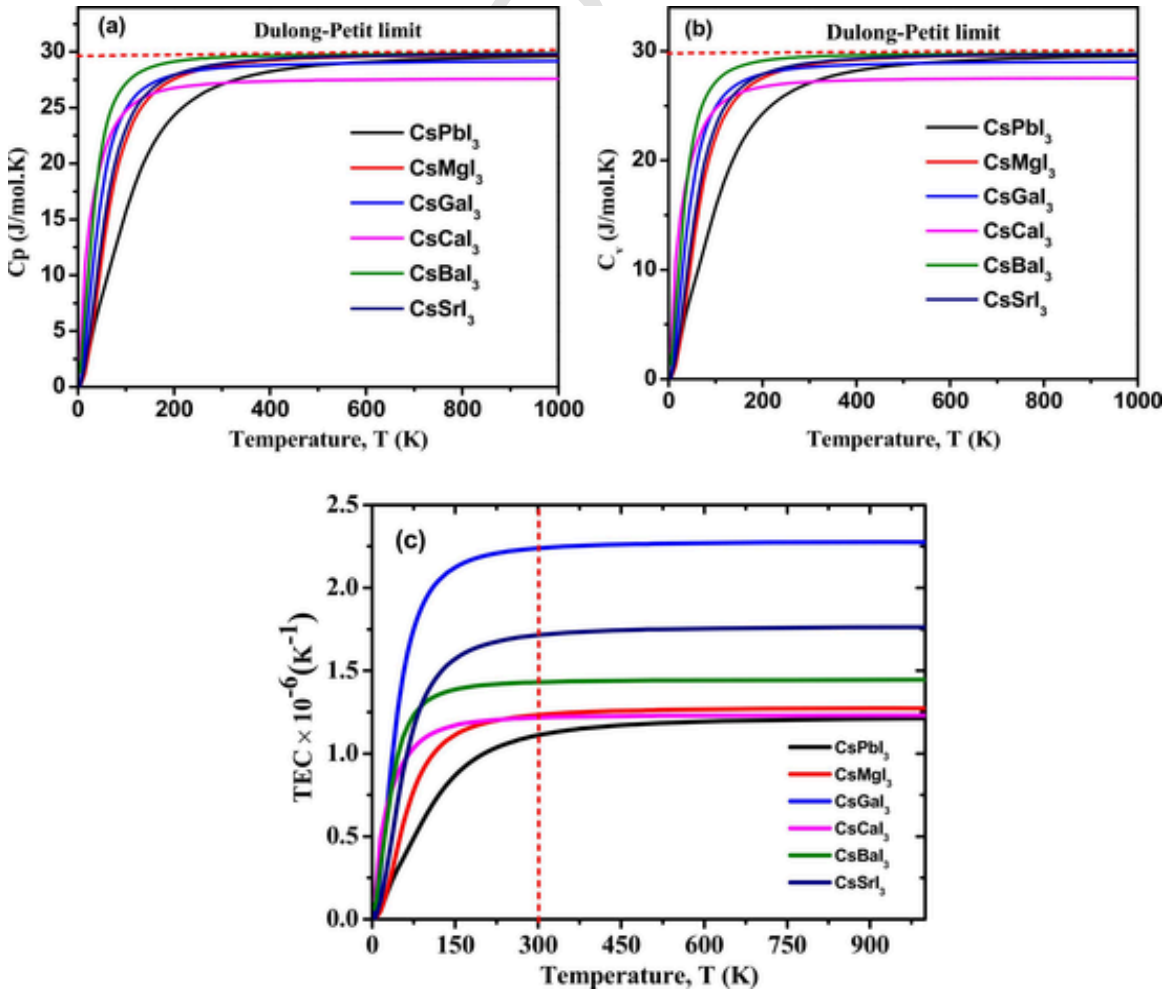

Fig. 11. : Calculated heat capacity at constant pressure, C_p (a) and heat capacity at constant volume, C_v (b), and estimated TEC values (c) of Perovskites $CsMI_3$ (M = Pb, Mg, Ga, Ca, Ba, Sr).

exhibits a considerable increase in heat capacity (C_v and C_p) at temperatures as high as 200 K. Furthermore, it has been discovered that elevated temperatures allow for the reinstatement of the Dulong-Petit law. Scientists are interested in disseminating information about the application at high temperatures. By analyzing the thermal characteristics defining factors like Debye temperature (Θ_D), phonon thermal conductivity (k_{ph}), minimum thermal conductivity (K_{min}), Grüneisen parameter (γ), and melting temperature (T_m), one may comprehend the uses of these materials as thermoelectric power generator. The discrepancy between C_p and C_v is due to the thermal expansion of materials, which is brought on by the anharmonicity in the lattice dynamics.

The thermal expansion coefficient (*TEC*) is calculated by the following equation [103]:

$$\mathrm{TEC} = \frac{\gamma C_v}{3B_T v_m} \tag{15}$$

Where γ = Grüneisen parameter, C_v = specific heat at constant volume, B_T = isothermal bulk modulus, and v_m = molar volume. The variation of TEC with temperature is presented in Fig. 11(c) for the compounds under study. The values are found to be 1.12 × 10^{-6}, 1.24 × 10^{-6}, 2.24 × 10^{-6}, 1.21 × 10^{-6}, 1.44 × 10^{-6}, 1.72× 10^{-6} (with unit K^{-1}) at temperature 300 K for the $CsMI_3$ (M = Pb, Mg, Ga, Ca, Ba, Sr) compounds, respectively. These values are comparable with the reported values for the Ti_2SC 211 MAX phase system [104]. The values of C_p are calculated using $C_p = C_v[1 + \alpha\gamma T]$ and values are found to be26.97, 28.99, 28.49, 27.29, 29.44, and 29.11(with unit J/mol.K) for the $CsMI_3$ (M = Pb, Mg, Ga, Ca, Ba, Sr) compounds at temperature 300 K, respectively [55].

3.7. Lead free perovskites (Supercell of $CsMg(I_{1-x}Br_x)_3$, x= 0–1 in step of 0.25)

The key characteristics of the studied perovskite materials are illustrated in Table 4. It is seen that $CsMgI_3$ has higher absorption coefficient compared to others and it is suitable for optical device application. However, $CsGaI_3$ and $CsCaI_3$ are shown medium absorption, whereas $CsBaI_3$ and $CsSrI_3$ have very low optical absorption, consequently are not suitable to use in especially solar cell device.

Table 4 summarizes the essential characteristics of the metal halide perovskites $CsMI_3$. As can be seen in Fig. 8(a), the $CsGaI_3$ displays high absorbance, using the HSE06 potential, it is proven that E_g = 1.74 eV. Since the $CsGaI_3$ exhibits semiconductor properties, it might be a good choice for solar applications. Consequently, further insight into the $CsGaI_3$ characteristics may be gained. Then, the Mg-based compounds, in contrast to Pb-containing compounds, exhibit high optical absorbance and optical conductivity, indicating that Mg might be a more suitable substitute for lead. However, due to their wide or tunable band gap behavior, all of the metal halide perovskites of $CsCaI_3$, $CsBaI_3$, and $CsSrI_3$ are outside the prescribed band gap (Shockley-Queisser limit for single solar cell) to achieve the highest possible efficiency in solar cells, even though their mechanical properties, which include elastic constants and material tolerance factors like brittleness or ductility, clarify their stability by Born stability criteria. Furthermore, because $CsMgI_3$ has the maximum absorption and photoconductivity in the solar spectrum, It may be assumed that it would be a superior lead-free perovskite material for solar cell application. However, the issue with $CsMgI_3$ is that it remains at the boundary between brittleness and ductility. However, brittleness can be reduced by combining Br and Cl with $CsMgI_3$ in a solid solution [supplementary Fig. 5 (a,b)] [105]. This will increase the likelihood of obtaining a more lead-free, magnesium-based perovskite compound with a better band gap and better optoelectronic characteristics for use in solar cells. The mechanical characteristics and electronic band gap of solid solutions $CsMg(I_{1-x}Br_x)_3$ have been computed in order to identify a ductile lead-free perovskite (supplementary Table-2 and Fig. 6). Fig. 12 shows the Pugh's ratio with Poisson's ratio for various combinations of I and Br. The results show that in $CsMg(I_{1-x}Br_x)_3$, the highest ductility is located at x = 0.25. Furthermore, a visual representation of the band gap value with the lattice parameter for different $CsMg(I_{1-x}Br_x)_3$ combinations is shown in supplementary Fig. 6a. The results indicate that $CsMg(I_{0.75}Br_{0.25})_3$ is more ductile than $CsMgI_3$. Additionally, the material is soft and mechanically stable (Supplementary Table 3), and it can be readily fabricated as a thin film. A supercell of $CsMg(I_{1-x}Br_x)_3$ is produced where x = 0, 0.25, 0.50, 0.75, and 1 in order to better understand absorption and optical conductivity. The electronic band gap of $CsMg(I_{0.75}Br_{0.25})_3$ is determined to be 1.4 eV. For applications that need ductility, the optimum Pb-free perovskite would be $CsMg(I_{0.75}Br_{0.25})_3$. The electronic band gap value is graphically presented with the lattice parameter in supplementary Fig. 6 (a,b), indicating that $CsMg(I_{1-x}Br_x)_3$ is a superior combination.

Table 4
The key properties are summarized to predict perovskites.

Traits	$CsPbI_3$	$CsMgI_3$	$CsGaI_3$	$CsCaI_3$	$CsBaI_3$	$CsSrI_3$
Optical Absorption	Less	High	High	Medium	Less	Less
Photoconductivity	Less	High	Medium	Medium	Less	Less
Ductility	Highly Ductile	Brittle-Ductile Border line	Highly Ductile	Ductile	Highly Ductile	Highly Ductile
Dynamically stable	Yes	Yes	Yes	Yes	Yes	Yes
Reflectivity	High	High	Medium	Less	Less	Less
Formation Energy	Negative	Negative	Negative	Negative	Negative	Negative

3.7.1. Electronic band gap of lead-free perovskites (Supercell of $CsMg(I_{1-x}Br_x)_3$, x = 0, 0.25, 0.50, 0.75, 1)

Despite having acceptable mechanical stability and ductility qualities (supplementary Fig. 5), the $CsMg(I_{0.6}Br_{0.4})_3$ solid solution does not exhibit the optical properties necessary to get a desired band gap value of 1–1.8 eV for use in solar cell applications. To get a deeper knowledge of the electronic band gap and more suitable optoelectronic characteristics, a supercell of 40 $CsMg(I_{1-x}Br_x)_3$ atoms, with x = 0, 0.25, 0.50, 0.75 has been constructed and 1; the structural property section has already covered x-values. 24 I atoms in the $CsMgI_3$ supercell have undergone successive changes to produce the desired mixture of 25 %, 50 %, 75 %, and 100 % Br in the molecule. Fig. 13 displays the predicted mechanical characteristics (supplementary Table-3) and electrical band gap of the supercell $CsMg(I_{1-x}Br_x)_3$, with x = (0, 0.25, 0.50, 0.75, and 1).

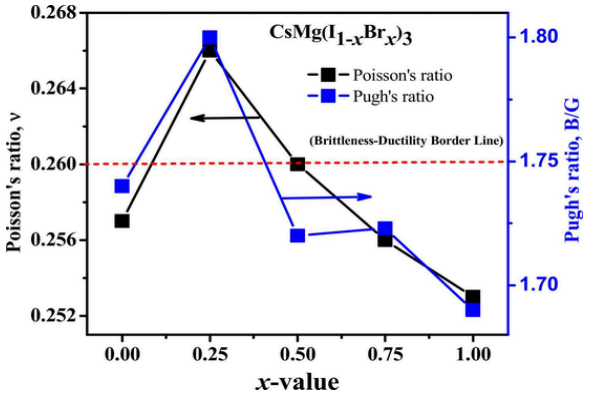

Fig. 12. : Variation of Pugh's ratio with Poisson's ratio of the perovskites with different compositions in supercell of $CsMg(I_{1-x}Br_x)_3$. The red dashed line separates the ductile materials from the brittle.

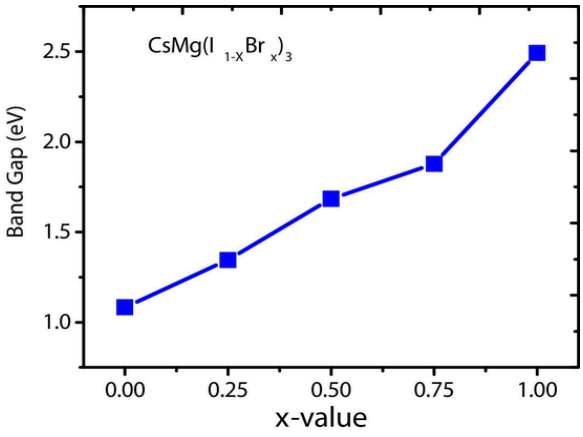

Fig. 13. : Variations of band gap of the perovskites with different composition [$CsMg(I_{1-x}Br_x)_3$ supercell].

According to the findings (Supplementary Table 3), the $CsMg(I_{0.75}Br_{0.25})_3$ compound is more ductile than the $CsMgI_3$ material. It is also soft and mechanically stable, making it easy to form into thin films. Supplementary Table 3 indicates that these composite compounds exhibit a modest phase change from cubic to triclinic, as well as 21 positive stiffness constants that all fulfill stability requirements. It is discovered that CsMg $(I_{0.75}Br_{0.25})_3$ has a band gap of 1.35 eV and favorable optical characteristics, indicating that it is a favorable candidate for lead-free perovskite. However, the $CsMg(I_{1-x}Br_x)_3$ compound exhibits an expected band gap of 1.87 eV for $x = 0.50$ and 0.75. However, the Shockley-Queisser limit indicates that a reasonable band gap for a single solar cell is 1.4.

For considered lead-free perovskite compounds $CsMg(I_{1-x}Br_x)_3$, where $x = 0, 0.25, 0.75, 0.50, 1$, the detailed optical properties, including the real and imaginary parts of dielectric functions, refractive index, extinction coefficient, absorption spectra, reflectivity, and photoconductivity, are investigated up to the photon energy of 20 eV to reveal the response of the materials in solar and high energy radiation [Supplementary Fig. 7 (a-e)]. The amount of light at a given wavelength (energy) that enters a material before it is absorbed is measured by the substance's optical absorption coefficient [104]. Additionally, it provides details on the ideal solar energy conversion efficiency, which is crucial for a material's actual use in solar cells. Fig. 14(a) shows the computed optical absorption spectra of the compounds under consideration for the visible range. Its values are nearly identical to the bare $CsMgI_3$, and it varies greatly in the visible range.

The calculated refractive index, n, is shown in Fig. 14 (b), where n can be varied from 2.10 – 2.24 in the range of visible range for $x = 0.25$. It is consistent with its bare $CsMgI_3$ compound that is comparable with its commercially available counterpart (Fig. 8c). The remaining optical properties of the supercell, i.e., dialectic constant, conductivity, and loss function, have been represented in the supplementary section. All these findings reveal that $CsMg(I_{0.75}Br_{0.25})$ is a better replacement for lead-free perovskite for solar cell applications.

4. Conclusions

First-principles DFT calculations have been performed to investigate the structural, electronic, optical, mechanical, and thermodynamic properties of Pb-free inorganic metal halide cubic perovskites $CsMI_3$ (M = Mg, Ga, Ca, Ba, Sr). These compounds have been compared with the Pb-based compounds. The negative formation energy, all positive frequencies in the phonon dispersion curve, and fulfillment of stability conditions by elastic constants confirmed the chemical and structural stability of the compounds. This study suggests that the electronic band gap value and other physical properties are affected by the replacement of the M= (Mg, Ga, Ca, Ba, Sr) atoms in place of Pb atom of $CsMI_3$ compound. These are the key features of the materials to be used in the solar cell and optoelectronic devices. The investigated perovskite compounds are mechanically stable and can easily be developed into thin films as the materials have low bulk modulus. According to the optical properties as well as electronic properties analysis, the Mg atom appears superior to Pb for the considered inorganic perovskites, as Mg-based compounds $CsMgI_3$ have higher optical absorption and optical conductivity than the Pb-based compounds, specially the composition $CsMg(I_{0.75}Br_{0.25})$ is suitable for the use as absorbing material in the solar cell. However, the $CsMgI_3$ is slightly brittle and may not be superior in applications that require ductility. Finally, supercell $CsMg(I_{0.75}Br_{0.25})_3$ proves its proper capability in mechanical, electronic, and optical fields so that results favor the better replacement of lead-free perovskite.

Funding

Research grant was sponsored by The World Academy of Sciences (TWAS). Grant No. RGA No. 21–378 RG/PHYS/AS_ FR3240319526.

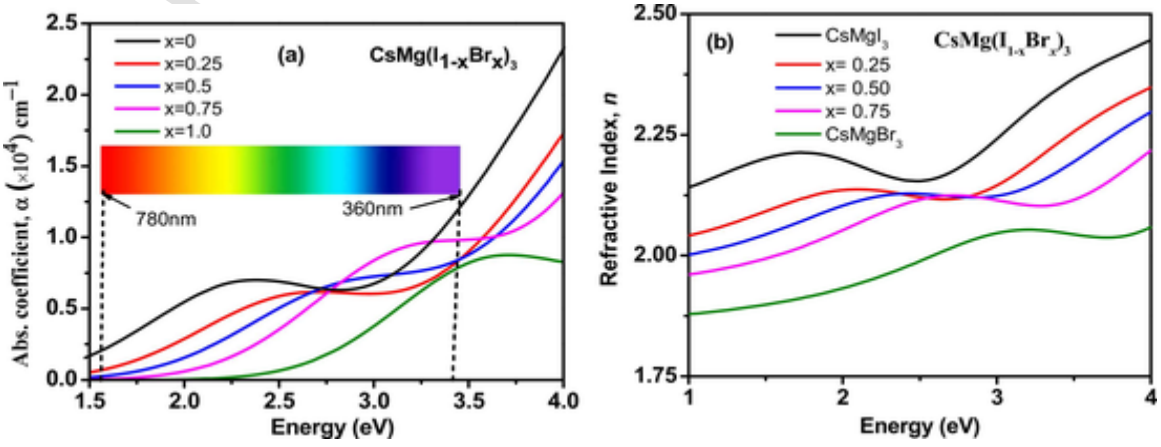

Fig. 14. : (a) Variations of absorption coefficient as a function of photon energy (b) refractive index for different compositions of $CsMg(I_{1-x}Br_x)_3$ supercell.

CRediT authorship contribution statement

J. Chowdhury: Writing – review & editing. **Uddin Md Mohi Uddin:** Writing – review & editing, Supervision, Software, Data curation. **M. A. Ali:** Writing – review & editing. **M. M. Hossain:** Writing – review & editing. **S. H. Naqib:** Writing – review & editing. **S. Ghosh:** Writing – review & editing, Data curation. **M. Biswas:** Writing – original draft, Software, Methodology, Data curation, Conceptualization.

Declaration of Competing Interest

Authors declare no financial interest.

Data Availability

Data will be made available on request.

Acknowledgements

This work was carried out with the aid of a grant (grant number: 21–378 RG/PHYS/AS_G -FR3240319526) from UNESCO-TWAS and the Swedish International Development Cooperation Agency (SIDA). The views expressed herein do not necessarily represent those of UNESCO-TWAS, SIDA or its Board of Governors. S. Ghosh and J. Chowdhury sincerely acknowledge the Bioinformatics Resources and Applications Facility (BRAF), C-DAC, Pune for availing the computational resources. S. Ghosh also expresses his thanks to the University Grants Commission, Government of India for providing the UGC-NET (JRF) award in form of senior research fellowship.

Appendix A. Supporting information

Supplementary data associated with this article can be found in the online version at doi:10.1016/j.mtcomm.2024.109422.

References

[1] Q.A. Akkerman, M. Gandini, F. Di Stasio, P. Rastogi, F. Palazon, G. Bertoni, J.M. Ball, M. Prato, A. Petrozza, L. Manna, Strongly emissive perovskite nanocrystal inks for high-voltage solar cells, Nat. Energy 2 (2016) 16194, https://doi.org/10.1038/nenergy.2016.194.

[2] Z. Ni, H. Jiao, C. Fei, H. Gu, S. Xu, Z. Yu, G. Yang, Y. Deng, Q. Jiang, Y. Liu, Y. Yan, J. Huang, Evolution of defects during the degradation of metal halide perovskite solar cells under reverse bias and illumination, Nat. Energy 7 (2022) 65–73, https://doi.org/10.1038/s41560-021-00949-9.

[3] W. Zhang, G.E. Eperon, H.J. Snaith, Metal halide perovskites for energy applications, Nat. Energy 1 (2016), https://doi.org/10.1038/nenergy.2016.48.

[4] P. Ramasamy, D.H. Lim, B. Kim, S.H. Lee, M.S. Lee, J.S. Lee, All-inorganic cesium lead halide perovskite nanocrystals for photodetector applications, Chem. Commun. 52 (2016) 2067–2070, https://doi.org/10.1039/c5cc08643d.

[5] A. Swarnkar, A.R. Marshall, E.M. Sanehira, B.D. Chernomordik, D.T. Moore, J.A. Christians, T. Chakrabarti, J.M. Luther, Quantum dot–induced phase stabilization of α-CsPbI3 perovskite for high-efficiency photovoltaics, Science 354 (2016) 92–95, https://doi.org/10.1126/science.aag2700.

[6] W.J. Yin, T. Shi, Y. Yan, Unique properties of halide perovskites as possible origins of the superior solar cell performance, Adv. Mater. 26 (2014) 4653–4658, https://doi.org/10.1002/adma.201306281.

[7] K.P. Marshall, M. Walker, R.I. Walton, R.A. Hatton, Enhanced stability and efficiency in hole-transport-layer-free CsSnI3 perovskite photovoltaics, Nat. Energy 1 (2016) 16178, https://doi.org/10.1038/nenergy.2016.178.

[8] R.J. Sutton, G.E. Eperon, L. Miranda, E.S. Parrott, B.A. Kamino, J.B. Patel, M.T. Hörantner, M.B. Johnston, A.A. Haghighirad, D.T. Moore, H.J. Snaith, Bandgap-Tunable Cesium Lead Halide Perovskites with High Thermal Stability for Efficient Solar Cells, Adv. Energy Mater. 6 (2016) 1502458, https://doi.org/10.1002/aenm.201502458.

[9] J.B. Hoffman, A.L. Schleper, P.V. Kamat, Transformation of Sintered CsPbBr3 Nanocrystals to Cubic CsPbI3 and Gradient CsPbBrxI3-x through Halide Exchange, J. Am. Chem. Soc. 138 (2016) 8603–8611, https://doi.org/10.1021/jacs.6b04661.

[10] L. Huang, W.R.L. Lambrecht, Electronic band structure trends of perovskite halides: Beyond Pb and Sn to Ge and Si, Phys. Rev. B. 93 (2016) 195211, https://doi.org/10.1103/PhysRevB.93.195211.

[11] G.E. Eperon, G.M. Paternò, R.J. Sutton, A. Zampetti, A.A. Haghighirad, F. Cacialli, H.J. Snaith, Inorganic caesium lead iodide perovskite solar cells, J. Mater. Chem. A. 3 (2015) 19688–19695, https://doi.org/10.1039/C5TA06398A.

[12] T. Krishnamoorthy, H. Ding, C. Yan, W.L. Leong, T. Baikie, Z. Zhang, M. Sherburne, S. Li, M. Asta, N. Mathews, S.G. Mhaisalkar, Lead-free germanium iodide perovskite materials for photovoltaic applications, J. Mater. Chem. A 3 (2015) 23829–23832, https://doi.org/10.1039/c5ta05741h.

[13] Best research-cell efciency chart. NREL, (n.d.). ⟨https://www.nrel.gov/pv/cellefciency.html⟩ (2021).

[14] M.M. Lee, J. Teuscher, T. Miyasaka, T.N. Murakami, H.J. Snaith, Efficient Hybrid Solar Cells Based on Meso-Superstructured Organometal Halide Perovskites, Science 338 (2012) 643–647, https://doi.org/10.1126/science.1228604.

[15] D.P. McMeekin, G. Sadoughi, W. Rehman, G.E. Eperon, M. Saliba, M.T. Hörantner, A. Haghighirad, N. Sakai, L. Korte, B. Rech, M.B. Johnston, L.M. Herz, H.J. Snaith, A mixed-cation lead mixed-halide perovskite absorber for tandem solar cells, Science 351 (2016) 151–155, https://doi.org/10.1126/science.aad5845.

[16] S. Yang, S. Chen, E. Mosconi, Y. Fang, X. Xiao, C. Wang, Y. Zhou, Z. Yu, J. Zhao, Y. Gao, F. De Angelis, J. Huang, Stabilizing halide perovskite surfaces for solar cell operation with wide-bandgap lead oxysalts, Science 365 (2019) 473–478, https://doi.org/10.1126/science.aax3294.

[17] Y.-H. Lin, N. Sakai, P. Da, J. Wu, H.C. Sansom, A.J. Ramadan, S. Mahesh, J. Liu, R.D.J. Oliver, J. Lim, L. Aspitarte, K. Sharma, P.K. Madhu, A.B. Morales-Vilches, P.K. Nayak, S. Bai, F. Gao, C.R.M. Grovenor, M.B. Johnston, J.G. Labram, J.R. Durrant, J.M. Ball, B. Wenger, B. Stannowski, H.J. Snaith, A piperidinium salt stabilizes efficient metal-halide perovskite solar cells, Science 369 (2020) 96–102, https://doi.org/10.1126/science.aba1628.

[18] W.S. Yang, B.W. Park, E.H. Jung, N.J. Jeon, Y.C. Kim, D.U. Lee, S.S. Shin, J. Seo, E.K. Kim, J.H. Noh, S.Il Seok, Iodide management in formamidinium-lead-halide-based perovskite layers for efficient solar cells, Science 356 (2017) 1376–1379, https://doi.org/10.1126/science.aan2301.

[19] T. Baikie, Y. Fang, J.M. Kadro, M. Schreyer, F. Wei, S.G. Mhaisalkar, M. Graetzel, T.J. White, Synthesis and crystal chemistry of the hybrid perovskite (CH 3NH3)PbI3 for solid-state sensitised solar cell applications, J. Mater. Chem. A 1 (2013) 5628–5641, https://doi.org/10.1039/c3ta10518k.

[20] M.R. Filip, F. Giustino, GW quasiparticle band gap of the hybrid organic-inorganic perovskite CH3NH3PbI3: Effect of spin-orbit interaction, semicore electrons, and self-consistency, Phys. Rev. B - Condens. Matter Mater. Phys. 90 (2014) 1–10, https://doi.org/10.1103/PhysRevB.90.245145.

[21] D. Shi, V. Adinolfi, R. Comin, M. Yuan, E. Alarousu, A. Buin, Y. Chen, S. Hoogland, A. Rothenberger, K. Katsiev, Y. Losovyj, X. Zhang, P.A. Dowben, O.F. Mohammed, E.H. Sargent, O.M. Bakr, Low trap-state density and long carrier diffusion in organolead trihalide perovskite single crystals, Science 347 (2015) 519–522, https://doi.org/10.1126/science.aaa2725.

[22] K. Tvingstedt, O. Malinkiewicz, A. Baumann, C. Deibel, H.J. Snaith, V. Dyakonov, H.J. Bolink, Radiative efficiency of lead iodide based perovskite solar cells, Sci. Rep. 4 (2014) 1–7, https://doi.org/10.1038/srep06071.

[23] G. Xing, N. Mathews, S. Sun, S.S. Lim, Y.M. Lam, M. Grätzel, S. Mhaisalkar, T.C. Sum, Long-range balanced electron- and hole-transport lengths in organic-inorganic CH 3 NH 3 PbI 3, Science 342 (2013) 344–347, https://doi.org/10.1126/science.1243167.

[24] S.D. Stranks, G.E. Eperon, G. Grancini, C. Menelaou, M.J.P. Alcocer, T. Leijtens, L.M. Herz, A. Petrozza, H.J. Snaith, Electron-hole diffusion lengths exceeding 1 micrometer in an organometal trihalide perovskite absorber, Science 342 (2013) 341–344, https://doi.org/10.1126/science.1243982.

[25] M. Grätzel, The light and shade of perovskite solar cells, Nat. Mater. 13 (2014) 838–842, https://doi.org/10.1038/nmat4065.

[26] C. Wehrenfennig, G.E. Eperon, M.B. Johnston, H.J. Snaith, L.M. Herz, High Charge Carrier Mobilities and Lifetimes in Organolead Trihalide Perovskites, Adv. Mater. 26 (2014) 1584–1589, https://doi.org/10.1002/adma.201305172.

[27] C.C. Stoumpos, C.D. Malliakas, M.G. Kanatzidis, Semiconducting tin and lead iodide perovskites with organic cations: phase transitions, high mobilities, and near-infrared photoluminescent properties, Inorg. Chem. 52 (2013) 9019–9038, https://doi.org/10.1021/ic401215x.

[28] A. Babayigit, D. Duy Thanh, A. Ethirajan, J. Manca, M. Muller, H.G. Boyen, B. Conings, Assessing the toxicity of Pb-and Sn-based perovskite solar cells in model organism Danio rerio, Sci. Rep. 6 (2016) 1–11, https://doi.org/10.1038/srep18721.

[29] F. Giustino, H.J. Snaith, Toward Lead-Free Perovskite Solar Cells, ACS Energy Lett. 1 (2016) 1233–1240, https://doi.org/10.1021/acsenergylett.6b00499.

[30] B. Hailegnaw, S. Kirmayer, E. Edri, G. Hodes, D. Cahen, Rain on methylammonium lead iodide based perovskites: Possible environmental effects of perovskite solar cells, J. Phys. Chem. Lett. 6 (2015) 1543–1547, https://doi.org/10.1021/acs.jpclett.5b00504.

[31] R. Wang, J. Wang, S. Tan, Y. Duan, Z.-K. Wang, Y. Yang, Opportunities and Challenges of Lead-Free Perovskite Optoelectronic Devices, Trends Chem. 1 (2019) 368–379, https://doi.org/10.1016/j.trechm.2019.04.004.

[32] F. Hong, B. Saparov, W. Meng, Z. Xiao, D.B. Mitzi, Y. Yan, Viability of lead-free perovskites with mixed chalcogen and halogen anions for photovoltaic applications, J. Phys. Chem. C. 120 (2016) 6435–6441, https://doi.org/10.1021/acs.jpcc.6b00920.

[33] M. Lyu, J.H. Yun, P. Chen, M. Hao, L. Wang, Addressing toxicity of lead: progress and applications of low-toxic metal halide perovskites and their derivatives, Adv. Energy Mater. 7 (2017), https://doi.org/10.1002/aenm.201602512.

[34] Z. Shi, J. Guo, Y. Chen, Q. Li, Y. Pan, H. Zhang, Y. Xia, W. Huang, Lead-Free Organic–Inorganic Hybrid Perovskites for Photovoltaic Applications: Recent Advances and Perspectives, Adv. Mater. 29 (2017), https://doi.org/10.1002/

adma.201605005.
[35] M. Roknuzzaman, K. Ostrikov, H. Wang, A. Du, T. Tesfamichael, Towards lead-free perovskite photovoltaics and optoelectronics by ab-initio simulations, Sci. Rep. 7 (2017) 14025, https://doi.org/10.1038/s41598-017-13172-y.
[36] G.E. Eperon, S.D. Stranks, C. Menelaou, M.B. Johnston, L.M. Herz, H.J. Snaith, Formamidinium lead trihalide: A broadly tunable perovskite for efficient planar heterojunction solar cells, Energy Environ. Sci. 7 (2014) 982–988, https://doi.org/10.1039/c3ee43822h.
[37] B. Ghosh, S. Chakraborty, H. Wei, C. Guet, S. Li, S. Mhaisalkar, N. Mathews, Poor photovoltaic performance of Cs3Bi2I9: an insight through first-principles calculations, J. Phys. Chem. C. 121 (2017) 17062–17067, https://doi.org/10.1021/acs.jpcc.7b03501.
[38] N.H. Tiep, Z. Ku, H.J. Fan, Recent advances in improving the stability of perovskite solar cells, Adv. Energy Mater. 6 (2016) 1–19, https://doi.org/10.1002/aenm.201501420.
[39] J. Zhao, H. Liu, Z. Yu, R. Quhe, S. Zhou, Y. Wang, C.C. Liu, H. Zhong, N. Han, J. Lu, Y. Yao, K. Wu, Rise of silicene: A competitive 2D material, Prog. Mater. Sci. 83 (2016), https://doi.org/10.1016/j.pmatsci.2016.04.001.
[40] B. Saparov, F. Hong, J.-P. Sun, H.-S. Duan, W. Meng, S. Cameron, I.G. Hill, Y. Yan, D.B. Mitzi, Thin-Film Preparation and Characterization of Cs 3 Sb 2 I 9: A Lead-Free Layered Perovskite Semiconductor, Chem. Mater. 27 (2015) 5622–5632, https://doi.org/10.1021/acs.chemmater.5b01989.
[41] M. Serhan, M. Sprowls, D. Jackemeyer, M. Long, I.D. Perez, W. Maret, N. Tao, E. Forzani, Total iron measurement in human serum with a smartphone, AIChE Annu. Meet., Conf. Proc. 2019-Novem (2019) 1–3 https://doi.org/10.1039/x0xx00000x.
[42] M.R. Filip, F. Giustino, Computational Screening of Homovalent Lead Substitution in Organic-Inorganic Halide Perovskites, J. Phys. Chem. C. 120 (2016) 166–173, https://doi.org/10.1021/acs.jpcc.5b11845.
[43] D. Ray, C. Clark, H.Q. Pham, J. Borycz, R.J. Holmes, E.S. Aydil, L. Gagliardi, Computational Study of Structural and Electronic Properties of Lead-Free CsMI3 Perovskites (M = Ge, Sn, Pb, Mg, Ca, Sr, and Ba), J. Phys. Chem. C. 122 (2018) 7838–7848, https://doi.org/10.1021/acs.jpcc.8b00226.
[44] M.C. Payne, M.P. Teter, D.C. Allan, T.A. Arias, ad J.D. Joannopoulos, Iterative minimization techniques for ab initio total-energy calculations: molecular dynamics and conjugate gradients, Rev. Mod. Phys. 64 (1992) 1045.
[45] M. Caid, D. Rached, S. Al-Qaisi, Y. Rached, H. Rached, DFT calculations on physical properties of the lead-free halide-based double perovskite compound Cs2CdZnCl6, Solid State Commun. 369 (2023) 115216, https://doi.org/10.1016/j.ssc.2023.115216.
[46] S.J. Clark, M.D. Segall, C.J. Pickard, P.J. Hasnip, M.I.J. Probert, K. Refson, M.C. Payne, First principles methods using CASTEP, Z. Fur Krist. 220 (2005) 567–570, https://doi.org/10.1524/zkri.220.5.567.65075.
[47] J.P. Perdew, K. Burke, M. Ernzerhof, Generalized gradient approximation made simple, Phys. Rev. Lett. 77 (1996) 3865–3868, https://doi.org/10.1103/PhysRevLett.77.3865.
[48] H.J. Monkhorst, J.D. Pack, Special points for Brillouin-zone integrations, Phys. Rev. B 13 (1976) 5188.
[49] C. Truesdell, Murnaghan's Finite Deformation of an Elastic Solid (1952). in: An Idiot's Fugitive Essays on Science, Springer New York, New York, NY, 1984, pp. 148–150 https://doi.org/10.1007/978-1-4613-8185-3_14.
[50] J.D. Pack, H.J. Monkhorst, special points for Brillouin-zone integrations"-a reply, Phys. Rev. B 16 (1977) 1748–1749, https://doi.org/10.1103/PhysRevB.16.1748.
[51] P. Giannozzi, O. Baseggio, P. Bonfà, D. Brunato, R. Car, I. Carnimeo, C. Cavazzoni, S. de Gironcoli, P. Delugas, F.F. Ruffino, A. Ferretti, N. Marzari, I. Timrov, A. Urru, S. Baroni, Quantum ESPRESSO toward the exascale, J. Chem. Phys. 152 (2020) 154105, https://doi.org/10.1063/5.0005082.
[52] J. Islam, S.K. Mitro, M.M. Hossain, M.M. Uddin, N. Jahan, A.K.M.A. Islam, S.H. Naqib, M.A. Ali, Exploration of the physical properties of the newly synthesized kagome superconductor LaIr3Ga2 using different exchange–correlation functionals, Phys. Chem. Chem. Phys. 24 (2022) 29640–29654, https://doi.org/10.1039/D2CP04054A.
[53] M.H.K. Rubel, S.K. Mitro, K.M. Hossain, M.M. Rahaman, M.K. Hossain, J. Hossain, B.K. Mondal, I. Ahmed, A.K.M.A. Islam, A. El-Denglawey, A comprehensive first principles calculations on (Ba0.82K0.18)(Bi0.53Pb0.47)O3 single-cubic-perovskite superconductor, (2021). https://doi.org/10.1016/j.mtcomm.2022.104302.
[54] Y. Xu, N. Wang, X. Guo, S. Huang, Effects of the coordination number on H2O dissociation reaction on the surface of Zr5nO10n (n = 4–9) nanoparticles: A DFT approach, Int. J. Hydrog. Energy 44 (2019) 31029–31040, https://doi.org/10.1016/j.ijhydene.2019.10.001.
[55] M.A. Ali, M.M. Hossain, M.M. Uddin, M.A. Hossain, A.K.M.A. Islam, S.H. Naqib, Physical properties of new MAX phase borides M2SB (M = Zr, Hf and Nb) in comparison with conventional MAX phase carbides M2SC (M = Zr, Hf and Nb): Comprehensive insights, J. Mater. Res. Technol. 11 (2021) 1000–1018, https://doi.org/10.1016/j.jmrt.2021.01.068.
[56] A. Chowdhury, M.A. Ali, M.M. Hossain, M.M. Uddin, S.H. Naqib, A. Islam, Predicted MAX phase Sc2InC: dynamical stability, vibrational and optical properties, Phys. Status Solidi (B) 255 (2018) 1700235.
[57] M. Born, On the stability of crystal lattices. I, Math. Proc. Camb. Philos. Soc. 36 (1940) 160–172 https://doi.org/DOI: 10.1017/S0305004100017138.
[58] A. Bouhemadou, R. Khenata, M. Kharoubi, Y. Medkour, First-principles study of structural and elastic properties of Sc2AC (A = Al, Ga, In, Tl), Solid State Commun. 146 (2008) 175–180.
[59] Y. Rakita, S.R. Cohen, N.K. Kedem, G. Hodes, D. Cahen, Mechanical properties of APbX3 (A = Cs or CH3NH3; X = I or Br) perovskite single crystals, MRS Commun. 5 (2015) 623–629, https://doi.org/10.1557/mrc.2015.69.
[60] M.M. Woolfson, Solid state physics 3. Theory of lattice dynamics in the harmonic approximation by A. A. Maradudin, E. W. Montroll, G. H. Weiss and I. P. Ipatova, Acta Crystallogr. Sect. A 29 (1973) 314, https://doi.org/10.1107/S0567739473000859.
[61] M.H.K. Rubel, M. Mozahar Ali, M.S. Ali, R. Parvin, M.M. Rahaman, K.M. Hossain, M.I. Hossain, A.K.M.A. Islam, N. Kumada, First−principles study: structural, mechanical, electronic and thermodynamic properties of simple−cubic−perovskite (Ba0.62K0.38)(Bi0.92Mg0.08)O3, Solid State Commun. 288 (2019) 22–27, https://doi.org/10.1016/j.ssc.2018.11.008.
[62] M.T. Nasir, M.A. Hadi, M.A. Rayhan, M.A. Ali, M.M. Hossain, M. Roknuzzaman, S.H. Naqib, A.K.M.A. Islam, M.M. Uddin, K. Ostrikov, First-Principles Study of Superconducting ScRhP and ScIrP pnictides, Phys. Status Solidi (B) 254 (2017) 1700336, https://doi.org/10.1002/pssb.201700336.
[63] X. Wang, H. Xiang, X. Sun, J. Liu, F. Hou, Y. Zhou, Mechanical Properties and Damage Tolerance of Bulk Yb3Al5O12 Ceramic, J. Mater. Sci. Technol. 31 (2015) 369–374, https://doi.org/10.1016/j.jmst.2015.01.002.
[64] M.M. Rahaman, M.H.K. Rubel, M.A. Rashid, M.A. Alam, K.M. Hossain, M.I. Hossain, A.A. Khatun, M.M. Hossain, A.K.M.A. Islam, S. Kojima, N. Kumada, Mechanical, electronic, optical, and thermodynamic properties of orthorhonmbic LiCuBiO4 crystal: a first–priciples study, J. Mater. Res. Technol. 8 (2019) 3783–3794, https://doi.org/10.1016/j.jmrt.2019.06.039.
[65] H. Rached, D. Rached, S. Benalia, A.H. Reshak, M. Rabah, R. Khenata, S. Bin Omran, First-principles study of structural stabilities, elastic and electronic properties of transition metal monocarbides (TMCs) and mononitrides (TMNs), Mater. Chem. Phys. 143 (2013) 93–108, https://doi.org/10.1016/j.matchemphys.2013.08.020.
[66] H. Rached, S. Bendaoudia, D. Rached, Investigation of Iron-based double perovskite oxides on the magnetic phase stability, mechanical, electronic and optical properties via first-principles calculation, Mater. Chem. Phys. 193 (2017) 453–469, https://doi.org/10.1016/j.matchemphys.2017.03.006.
[67] X.-Q. Chen, H. Niu, D. Li, Y. Li, Modeling hardness of polycrystalline materials and bulk metallic glasses, Intermetallics 19 (2011) 1275–1281, https://doi.org/10.1016/j.intermet.2011.03.026.
[68] E. Mazhnik, A.R. Oganov, A model of hardness and fracture toughness of solids, J. Appl. Phys. 126 (2019) 125109, https://doi.org/10.1063/1.5113622.
[69] F. Gao, Theoretical model of intrinsic hardness, Phys. Rev. B 73 (2006) 132104, https://doi.org/10.1103/PhysRevB.73.132104.
[70] M.F. Cover, O. Warschkow, M.M.M. Bilek, D.R. McKenzie, A comprehensive survey of M2AX phase elastic properties, J. Phys.: Condens. Matter 21 (2009) 305403.
[71] S.F. Pugh, XCII. Relations between the elastic moduli and the plastic properties of polycrystalline pure metals, Lond., Edinb., Dublin Philos. Mag. J. Sci. 45 (1954) 823–843, https://doi.org/10.1080/14786440808520496.
[72] I.N. Frantsevich, F.F. Voronov, I.N. Frantsevich, Elastic Constants Elastic Modul. Met. Insul. Handb. (1983) 60–180.
[73] D.G. Pettifor, Theoretical predictions of structure and related properties of intermetallics, Mater. Sci. Technol. 8 (1992) 345–349.
[74] M. Jamal, S. Jalali Asadabadi, I. Ahmad, H.A. Rahnamaye Aliabad, Elastic constants of cubic crystals, Comput. Mater. Sci. 95 (2014) 592–599, https://doi.org/10.1016/j.commatsci.2014.08.027.
[75] D. Vanderbilt, Rapid Communications Soft self-consistent pseudopotentials in a generalized eigenvalue formalism, n.d. file:///C:/Users/tahaitlink/AppData/Local/Mendeley Ltd./Mendeley Desktop/Downloaded/Vanderbilt - Unknown - Rapid Communications Soft self-consistent pseudopotentials in a generalized eigenvalue formalism.pdf.
[76] B.H. Elias, B.M. Ilyas, N.S. Saadi, A first principle study of the perovskite lanthanum aluminate, Mater. Res. Express 5 (2018) 86302, https://doi.org/10.1088/2053-1591/aad15f.
[77] Y.H. Chang, C.H. Park, K. Matsuishi, First-principles study of the structural and the electronic properties of the lead-halide-based inorganic-organic perovskites (CH 3NH 3)PbX 3 and CsPbX 3 (X = Cl, Br, I), J. Korean Phys. Soc. 44 (2004) 889–893.
[78] G. Murtaza, I. Ahmad, First principle study of the structural and optoelectronic properties of cubic perovskites CsPbM3 (M = Cl, Br, I), Phys. B: Condens. Matter 406 (2011) 3222–3229, https://doi.org/10.1016/j.physb.2011.05.028.
[79] M. Afsari, A. Boochani, M. Hantezadeh, Electronic, optical and elastic properties of cubic perovskite CsPbI3: Using first principles study, Optik 127 (2016) 11433–11443, https://doi.org/10.1016/j.ijleo.2016.09.013.
[80] I.R. Shein, A.L. Ivanovskii, Elastic properties of superconducting MAX phases from first-principles calculations, Phys. Status Solidi (B) 248 (2011) 228–232.
[81] L.-K. Gao, Y.-L. Tang, Theoretical study on the carrier mobility and optical properties of CsPbI3 by DFT, ACS Omega 6 (2021) 11545–11555, https://doi.org/10.1021/acsomega.1c00734.
[82] C.H. Hendon, R.X. Yang, L.A. Burton, A. Walsh, Assessment of polyanion (BF4− and PF6−) substitutions in hybrid halide perovskites, J. Mater. Chem. A. 3 (2015) 9067–9070, https://doi.org/10.1039/C4TA05284F.
[83] J. Even, L. Pedesseau, J.-M. Jancu, C. Katan, Importance of Spin–Orbit Coupling in Hybrid Organic/Inorganic Perovskites for Photovoltaic Applications, J. Phys. Chem. Lett. 4 (2013) 2999–3005, https://doi.org/10.1021/jz401532q.
[84] S. Bertolazzi, J. Brivio, A. Kis, Stretching and breaking of ultrathin MoS 2, ACS Nano 5 (2011) 9703–9709, https://doi.org/10.1021/nn203879f.
[85] M. Tomasik, N. Mangan, J. Grossman, Photovoltaic efficiency of an indirect bandgap material, : APS March Meet. Abstr. (2015) L34 .011.
[86] M. Wang, W. Wang, B. Ma, W. Shen, L. Liu, K. Cao, S. Chen, W. Huang, lead-free

perovskite materials for solar cells, Nano-Micro Lett. 13 (2021) 62, https://doi.org/10.1007/s40820-020-00578-z.
[87] S. Azam, S. Goumri-Said, S.A. Khan, M.B. Kanoun, Electronic, optical and thermoelectric properties of new metal-rich homological selenides with palladium–indium: density functional theory and Boltzmann transport model, J. Phys. Chem. Solids 138 (2020) 109229, https://doi.org/10.1016/j.jpcs.2019.109229.
[88] S.A. Dar, R. Sharma, V. Srivastava, U.K. Sakalle, Investigation on the electronic structure, optical, elastic, mechanical, thermodynamic and thermoelectric properties of wide band gap semiconductor double perovskite Ba 2 InTaO 6, RSC Adv. 9 (2019) 9522–9532, https://doi.org/10.1039/C9RA00313D.
[89] V. Kumar, A. Dey, S. Thomas, M. Asle Zaeem, D.R. Roy, Hydrogen-induced tunable electronic and optical properties of a two-dimensional penta-Pt 2 N 4 monolayer, Phys. Chem. Chem. Phys. 23 (2021) 10409–10417, https://doi.org/10.1039/D1CP00681A.
[90] H.M. Ghaithan, Z.A. Alahmed, S.M.H. Qaid, M. Hezam, A.S. Aldwayyan, Density Functional Study of Cubic, Tetragonal, and Orthorhombic CsPbBr3 Perovskite, ACS Omega 5 (2020), https://doi.org/10.1021/acsomega.0c00197.
[91] M. Roknuzzaman, M.A. Hadi, M.A. Ali, M.M. Hossain, N. Jahan, M.M. Uddin, J.A. Alarco, K. Ostrikov, First hafnium-based MAX phase in the 312 family, Hf3AlC2: A first-principles study, J. Alloy. Compd. 727 (2017) 616–626.
[92] M.D.B. Daniel C. Harris (Author), Symmetry and Spectroscopy: An Introduction to Vibrational and Electronic Spectroscopy (Dover Books on Chemistry), Dover Publications; New edition, 1989.
[93] K. Ephraim Babu, N. Murali, K. Vijaya Babu, P. Taddesse Shibeshi, V. Veeraiah, Structural, Elastic, Electronic, and Optical Properties of Cubic Perovskite CsCaCl 3 Compound: An ab initio Study, Acta Phys. Pol. A 125 (2014) 1179–1185, https://doi.org/10.12693/APhysPolA.125.1179.
[94] O.L. Anderson, A simplified method for calculating the debye temperature from elastic constants, J. Phys. Chem. Solids 24 (1963) 909–917, https://doi.org/10.1016/0022-3697(63)90067-2.
[95] N. Mendelson, M. Doherty, M. Toth, I. Aharonovich, T.T. Tran, Strain-Induced Modification of the Optical Characteristics of Quantum Emitters in Hexagonal Boron Nitride, Adv. Mater. 32 (2020), https://doi.org/10.1002/adma.201908316.
[96] Y. Shen, D.R. Clarke, P.A. Fuierer, Anisotropic thermal conductivity of the Aurivillus phase, bismuth titanate (Bi4Ti3O12): A natural nanostructured superlattice, Appl. Phys. Lett. 93 (2008), https://doi.org/10.1063/1.2975163.
[97] M.D. Segall, P.J.D. Lindan, M.J. al Probert, C.J. Pickard, P.J. Hasnip, S.J. Clark, M.C. Payne, First-principles simulation: ideas, illustrations and the CASTEP code, J. Phys.: Condens. Matter 14 (2002) 2717.
[98] K.S. Novoselov, A.K. Geim, S.V. Morozov, D. Jiang, Y. Zhang, S.V. Dubonos, I.V. Grigorieva, A.A. Firsov, Electric field effect in atomically thin carbon films supplementary, Science 5 (2004) 1–12, https://doi.org/10.1126/science.aab1343.
[99] M. Mattesini, M. Magnuson, F. Tasnádi, C. Höglund, I.A. Abrikosov, L. Hultman, Elastic properties and electrostructural correlations in ternary scandium-based cubic inverse perovskites: A first-principles study, Phys. Rev. B - Condens. Matter Mater. Phys. 79 (2009) 1–9, https://doi.org/10.1103/PhysRevB.79.125122.
[100] M. Naguib, V.N. Mochalin, M.W. Barsoum, Y. Gogotsi, 25th anniversary article: MXenes: A new family of two-dimensional materials, Adv. Mater. 26 (2014), https://doi.org/10.1002/adma.201304138.
[101] M.A. Ali, M.S. Ali, M.M. Uddin, Structural, elastic, electronic and optical properties of metastable MAX phase Ti5SiC4 compound, Indian J. Pure Appl. Phys. 54 (2016) 386–390.
[102] P. Debye, Zur theorie der spezifischen wärmen, Ann. Der Phys. 344 (1912) 789–839.
[103] M.A. Blanco, E. Francisco, V. Luaña, GIBBS: Isothermal-isobaric thermodynamics of solids from energy curves using a quasi-harmonic Debye model, Comput. Phys. Commun. 158 (2004) 57–72, https://doi.org/10.1016/j.comphy.2003.12.001.
[104] S. Cui, W. Feng, H. Hu, Z. Feng, H. Liu, Hexagonal Ti2SC with high hardness and brittleness: a first-principles study, Scr. Mater. 61 (2009) 576–579, https://doi.org/10.1016/j.scriptamat.2009.05.026.
[105] M.A. Hadi, M. Roknuzzaman, A. Chroneos, S.H. Naqib, A.K.M.A. Islam, R.V. Vovk, K. Ostrikov, Elastic and thermodynamic properties of new (Zr3−xTix)AlC2 MAX-phase solid solutions, Comput. Mater. Sci. 137 (2017) 318–326, https://doi.org/10.1016/j.commatsci.2017.06.007.